

REPORT DOCUMENTATION PAGE

AFRL-SR-AR-TR-03-

0107

Public reporting burden for this collection of information is estimated to average 1 hour per response, including the time for gathering and maintaining the data needed, and completing and reviewing this collection of information. Send comments regarding this collection of information, including suggestions for reducing this burden to Department of Defense, Washington Headquarters Reports (0704-0188), 1215 Jefferson Davis Highway, Suite 1204, Arlington, VA 22202-4302. Respondents should be aware that be subject to any penalty for failing to comply with a collection of information if it does not display a currently valid OMB control number. PLEASE DO NOT RETURN YOUR FORM TO THE ABOVE ADDRESS.

1. REPORT DATE (DD-MM-YYYY) 28-02-03	2. REPORT TYPE Final Report	3. DATES COVERED (From - To) 01-02-00 through 30-11-02		
4. TITLE AND SUBTITLE Cluster Ion Beam Studies of Fundamental Dynamics Related to to Physical Deposition		5a. CONTRACT NUMBER		
		5b. GRANT NUMBER F49620-00-1-0138		
		5c. PROGRAM ELEMENT NUMBER		
6. AUTHOR(S) Scott L. Anderson		5d. PROJECT NUMBER		
		5e. TASK NUMBER		
		5f. WORK UNIT NUMBER		
7. PERFORMING ORGANIZATION NAME(S) AND ADDRESS(ES) Department of Chemistry University of Utah 315 S. 1400 E. Rm 2020 Salt Lake City, UT 84112		8. PERFORMING ORGANIZATION REPORT NUMBER		
9. SPONSORING / MONITORING AGENCY NAME(S) AND ADDRESS(ES) Dr. Michael Berman AFOSR/NL 4015 Wilson Blvd, Rm 713 Arlington, VA 22203-1954		10. SPONSOR/MONITOR'S ACRONYM(S) AFOSR/NL		
		11. SPONSOR/MONITOR'S REPORT NUMBER(S)		
12. DISTRIBUTION / AVAILABILITY STATEMENT <i>Approve for Public Release; Distribution Unlimited</i>				
13. SUPPLEMENTARY NOTES				
14. ABSTRACT Instrumental developments during the grant period are reported. Results for the Ni/TiO ₂ are summarized with details provided in an attachment. Details are reported regarding the Ir/TiO ₂ system.				
15. SUBJECT TERMS Clusters Deposition Thin Films Catalysis				
16. SECURITY CLASSIFICATION OF: a. REPORT unclassified		17. LIMITATION OF ABSTRACT UL	18. NUMBER OF PAGES 21	19a. NAME OF RESPONSIBLE PERSON Scott L. Anderson
b. ABSTRACT unclassified				19b. TELEPHONE NUMBER (include area code) 801-585-7289
c. THIS PAGE unclassified				

20030508 099

Objective:

The original proposal for this grant was to continue studies of the dynamics involved in small cluster impacts on solid substrates. With agreement of AFOSR, the effort was re-focused on cluster deposition as a means to prepare and study model catalysts composed of size-selected clusters on oxide supports. The objectives are to probe the effects of cluster size, substrate structure, and deposition conditions on catalytic activity. The focus is on catalysts for monopropellant decomposition in spacecraft thrusters. These operate under unusually harsh conditions, where catalyst stability is the major problem, unlike more typical industrial catalysts, where activity and selectivity are the major problems. We are particularly interested in developing approaches that may lead to new sinter-resistant catalysts.

Accomplishments during the grant period:

Roughly the first half of the grant period was occupied by a series preliminary experiments, alternating with instrumental upgrades that were felt to be necessary for the catalysis experiments. The second half of the grant period was devoted to publication grade experiments, although we continued some instrument upgrades, and development of improved experimental methodologies. At present one full study has been published, and a second will be submitted for publication this week. Because both these initial studies were done during periods with significant instrument development, the papers acknowledge support from both AFOSR and DOE, which was also supporting our cluster deposition effort. The scientific goals of the DOE-funded work were complementary to the focus of the AFOSR-funded effort. (AFOSR: stable catalysts for monopropellant decomposition. DOE: effects of cluster size and support defects on catalytic activity and selectivity). Toward the end of the grant period, we "finished" the instrument development, and the DOE and AFOSR efforts have now diverged. On-going AFOSR-funded work focuses on hydrazine decomposition on Ir_n clusters, and will be published with acknowledging sole support from AFOSR. DOE-sponsored work is currently focusing on CO oxidation on supported Pd clusters.

Instrument Upgrades

To facilitate the catalysis experiments agreed on with AFOSR, a number of instrument upgrades were carried out:

1. **Upgrades of the cluster deposition beamline:**
 - a. Addition of a wide mass range quadrupole mass filter.
 - b. Redesign of the focus/mask ion optics in the deposition stage, increasing spot size and intensity
 - c. Redesign of front end rf guides, including addition of a 18 degree bending section, for better coupling to the source.
2. **Addition of low energy ion scattering spectroscopy (ISS).** One observation in the work to date, is that chemistry on the supported clusters has a *large* effect on their morphology. This effect is well known in catalysis, and ISS capabilities were added to provide an *in situ* probe of morphology. In addition to being quick and reliable, ISS can be done while heating the sample, allowing morphology changes to be followed in quasi-real time.
3. **Addition of Auger electron spectroscopy (AES).** Provides a faster and more sensitive (than XPS) check of sample contamination and deposition spot profiles.
4. **Redesign of sample holders and TPD station.** Our original sample holder/station system won the AVS Vacuum Technology Division 2001 award for the best note in J. Vac. Sci. Tech. describing an experimental innovation. Nonetheless, it needed improvements to reach lower temperatures. In addition, an improved differential pumping system added, and a computer-controlled PID system was developed to handle the somewhat tricky temperature control that results from e-beam heating.

DISTRIBUTION STATEMENT A
Approved for Public Release
Distribution Unlimited

Experiments performed to date.

I. Ni_n^+ on TiO_2 (110): (reprint attached)

This study represents the first use of ISS to characterize size-selected deposited clusters, and this technique proved to be critical to understanding the chemistry. We studied Ni_n/TiO_2 samples prepared by size-selected deposition of Ni_n^+ ($n = 1, 2, 5, 10, 15$) on rutile TiO_2 (110)-(1x1). The effects of deposition energy and support preparation conditions on the oxidation state of the clusters were examined by x-ray photoelectron spectroscopy (XPS). On the stoichiometric surface, Ni_n are stable, but oxidation can be driven by increased impact energy. For TiO_2 surfaces with chemisorbed oxygen, deposited Ni_n are oxidized even at low impact energies. ISS was used to characterize the dispersion of Ni on the support, and provide some insight into binding morphology. Small clusters bind in such a way that preferentially attenuates ion scattering from oxygen. There is some evidence that deposited Ni atoms preferentially bind into missing-oxygen defects on the surface. Large clusters bind in compact geometries and the largest clusters appear to retain some three dimensional character on the surface. The data suggest that the clusters neither fragment, nor agglomerate, in room temperature deposition. Temperature programmed desorption (TPD) of CO was used to characterize deposited clusters. For these small clusters, no strong desorption features are observed in the temperature range above 140 K, where CO desorbs from TiO_2 . The lack of CO binding appears to be a consequence of strong Ni-TiO₂ binding. The ion scattering data indicated that there is significant sintering, and possibly partial encapsulation, of the Ni clusters during the TPD experiments. XPS reveals little change in oxidation state. This was the first study where the oxidation state and morphology of size-selected deposited clusters was studied, before and after TPD.

II. Ir_n on TiO_2 (110)

Iridium is the current catalyst of choice for monopropellant decomposition, and thus is a logical choice for initial study. The rutile TiO_2 (110)-(1x1) surface was chosen as the initial substrate for study, because we had considerable experience with preparing good single crystal stoichiometric surfaces, with controlled and variable defect density. Our preparation procedure for the TiO_2 is similar to that reported by Li and coworkers [1]. The sample is mounted on a sample holder similar to award-winning sample holder we described previously[2] that allows samples to be transferred between precision preparation/analysis stations, while providing for heating/cooling and temperature measurement. The sample holders were improved by constructing them from OFHC copper to allow lower temperature to be reached. Iridium clusters are produced by a 100 Hz laser vaporization/nozzle source similar to that reported by Heiz and coworkers,[3] the principle difference being that we use a pair of computer-controlled translation stages to raster the Ir target across the vaporization position. The advantage to this approach is that we can use small and irregularly-shaped vaporization targets – a significant advantage when dealing with expensive metals. The clusters are collected and guided through several stages of differential pumping, then the cluster size of interest is selected using a conventional quadrupole mass filter. Finally, clusters are passed through an additional differential pumping stage, and delivered to the TiO_2 target through a 2mm diameter exposure mask. Current is measured directly on the deposition substrate, and the energy spread, determined by retarding potential analysis at the substrate, is better than 1 eV FWHM. (Achieving good energy spread and high currents is non-trivial, and was a major focus of the beamline design). The deposition spot size is profiled by AES, with resolution of ~0.1mm. To check for possible deposition of contaminants from the beamline, samples were examined with AES and TPD following a prolonged exposure under deposition conditions, but with the sample biased to prevent ion impact. No metal deposition is observed, and the level of other surface contaminants is identical to that resulting from a similar time exposure to base pressure.

Except for a few experiments noted below, the total Ir dose was fixed at 1.6×10^{14} Ir atoms per cm^2 , corresponding to a tenth of a close-packed Ir monolayer. Deposition times are typically 30 minutes,

and do not vary strongly with cluster size, because the decline in ion current with size is approximately countered by the increase in number of atoms *per* cluster. The exception is Ir⁺, where intensity can be made very large, allowing rapid deposition. Because the cluster beam energy spread is small, the deposition time is also independent of energy, over the entire energy range explored here. Both before and after deposition, the sample is analyzed by XPS and ISS, providing insight into the effects of deposition on the oxidation state and morphology of the cluster/TiO₂ composite. ISS was done using a 1 keV He⁺ beam, incident at 45 degrees with a current density of about 10 microA/cm² ($6 \times 10^{13} \text{ cm}^{-2} \cdot \text{sec}^{-1}$). Scattered He⁺ ions are collected along the surface normal, thus the scattering angle is fixed at 135 degrees. To minimize surface damage, ISS data are taken quickly – about 30 seconds total exposure to the ion beam for a survey scan, and select experiments were also done with He⁺ exposures about 100 times lower. Because 1 keV He⁺ may cause several types of damage, we have done a number of experiments to probe the effects. XPS data are taken for clean TiO₂ surfaces before and after performing ISS. After taking ISS, the Ti 2p XPS shows a small increase in the Ti³⁺ shoulder, and the O 1s XPS is slightly reduced in intensity. XPS analysis indicates that a single ISS spectrum increases the concentration of Ti³⁺ to ~9%, presumably mostly in the form of missing oxygen defects.[4] We also examined the change in O and Ti ISS peak intensities, and found that after an ISS scan, the O/Ti ISS ratio decreases ~6%.

To obtain results not complicated by the ISS-induced defects, the main set of cluster deposition/characterization experiments at 1 eV/atom deposition energy was also run without ISS characterization prior to TPD analysis. Comparison of data sets with, and without ISS provides some insight into the effects of support defects on the cluster properties. No differences are observed in the Ir XPS. As discussed below, we do find that the CO TPD measurements are modestly affected by pre-TPD ISS characterization, so the main TPD results presented are from the set taken without prior ISS. For TPD measurements, C¹⁸O is introduced to the chamber through a leak valve, and doses are estimated from the pressure (3×10^{-8} Torr) measured using an ion gauge, with correction for sensitivity to CO. TPD experiments involve heating the sample at a rate of 3 K/sec to 800K, then rapidly cooling back to 300 K. Typically, three successive TPD runs are performed to study the effects of TPD-induced changes in sample properties. Finally, after the TPD experiments, XPS and ISS spectra are again recorded to examine the effects of TPD on the oxidation state and morphology of the sample.

Because CO desorption temperatures from single crystal Ir(110)[5, 6] and Ir(111)[7] are 530K and 550K, respectively, some adsorption of adventitious CO on our supported Ir clusters is expected during deposition and XPS analysis. To quantify the adventitious CO exposure, we also looked at CO TPD from Ni (100) following 1 hour exposure to the deposition chamber background, and following 1 hour in the deposition station with gas flows identical to those during deposition. The amount of CO desorbing following background exposure was 20% of that desorbing following a 0.5L dose, and was independent of whether the exposure was in the deposition position or not. The estimated adventitious CO exposure for the clusters is ~0.095 L – consistent with the value estimated from the CO partial pressure ($\sim 4 \times 10^{-11}$ Torr) and exposure time. For CO at room temperature, 1 L corresponds to 3.8×10^{14} collisions/cm², thus 0.1L exposure corresponds to 2.4% of the density of a close-packed Ir monolayer ($1.56 \times 10^{15}/\text{cm}^2$).

A. X-ray photoelectron spectroscopy

Examples of Ti 2p XPS data are shown in Fig. 1 with the expected peak positions[8] for the +3 and +4 oxidation states indicated by vertical lines. The upper spectra (A) are for annealed TiO₂, and the higher intensity Ti³⁺ shoulder in the lower set of spectra shows the presence of additional missing O defects created by 1 keV He⁺ bombardment. The solid lines are the spectra for clean TiO₂ prepared as above. The dotted lines show the spectra acquired immediately after depositing 0.1ML equivalent of Ir₂ at an impact energy of 1eV/atom. First consider the top spectra, for freshly annealed TiO₂. The intensity in the region where Ti³⁺ should appear is too low to allow extraction of a precise value of the Ti³⁺ density, with estimates ranging from 3 to 8%, depending on the lineshape assumed for the dominant Ti⁴⁺ peak. After deposition of 0.1 ML equivalent of Ir₂, there is a slight general intensity reduction, as

expected because Ir on the surface will tend to attenuate photoelectrons from the underlying substrate, and in addition, the relative Ti^{+3} intensity is slightly reduced. The latter effect is more obvious in the bottom set of spectra, where the pre-deposition Ti^{+3} intensity is higher. It is quite clear that the Ti^{+3} intensity decreases upon Ir deposition, and the Ti^{+4} intensity decreases less than would be expected from attenuation by the overlying Ir. These data indicate that a fraction of the surface Ti^{+3} centers, i.e., Ti at missing oxygen defects, are oxidized to Ti^{+4} by interaction with the deposited Ir. We also considered the possibility that the Ti^{+3} might be oxidized by reaction with background gas during the deposition time, however, the Ti XPS shows no change after exposure to background for one hour, in absence of Ir deposition.

Fig. 2 shows Ir 4f XPS spectra for different size Ir clusters deposited at various impact energies. The solid lines are the XPS for as-deposited clusters, and the dotted lines are post-TPD spectra, discussed below. Table 1 gives integrated XPS peak areas, normalized to the value for 0.1 ML of Ir^+ at 1 eV/atom. Consider, first, the spectra for as-deposited clusters, indicated with solid lines. The Ir 4f doublet structure is shifted ~ 0.3 eV to higher binding energy, compared to the binding energy reported for bulk Ir. The shift is in the direction of positive oxidation states of Ir, qualitatively similar to the shift observed by Escard *et al.* [9] for 15 nm mean diameter iridium particles on TiO_2 . They interpreted the shift as indicating partial oxidation of Ir by the substrate, however, this interpretation is contradicted by our observation that the Ti^{+3} intensity decreases, rather than increasing upon Ir deposition. (The case of Ni_n deposited at high energies on TiO_2 provides a clear case where deposited metal is oxidized by the support – the growth of Ni^{+3} intensity is clearly correlated by reduction of Ti^{+4} to Ti^{+3} . [10]) Shifts of XPS binding energies for small metal particles on oxide surfaces are complicated by final state relaxation effects, which can counter or reinforce the shift resulting from the metal initial state (i.e., oxidation state). [11, 12] For example, Bahl *et al.* [13] have examined XPS spectra for Pt supported on SrTiO_3 , and find that there is a net charge transfer of 0.6 electrons from the support oxide to the supported Pt metal, after taking into account the final state relaxation effects on the binding energy. In order to extract the true metal oxidation state from binding energy shifts, the final state relaxation shift needs to be estimated, and this was

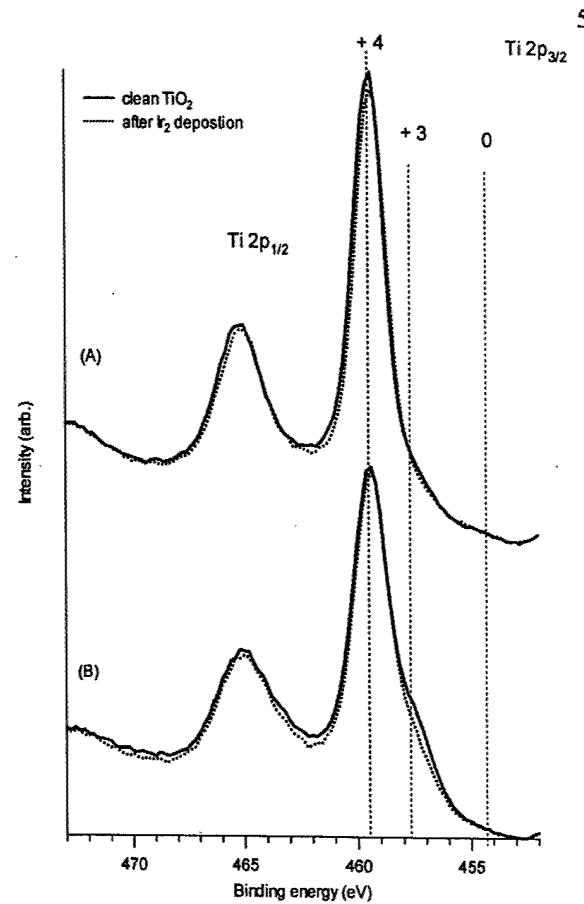


Figure 1. Ti 2p XPS

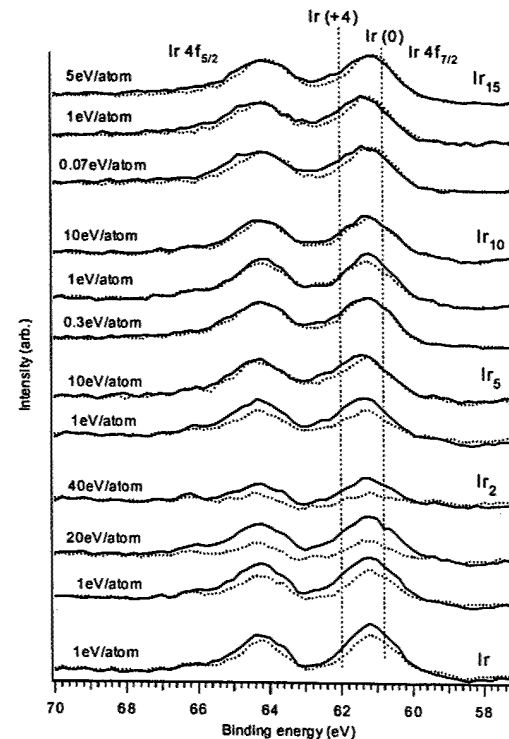


Figure 2. Ir 4f XPS

done using the approximate method proposed by Bahl *et al.*[13] and Oberli *et al.*[14] based on measured XPS and AES peak shifts. To extract the relaxation energy shift, we compared the XPS and Auger spectra for samples containing 0.1ML equivalent of Ir_n on TiO_2 with those for Ir foil (bulk). The Ir 4f XPS for the Ir_n/TiO_2 samples is shifted $\sim 0.3\text{eV}$ towards higher binding energy compared to the bulk, while the Ir LMM Auger peak at 58.0 eV for Ir_n/TiO_2 is shifted 1.5eV toward lower kinetic energy compared to bulk Ir. Based on these measured shifts, the estimated final state relaxation contribution to the Ir XPS shift is $+0.6\text{ eV}$. Thus, the observed Ir 4f binding energy shift of $+0.3\text{ eV}$ actually corresponds to a shift of roughly -0.3 eV in the core level energy. In other words, after correction for the final state effect, the XPS data correspond to net electron transfer from the TiO_2 to the Ir clusters, consistent with our observation that Ti^{+3} tends to be oxidized by Ir deposition. This oxidation could indicate that the Ir clusters tend to bind at missing oxygen defect sites, or possibly that Ir binding to TiO_2 near defect sites is able to induce reconstruction that oxidizes the Ti^{+3} center.

Within the uncertainty of the background subtraction/integration process ($\pm 5\%$), the intensity of the Ir XPS for as-deposited clusters (solid lines) is nearly independent of cluster size and impact energy. The only obvious exception is that the XPS intensity for Ir_2 at 40 eV/atom is only about half the intensity for lower impact energies. XPS intensity is determined by the Ir concentration in the sample, weighted by the variation in detection efficiency with depth. The inelastic mean free path (IMFP) of the Ir photoelectrons in TiO_2 is approximately 2.3 nm (calculated using the predictive formula in the NIST IMFP database[15]), thus the Ir XPS is sensitive to Ir in the top few nanometers of the sample.

The observation that the XPS intensity is nearly size- and impact energy-independent indicates that the sticking coefficient for Ir_n on TiO_2 is also independent of size and energy, at least for energies below tens of eV/atom. It is hard to imagine a mechanism whereby the sticking coefficient could be low, but also nearly constant over a wide impact energy range, therefore, we conclude that these data indicate near-unit sticking coefficient over most or all of the energy range studied. Sticking probability can also be estimated from the intensity of the Ir XPS, relative to that of TiO_2 , if some depth distribution is assumed. Assuming that all Ir is on top of the TiO_2 sample for low deposition energies, the measured Ir/Ti XPS intensities correspond to a sticking coefficient of unity, within the experimental uncertainty. Near-unit sticking probability is not unexpected, given the strength of the Ir- TiO_2 interaction (see above). The explanation for the decrease in Ir XPS at the highest impact energies becomes clear in light of the ISS results discussed below.

Note that no significant shifts or new peaks/shoulders are observed over the range of cluster size and impact energy studied, indicating that the oxidation state of Ir is not significantly affected by either cluster size or impact energy. This situation is quite different from the case of Ni_n deposited on TiO_2 ,[16] where deposition at impact energies above $\sim 10\text{eV/atom}$ results in significant new Ni^{+3} peaks, indicating the onset of impact-driven redox reaction between Ni_n and TiO_2 . The lack of peak shifts for different cluster size is interesting in light of many previous experiments where binding energies were inferred to shift with cluster size.[11, 12, 17, 18] Most of these experiments actually measured binding energy as a function of evaporative metal dose, and inferred that the dependence was actually on cluster size. For example, Fritsch *et al.*[19] studied XPS shifts for Ir evaporated on carbon with increasing deposition time. They found that the Ir 4f binding energy is initially shifted 1.0 eV to higher binding energy (relative to bulk metallic Ir), but decreases with time, finally reaching the metallic value. They concluded that the shift was due to increasing Ir cluster size because the final state shifts are expected to decrease with increasing cluster size.

There are several conceivable explanations for why we don't see significant cluster size shifts. From the XPS data alone, one might conclude that our clusters are sintering or fragmenting such that the actual size distribution of Ir on the surface is independent of the deposited cluster size and energy. The ISS results clearly show, however, that this is not the case. More likely, the cluster sizes probed in our experiments are simply too small for there to be significant dependence of the final state relaxation on size. Photoemission leaves a cluster with a unit positive charge that is eventually neutralized by electron transfer from the substrate. On semiconducting or insulating substrates, electron transfer from the

substrate may be slow compared to the photoemission time scale, so that the photoemission final state is determined by only intra-cluster electronic relaxation. If the clusters are truly metallic, then the core hole is screened by the conduction electrons such that the charge appears at the surface of the cluster. As the size is reduced, the final state energy is increased by the coulomb energy, $e^2/2r$, where r is the cluster radius. On the other hand, if the clusters are not metallic, then the extent of screening is limited to localized polarization of the valence electrons, and may not depend strongly on cluster size. Such localized screening was inferred, for example, by Wertheim and co-workers for metal clusters containing fewer than 30 atoms supported on amorphous carbon. In the end, it is difficult to assess what shifts might be expected with cluster size, because the net XPS shift is the result of two partially cancelling effects. Initial state effects (partial electron transfer to the clusters) tend to shift the peak to lower binding energy, while the final state effects tend to shift to higher binding energy. Both effects are expected to die out with increasing Ir cluster size, but not necessarily at the same rate.

B. Low energy ion scattering spectroscopy

To provide some insight into the morphology of the cluster/substrate composite, we performed low energy ion scattering spectroscopy (ISS) studies. ISS is sensitive to surface structure in several ways. To a good approximation, scattering of 1 keV He^+ can be thought of as isolated binary collisions between the He^+ and surface atoms, and to a good approximation, the interaction of the atom pair is elastic. In that case, the laboratory frame energy of the scattered He^+ is a simple function of the scattering angle (fixed at 135 degrees) and the mass of the surface atom.[20] As Fig. 3 shows, the ISS spectra for Ir_n/TiO_2 samples consist of three peaks at different He^+ energies (plotted as E/E_0 , where E_0 is the 1 keV initial energy), corresponding to scattering from O, Ti, and Ir. Note that the Ir ISS peak intensity is strongly dependent on the size of the deposited cluster, demonstrating that deposited cluster size has a strong effect on the morphology of the resulting sample. As we will see below, cluster deposition energy also has a strong effect on ISS intensities.

While ISS peak positions are trivially interpreted, peak intensities are a far more complex problem. Intensities can logically be considered to be a convolution of three factors: the cross section for scattering from a particular type of atom, the He^+ ion survival probability (ISP), and the extent to which different surface atoms are shadowed or blocked by other surface atoms. For 1 keV He^+ , the scattering cross section depends mostly on the radial distribution of the surface atom's core electrons, and therefore is not strongly dependent on oxidation state. The most important factor in ISS intensities for our scattering geometry is the ISP, because most He^+ is neutralized during the scattering process. The ISP depends on the electron densities traversed during each scattering trajectory, and thus varies with the chemical element, oxidation state, and local environment of the target atom. High neutralization probability greatly simplifies the ISS spectra, because only single-scattering events from top layer atoms contribute significantly to the ISS spectrum. For Ir deposited on top of the surface, the underlying Ti or O atoms are effectively 2nd layer atoms, thus ion scattering from them is greatly attenuated. The oxidation state of the surface atoms can affect ISP, complicating interpretation of ISS if sample oxidation

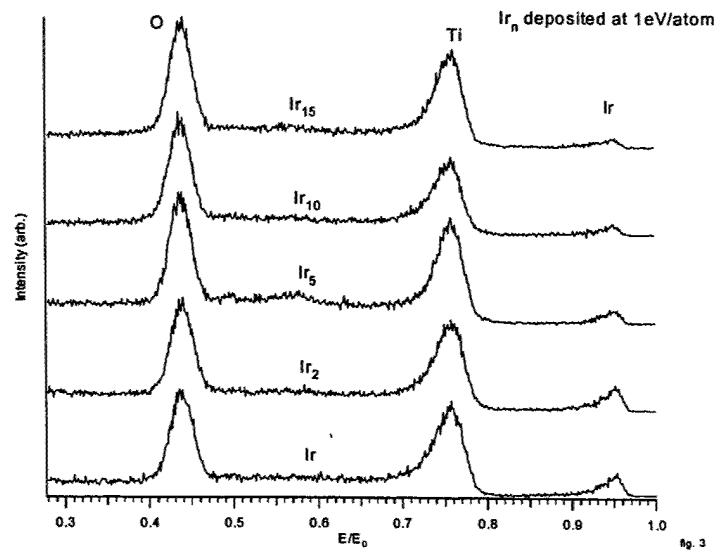


Figure 3 ISS spectra of Ir_n/TiO_2

state changes with cluster size or impact energy. For this system, the XPS shows no significant oxidation state changes, therefore the ISS variations must be related to morphology changes. The effect of oxidation state on ISP can be seen from the presence of a weak peak at $E/E_0 \sim 0.57$ for Ir_5 , attributed to the presence of surface Na. This Na contamination is well below the level detectable by AES, but high ISP for scattering from surface Na^+ enhances the ISS detection efficiency dramatically. By comparing ISS and AES intensities for a sample deliberately contaminated with enough Na to quantitate with AES, we estimate that the Na coverage present in the worst case ISS spectrum in Fig. 3 is less than 0.05%.

The final effects are blocking and shadowing. Blocking is when He^+ scattered from one atom cannot reach the detector because a second atom is in the way. Because we detect along the surface normal, blocking affects only atoms directly underneath the surface atom, and these 2nd layer atoms already have negligible detection probability. Shadowing refers to the fact that atoms on the surface cast a roughly conical scattering shadow, i.e., scattering from a surface atom prevents He^+ from reaching other atoms that are directly behind it. The shadow cone radius for 1 keV He^+ scattering from an Ir adatom is estimated[21] to be ~ 0.12 nm at a distance corresponding to the TiO_2 surface layer. Each Ir adatom shadows about one Ti or O surface layer atom, on average.

In essence, ISP, shadowing, and blocking will eliminate ISS signal from atoms directly beneath Ir adatoms, will also tend to attenuate ISS signal for scattering from surface layer atoms immediately surrounding the site of ad-atom binding. As a consequence, we expect the largest Ir ISS peaks and the greatest attenuation of Ti and O ISS peaks (i.e., the largest Ir/Ti and Ir/O ISS peak ratios), should occur for Ir dispersed as atoms on top of the surface. If the deposited Ir is in the form of clusters on top of the surface, there will be less attenuation of Ti and O signal, because areas attenuated by adjacent Ir atoms will tend to overlap to some extent, leaving a larger fraction of the TiO_2 exposed. Note, however, that for our 0.1 ML Ir dose, most of the TiO_2 is exposed regardless of Ir morphology, thus the O and Ti ISS intensities can't change much. Any large changes in Ir/Ti or Ir/O ISS peak ratios must, therefore, originate from changes in Ir signal. If the deposited Ir forms one or two dimensional islands on the surface, the Ir ISS signal should be unchanged, and the resulting Ir/Ti or Ir/O ratios should be close to the dispersed atom limit. If, however, deposition leads to formation of Ir clusters with multilayer structure, then the Ir ISS signal should be substantially reduced, because the top layer Ir atoms will attenuate signal from the lower layers. Similarly, if Ir is implanted or diffuses beneath the TiO_2 surface, or is decorated by adsorbed species, the Ir ISS signal would be strongly attenuated, or entirely absent.

Absolute ISS intensities taken during the course of the experiments are quite reproducible, nonetheless, to compensate for possible variations in He^+ beam intensity, focus, detector gain, etc., our analysis will largely be based on ratios of ISS peaks. Ir/O , Ir/Ti , and O/Ti ISS peak ratios are calculated by integrating the peak areas. Fig. 4 gives the Ir/substrate ratio (average of Ir/O and Ir/Ti) and O/Ti ratio as a function of cluster size,

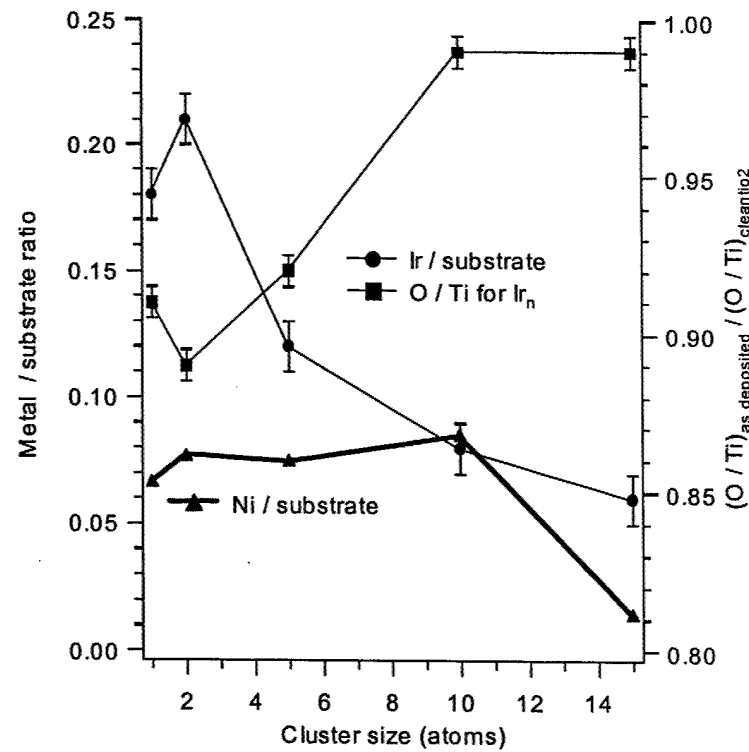


Figure 4. Metal/substrate and O/Ti ISS intensity ratios

for deposition at 1 eV/atom energy. Also shown in Fig. 4 for comparison, are the analogous metal/substrate ratios for 1 eV/atom deposition of 0.1 ML equivalent of Ni_n on TiO_2 .^[16] The O/Ti ratio has been normalized to the O/Ti ratio for clean freshly annealed TiO_2 . The ISS intensities are summarized in Table 1. It should be noted that the deposition times and spot sizes are approximately independent of cluster size and impact energy, and the XPS data show that sticking probability is also constant, except perhaps at the highest energies. The changes in ISS ratios must, therefore, be related to the morphology of the samples.

The most obvious trend, clear in both raw data (Fig. 3) and in the ratios (Fig. 4), is that the Ir/substrate ratio decreases by about a factor of four as the deposited cluster size increases, largely because the Ir ISS intensity decreases. A more subtle effect, evident in Fig. 4, is that the O/Ti ratio depends on cluster size. For the large clusters, the O/Ti ratio is close to the value observed for clean TiO_2 , but the ratio drops by ~10% for the small clusters. These results show that the morphology of the deposited Ir is strongly dependent on the size of clusters deposited. In particular, we can rule out the possibility that the clusters might be sintering or fragmenting extensively upon deposition, because in either case, the final state of the system would be approximately independent of deposited cluster size.

The most reasonable explanation for the trend in Ir/substrate ratio is that the size of clusters on the surface is strongly correlated with the size deposited, i.e., the clusters are remaining approximately intact. Deposition of Ir and Ir_2 results in high dispersion, so that the Ir/substrate ratio is large. The rapid decrease in Ir/substrate ratio with increasing cluster size implies that an increasing fraction of the Ir is no longer in the top-most layer for the larger clusters, i.e., the supported clusters are multilayer, retaining some memory of their 3-d gas-phase structures. Only a small degree of multilayer character is probably needed to cause a significant change in the ISS. For example, if the structure of deposited Ir_5 were Ir_4 with a single Ir on top, we would expect the signal from the lower four atoms to be significantly attenuated by ISP and shadowing effects. The cluster size dependence of the O/Ti ratio is also consistent with the clusters remaining approximately intact in low energy deposition. For large multilayer clusters, the O/Ti ratio must be close to the clean TiO_2 limit, both because most of the substrate is free of Ir, and because the cluster "footprint" is large enough that it will tend to attenuate O and Ti ISS signal equally. The decrease in O/Ti ratio with decreasing size indicates that Ir deposited as small clusters binds so that it preferentially attenuates scattering from surface O. The preference is actually quite strong, considering that 0.1 ML equivalent of Ir results in up to a ~10% decrease in the O/Ti ratio.

Further evidence regarding the structure of the supported iridium clusters comes from the decay slope of Ir ISS intensity with He^+ sputtering time, shown in Fig. 5 as Ir/Ti ratios, normalized to the ratios observed for as-deposited clusters. (The Ir/Ti ratio is plotted, rather than Ir/substrate, because O tends to sputter rapidly compared to Ti). This experiment is done simply by leaving the He^+ beam on continuously, and periodically running ISS scans. Only the early, *quasi*-linear part of the time dependence is shown, and the lines are simple linear fits to the data. The times indicated are the start times of each ~30 second ISS scan. The sputter rate (slope) is quite strongly correlated with cluster size. The decay is rapid with similar slopes for Ir and Ir_2 , but slows dramatically for the larger clusters, which are inferred to have multilayer structures from the ISS intensities. This trend is exact what is expected. For multilayer clusters the sputter-induced decay in Ir ISS should be slow because loss of Ir by

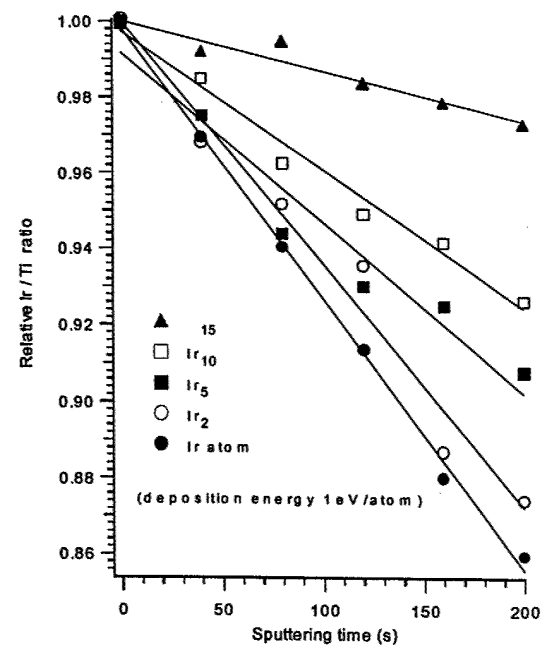


Figure 5 ISS Ir/Ti ratios as a function of He^+ sputter time

sputtering is partly offset by exposure of previously hidden Ir. In addition, it is not unlikely that the Ir sputter yield (Ir sputtered/incident He^+) should depend to some extent on the cluster size, because higher Ir-Ir coordination may stabilize against Ir sputtering.

Because the trends in ISS intensities and sputter rates are exactly what is expected if the post-deposition cluster size matches the size selected, we conclude that the clusters are depositing more-or-less intact at 1 eV/atom energy. By more-or-less intact, we are not suggesting that the structure of the clusters is unaffected by deposition, but only that most clusters are not fragmented or sintered. Indeed, the calculations of Pala *et al.*[22] suggest that Ir-TiO₂ binding should be relatively strong even for perfect TiO₂, presumably leading to changes in both geometry and electronic structure relative to the free clusters. Their calculations also suggest that the interaction potential is strongly corrugated – and that probably accounts for the apparent lack of diffusion (i.e. fragmentation or sintering) at room temperature. To the extent that the clusters bind at missing oxygen defects on the surface, this may provide an additional stabilization mechanism.

There are alternative ways to rationalize the decrease in Ir/substrate ratio with increasing cluster size. It might be, for example, that the larger clusters tend to implant or diffuse into the TiO₂ surface. As discussed below, we do observe such implantation behavior, however, the threshold for implantation is well above 1 eV/atom. A large decrease in Ir ISS would also be expected if the clusters become adsorbate covered, or encapsulated by TiO_x during the deposition process. There is some evidence for possible encapsulation when the samples are heated above 600K, but not at room temperature. The effect of both adventitious and deliberately dosed adsorbates on ISS signal is discussed below, however, it is clear that this issue account for the large cluster size effects.

For comparison, Fig. 4 also gives results for Ni_n deposition on TiO₂, taken under identical conditions.[10] Note that the Ni/substrate ratio is nearly constant for n up to 10, and decreases only for larger clusters. We take this as evidence that the small Ni clusters flatten on the surface during deposition, so that the transition to multilayer supported clusters only occurs for the larger sizes. The greater tendency of Ni_n to flatten on the surface is favored by the smaller Ni - substrate mass ratio, which makes the TiO₂ surface effectively stiffer for Ni_n impacts. Perhaps more importantly, Ir shows a much greater tendency than Ni toward multilayer growth on TiO₂, even for growth of films by low energy metal atomic ion deposition. This behavior can be seen in Table 1, by comparing the metal/substrate ISS ratios for 0.1 and 1.0 ML depositions of Ni and Ir. Note that the Ir/substrate ratio increases by only a factor of 1.8 between 0.1 and 1.0 ML, implying that Ir must be forming multilayer clusters, leaving the TiO₂ mostly Ir-free. In contrast, the Ni/substrate ratio grows by a factor of 16, indicating that Ni is covering a large fraction of the TiO₂. Caution is warranted in interpreting these dose-dependences, because the ISP might change with metal concentration differently for the two metals. Nonetheless, it is clear that Ni has a greater tendency to spread out on the surface than Ir.

An interesting point in common between the Ir and Ni results, is that the metal/substrate ISS ratios are smaller, and the O/Ti ratio larger, for deposition of atomic ions, relative to dimers. As Table 1 shows, there is no difference in XPS intensity between atoms and dimers at this impact energy, thus the ISS effect cannot be attributed to a decrease in sticking probability for the atomic ion. While we can only speculate regarding the origin of such subtle effects, a not unreasonable explanation is that the deposited atoms may be binding substitutionally into missing oxygen defect sites. Missing O atoms expose underlying Ti centers, and thus tend to decrease the O/Ti ratio, relative to that for a perfect surface. Ir atoms binding into these defects would block ISS signal from the underlying Ti centers, rather than attenuating O signal, which seems to be the propensity for Ir bound on top of the surface. Both effects would tend to increase the O/Ti ratio, as is observed. Binding into missing O defects might also account for the observed decrease in Ir/substrate ratio, because there might be reduced ISP for scattering from such Ir atoms, because they are in a more electron-rich environment.

2. Effects of impact energy

To probe the dynamics of the Ir/TiO₂ impacts, and to further address the issue of supported cluster structure, ISS was also performed following deposition over a wide range of impact energies. In

comparing different size clusters, it is not clear whether impact dynamics should scale with total energy, total momentum or *per* atom energy or momentum. We have opted to carry out experiments at certain values of energy/atom, i.e., clusters are impacted at certain velocities. For Ir_{10} and Ir_{15} , we also did experiments at lower energy/atom values, so that it is possible to make at least limited comparisons of different clusters at similar total impact energies. The energy/atom range studied is somewhat dependent on cluster size because our $\sim 1\text{eV}$ kinetic energy spread precludes very low energy/atom impacts for small clusters, and the electrometer used to measure cluster current complicates the problem of depositing at high total energies. It should be noted that the spot size (profiled by AES) and beam intensity (i.e., deposition time) are independent of energy over the range studied, so that the observed effects cannot be attributed to spot size or contamination issues.

Fig. 6 compares ISS spectra taken following Ir_2 and Ir_{10} depositions over a wide energy range, and the complete data set is summarized in Table 1. Note that at low energies, both cluster sizes give significant Ir ISS peaks, although the peak intensity decreases with cluster size, as discussed above. With increasing impact energy, the Ir ISS signal decreases substantially – much more than the decrease in Ir XPS intensity (Table 1). For example, at 20 eV/atom, the Ir_2 XPS is still 95% of the low energy value, while the ISS intensity is down to 41%, and the difference is even greater at 40

eV/atom. The XPS results show that most, or all, of the Ir is still in the top few layers of the sample, while ISS shows that for high impact energy, most of the Ir is no longer in the top layer, i.e., the Ir is penetrating into the substrate. For the dimer, the XPS intensity decrease at high energies could be taken as evidence of a decrease in sticking probability, however, penetration also decreases XPS intensity, and the ISS data show that penetration is the dominant effect. For the larger clusters, the XPS intensity remains high as the ISS drops, ruling out significant drops in sticking coefficient.

For larger clusters, the penetration becomes significant at lower *per* atom energies, as can be seen by noting that the ISS decrease for Ir_{10} at 10 eV/atom is greater than for Ir_2 at 20 eV/atom. Such a trend is not surprising – the large, three dimensional clusters transfer large total impact energy and momentum to a relatively small "footprint" on the surface. The more facile penetration observed for the larger clusters raises the question of whether there is already some penetration for Ir_{10} or Ir_{15} at the 1eV/atom energy compared in Figs. 3 and 4. As shown in Table 1, however, the Ir/substrate ISS ratios at 1eV/atom are identical, within the experimental uncertainty, with ratios taken at much lower energies, indication that significant penetration occurs only at higher energies.

The penetration observed for Ir_n at elevated impact energies is quite different from what we observed for Ni_n under identical conditions. For nickel, the Ni/substrate ISS ratio actually increases slightly with increasing impact energy for the larger clusters. We interpreted this effect as indicating that some fraction of the larger Ni clusters may retain multilayer structure when deposited at low energies (though much less so than for Ir_n), and that with increasing energy there is increased tendency to flatten on the surface. As expected for such a scenario, the Ni XPS intensities are independent of impact energy, indicating that all Ni remains on the surface. Note, however, that high impact energy does lead to oxidation of a small fraction of the deposited Ni (to Ni^{+3}), not observed for Ir. The tendency of Ni_n to flatten on the surface while Ir_n penetrates, probably reflects differences in the interaction of the two

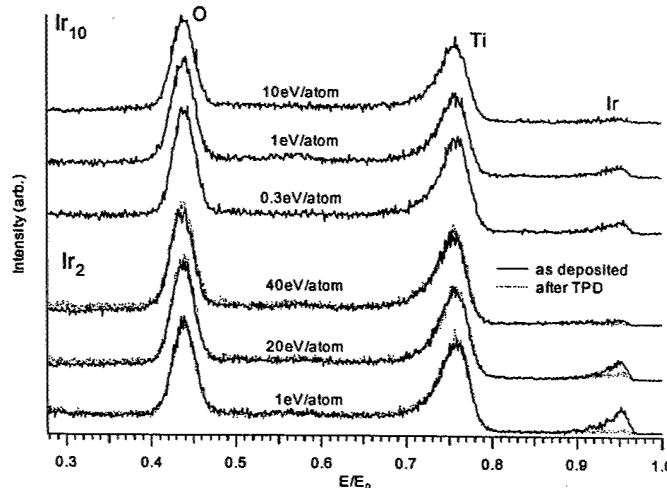


Figure 6. ISS spectra for different deposition energies

metals with TiO_2 , but also is probably influenced by the impact kinematics. The mass of Ir is more than seven times the average atomic mass of TiO_2 , while Ni is only a bit more than twice the average surface atom mass. At a given energy/atom, momentum/atom increases like the square root of atomic mass, thus Ir_n has nearly twice the momentum/atom as Ni_n . This additional momentum should facilitate displacement of surface atoms, enhancing penetration.

In summary, the ISS and sputter-rate results for as-deposited clusters all are consistent with a scenario where clusters deposit at more-or-less intact, on top of the surface for low deposition energies. With increasing impact energy, the clusters begin to penetrate the TiO_2 surface, becoming completely buried for energies above some size-dependent limit. The XPS results show no evidence of cluster-surface redox chemistry even at high impact energies, and also suggest that the sticking coefficient is roughly energy-independent, and probably near unity.

C. Temperature programmed desorption

C^{16}O and C^{18}O adsorption/desorption behavior was studied to further characterize the deposited Ir clusters. As shown above, damage by the ISS He^+ beam increases the density of oxygen defects, and also implants He in the substrate. To minimize the effects of ISS damage, the main TPD experiments were done without pre-TPD ISS characterization. For comparison, we also ran a set of TPD experiments where the TiO_2 substrate was subjected to one 30 second ISS run prior to deposition. The two data sets are similar, but unless specifically noted, the results presented are from the set with no pre-TPD ISS. In addition to C^{18}O and C^{16}O , we monitored desorption of CO_2 (with one or two ^{18}O) and looked for residual surface C by AES, respectively. CO desorption was the only significant channel.

Before describing our CO adsorption/desorption results, it is useful to review the STM results of Solymosi *et al.* [23, 24]. In their experiments Ir nanoparticles were grown by Ir evaporation onto a TiO_2 , (110)-(1x2) support, followed by various annealing treatments. The (1x2) surface differs from our stoichiometric (1x1) surface in that every other row of oxygen atoms is missing. For the lowest Ir coverages used in their experiments, the Ir particle size (1 - 1.5 nm, 8 - 10 atoms) was in the middle of the range we deposit. After imaging the nanoparticles, the samples were exposed to high pressures of CO (10^3 mbar) for several minutes at 300K, after which they were re-imaged. It was found that particles with diameters ~ 1.5 nm (10 atoms), were disrupted to isolated $\text{Ir}(\text{CO})_2$ species. IR spectroscopy was used to identify the dicarbonyl species, and also to follow the CO adsorption/breakup process. The breakup process was slow enough to be time-resolved for 3-4 nm Ir clusters, but too fast to follow by IR spectroscopy for the small clusters. The major difference between their experiment and ours, other than the use of a different TiO_2 surface, was the CO dose. Our doses vary from 0.1 L to 5 L, while their lowest dose was $\sim 10^5$ L. In addition to the particle breakup observed upon CO exposure at 300K, they also examined samples exposed to high CO doses at 600K. At high temperatures, they observed formation of large (several hundred atom) particles. Particle size was also observed to coarsen upon annealing in absence of CO. Based on their results, we can anticipate strong CO adsorption and thermal effects on the clusters.

1. The nature of CO binding, and effects of adventitious CO

The only gas present in the chamber background that adsorbs significantly at room temperature is CO. To quantify the adsorption of adventitious CO on the Ir_n/TiO_2 samples, experiments were run where Ir_n was deposited (in ~ 30 minutes), then the samples were allowed to stand in the deposition chamber until the total time since the beginning of deposition was exactly 1 hour. Both the CO partial pressure and calibration experiments using Ni (100) are consistent with an adventitious CO dose of 0.1 L. These samples were then moved to the TPD station, and a TPD run was performed with no additional CO dosing. Fig. 7 (A) shows the Ir cluster size dependence of the TPD signal for this adventitious CO. No CO desorption is observed in this temperature range from freshly annealed TiO_2 , even following large CO exposures, thus the desorption for Ir_n/TiO_2 samples is clearly associated with Ir. The desorption temperature is in the same range observed for Ir single crystals, [5-7] and shifts slightly to lower temperatures and sharpens as the cluster size increases. Because the sample morphology changes in the course of TPD (see below), the broad desorption feature does not necessarily reflect a distribution of CO

binding sites, and may be affected by the kinetics of thermally driven rearrangement processes.

The solid circles in Fig. 7 (B) represent the integrated desorption peak areas ($T > 400$ K), normalized to the value for Ir_2 . The open circles show the analogous results for desorption following a 5 L CO dose. For the adventitious dose, the CO coverage is found to decrease strongly with

increasing cluster size, whereas the coverage in the 5 L dose is nearly independent of cluster size. A surprising result is that the amount of CO desorbing for the 0.1 L adventitious dose is only a factor of ~ 1.5 to 3 times smaller than for the 5L dose. For reference, a 5L dose corresponds to 1.9×10^{15} CO molecules impinging *per* cm^2 , or about ~ 1.2 times the density of surface atoms, i.e., nearly all exposed Ir atoms will experience a direct CO collision. The 0.1L dose corresponds to 3.8×10^{13} CO molecules/ cm^2 , so that each exposed atom has only about a 2.4% chance for a direct CO collision. Even given the uncertainties of our mass spectrometer sensitivity calibration, it is clear that considerably more CO desorbs from the as-deposited clusters than could be explained if adsorption occurred only in direct CO-on-Ir collisions.

Instead, we conclude that CO must be adsorbing on the TiO_2 , then migrating to stable binding sites in association with Ir clusters. This process has variously been termed “reverse spillover” or substrate mediated adsorption (SMA), and has been discussed by many authors. See for example, the review of Conner and Falconer[25], papers by Henry and co-workers[26], Rumpf *et al.*[27], Boudart and co-workers[28, 29], or Dellwig *et al.*[30]. Because SMA depends mostly on the support, the recent study by Bowker *et al.*[31] of CO SMA on Pd/TiO_2 (110)-(1x1) is particularly relevant to our results. They found that the heat of adsorption of CO on TiO_2 is about 38 kJ/mol, and for a catalyst with 12% coverage of Pd, CO SMA was significant for temperatures up to 330K. In our experiments, the support is at room temperature and the Ir dose is 0.1 ML, thus significant SMA is to be expected. The SMA mechanism can also account for the inverse correlation of adventitious CO coverage with cluster size (Fig. 7(B)). The probability of a CO molecule diffusing to a stable Ir-associated binding site is inversely proportional to the average distance between clusters, which clearly increases with cluster size, particularly if the larger clusters have multilayer structures. In order to interpret the effects, it is useful to work out the maximum possible CO coverage. The 0.1L ($3.8 \times 10^{13}/\text{cm}^2$) adventitious CO dose corresponds to 24% of the 1.6×10^{14} Ir atoms deposited *per* cm^2 as clusters. Therefore, if the SMA mechanism is 100% efficient, the maximum adventitious CO adsorption level is about one CO for every four Ir atoms. Within the uncertainties of our mass spectrometer sensitivity calibration, it appears that the SMA efficiency approaches unity for deposited dimers, decreasing to $\sim 40\%$ for Ir_{15} .

The adventitious CO coverages seen for the as-deposited clusters raises the question of how adventitious CO might affect the clusters and/or our ISS/XPS measurements. The worst-case scenario would be that the deposited clusters are disrupted by interaction with adventitious CO, similar to the effects seen by Solymosi and co-workers. In fact, their experiments show disruption only for very high CO exposures (10^{-3} mbar, $\sim 10^5$ L), and no disruption was seen for lower exposures, still far in excess of our CO exposures.[32] Even without physically disrupting the clusters, however, there could be effects on

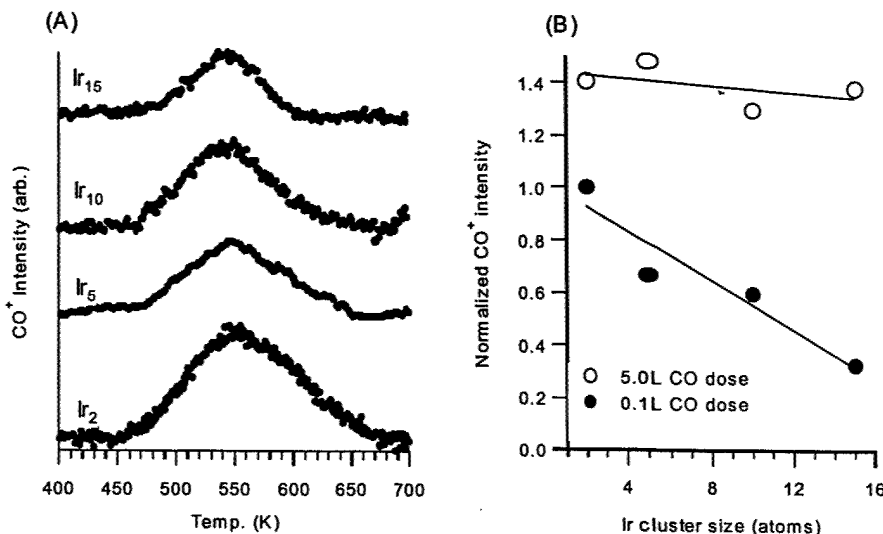


Figure 7 (A) CO TPD spectra for Ir_n/TiO_2 . (B) Integrated desorption yields

XPS or ISS. For XPS, the presence of CO clearly has little effect. We can compare XPS for as-deposited clusters with adventitious CO, clusters grown by very rapid atomic ion deposition where there is little adventitious CO, and clusters with 5 L CO exposures. Within experimental error, there are no shifts in XPS peak positions, and no changes in XPS intensities. ISS, on the other hand, is highly sensitive to adsorbates if they bind so as to attenuate scattering from underlying atoms. This sensitivity raises questions regarding interpretation of the ISS, but also provides an opportunity to probe the nature of the CO binding.

The nature of CO binding was probed by examining the effects of 1 keV He^+ sputtering on the Ir ISS signal. The analysis relies on the expectation that CO should sputter faster than Ir – experimentally, about 30 times faster. For example, a single ISS scan after cluster deposition results in a ~63% decrease in the amount of adventitious CO desorbing in subsequent TPD, but only causes a ~2% decrease in the Ir XPS signal. Consider a sample where CO is bound to Ir in such a way that it attenuates Ir ISS (i.e., on top). In that case, the Ir ISS intensity should increase substantially as the CO is sputtered away, decreasing only after longer sputter times when Ir removal becomes significant. If, on the other hand, CO is bound in such a way that it does not attenuate Ir ISS, then CO removal would result in little change in Ir ISS intensity, which should simply decrease slowly with sputter time. To allow us to monitor the initial stages of the rapid CO sputtering, the He^+ beam intensity was reduced by a factor of ~15 relative to our normal ISS conditions. In addition, only the Ir region of the ISS spectrum was scanned, reducing the He^+ exposure to about 1% of that in a normal ISS survey scan. Under these conditions, no significant sample damage or CO loss is expected during the initial Ir ISS scan.

The results are shown in Fig. 8. Because the intensity is so low, the data have been fit to gaussians, intended only as guides to the eye. Consider the top row of data, showing the results for a 5 L dose on Ir_2 and Ir_{10} . The data have been normalized, and the absolute ISS signal for Ir_2 is a bit more than twice that for Ir_{10} (see Fig. 3). The initial (most intense) ISS spectrum is for as-deposited Ir_n with only adventitious CO. The second (weakest) ISS spectrum was taken immediately after a 5L dose of C^{18}O . This dose is large enough that most of the exposed Ir atoms will have had a direct encounter with CO impinging from the gas phase, in addition to whatever CO is adsorbed via the SMA mechanism. After the 5L dose, the Ir ISS signal decreases by a factor of three (four) for the dimer (10-mer), indicating that the additional

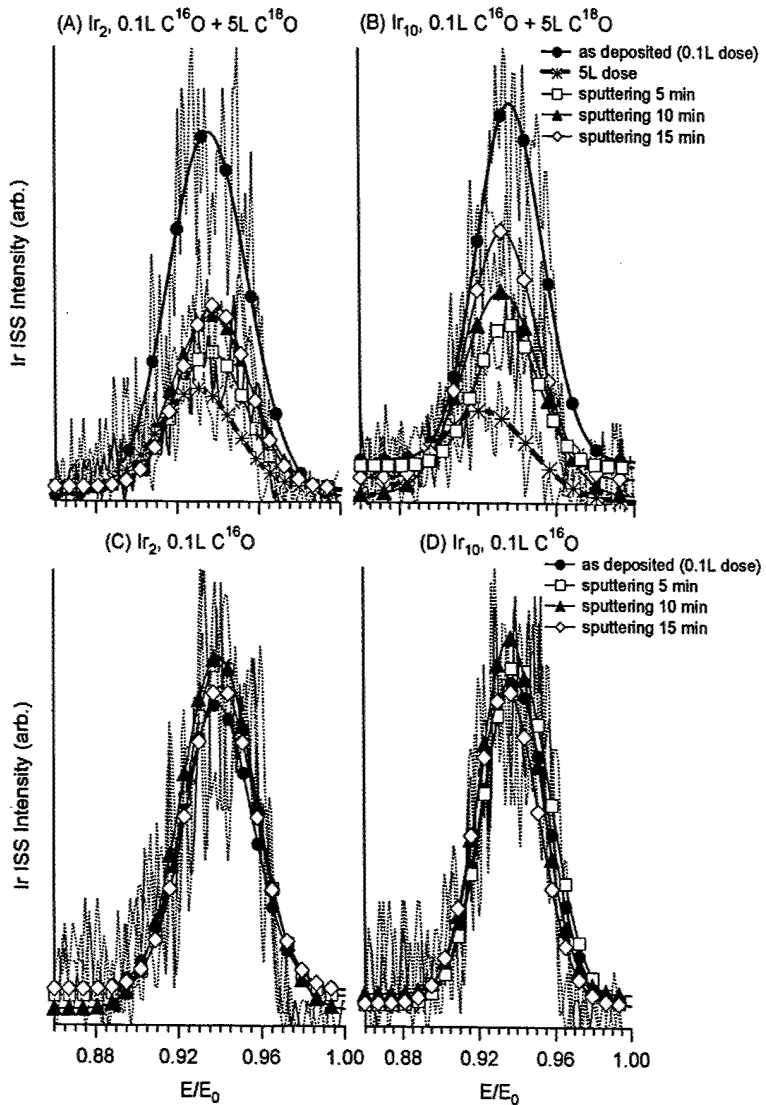


Figure 8. He^+ sputter time dependence of Ir ISS signal

adsorbed CO is bound so that it attenuates Ir ISS. After the 5 L dose, the He^+ beam was left on and ISS spectra were run periodically to examine sputter-induced changes in the Ir ISS signal. As expected from the considerations discussed above, the Ir ISS signal increases significantly as the overlying CO sputters away, exposing Ir. After \sim 15 minutes the Ir signal begins to drop, indicating that enough CO has been lost that the rate of Ir sputtering overtakes the rate at which CO sputtering exposes fresh Ir. The more complete recovery for Ir_{10} is consistent with the lower Ir sputter rates seen for the larger clusters (Fig. 5).

The bottom row shows the same experiment, but without the 5 L saturation dose. In this case, the sputter-induced increase in Ir ISS signal is much smaller. The maximum Ir ISS signal appears after \sim 10 minutes (compared to 15 min for the 5L dose), and is only 15% greater than the signal for as-deposited clusters. Based on the observation that \sim 63% of adventitious CO is lost in one 30 second, high He^+ intensity ISS survey scan, 10 minutes under low flux conditions should remove \sim 70% of the CO, assuming single exponential time dependence. If we extrapolate the 15% Ir ISS increase observed for \sim 70% CO removal, we can crudely estimate that adventitious CO adsorption results in only \sim 20% attenuation of Ir ISS signal, relative to the signal expected in absence of CO. Because this 20% attenuation is small compared to the large changes in Ir ISS intensity with cluster size and impact energy, we conclude that the adventitious CO coverage does not significantly affect interpretation of the ISS results. In fact, the CO effect on the ISS survey data is probably only \sim 10%, because we expect that about half the CO is already lost during the \sim 20 seconds it takes to reach the Ir region in an ISS survey scan.

The data in Fig. 8 also suggest the more surprising conclusion that adventitious CO tends to bind into different sites than CO adsorbed in the 5 L exposure. For the moment, assume that there is no difference in binding geometry, and recall (Fig. 7B) that the CO coverage following the 5 L dose only increases by a factor of 1.5 to 2 (for Ir_2 and Ir_{10}) compared to the adventitious coverage. Comparison with the \sim 20% ISS attenuation inferred for the adventitious exposure, implies that the 5 L exposure should cause 30% or 40% (Ir_2 , Ir_{10}) attenuations, relative to hypothetical samples with no CO. In other words, the 5 L dose should result in only 10 to 20% (Ir_2 , Ir_{10}) reduction in Ir ISS signal, relative to the as-deposited samples with adventitious CO. As Fig. 8 shows, the actual reductions are \sim 75%. We conclude that CO impinging on Ir directly from the gas phase in the 5 L exposure, tends to bind on top, where it results in strong attenuation. Adventitious CO, almost entirely adsorbing via SMA, appears to binding primarily into sites, possibly around the periphery of the clusters, where it does not tend to attenuate Ir ISS. The idea that SMA and direct impingement populate different sites is also supported by the TPD results, discussed next.

2. CO exchange, and the effects of TPD on the clusters.

Fig. 9 shows a series of TPD experiments for Ir_2 and Ir_{10} . It should be noted that each data set (A - F) represents a separate deposition on freshly annealed TiO_2 . Traces A and D show the signal for C^{16}O desorbing from as-deposited clusters, i.e., desorption of the adventitious ("0.1L") dose. In addition to the main peak at \sim 550K, there is a small feature starting at the initial heating temperature, and peaking \sim 340K. This feature is also present for clean TiO_2 , and is attributed to CO bound at defects on the TiO_2 surface, consistent with the results of Linsebigler *et al.* for CO TPD from $\text{TiO}_2(110)$ -(1x1).[33] The middle set of spectra shows desorption of both C^{16}O and C^{18}O (and total = $\text{C}^{16}\text{O} + \text{C}^{18}\text{O}$) for as-deposited clusters that were dosed with 0.5L of C^{18}O , prior to the TPD experiment. By comparing the bottom and middle data sets, it can be seen that the TiO_2 defect sites responsible for the low temperature feature undergo complete $\text{C}^{16}\text{O} \rightarrow \text{C}^{18}\text{O}$ exchange. In the top set of spectra, the as-deposited clusters have been subjected to a 5L C^{18}O dose, and as expected, the TiO_2 defect-bound CO is entirely exchanged. The run-to-run variations in the intensity of the low temperature feature reflect the fact that each data set is a separate experiment, with some variation in the concentration of defects capable of binding CO at room temperature. Because it is clearly not associated with Ir, this low temperature feature has been omitted in the peak integrations used to generate Fig. 7 (B).

The behavior for the Ir-associated high temperature feature is more complicated. Consider first Ir_2 . For the 0.1L $\text{C}^{16}\text{O} + 0.5\text{L C}^{18}\text{O}$ dose sequence (middle data set), roughly equal amounts of C^{16}O and C^{18}O desorb, but with distinct temperature dependences. The C^{16}O feature has intensity, shape, and peak

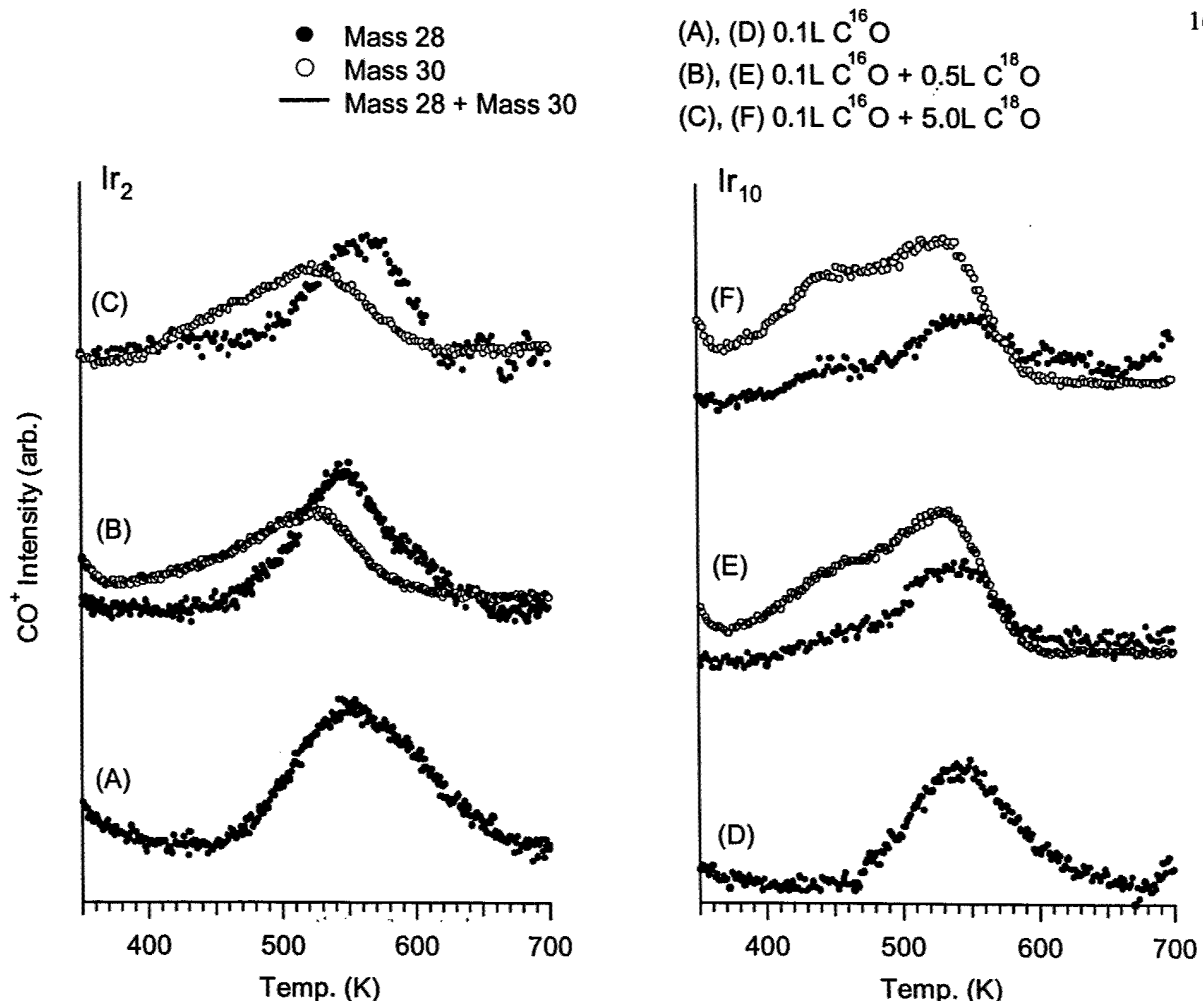


Figure 9. CO TPD from Ir_2 and Ir_{10} following different CO exposure sequences

temperature similar to that for C^{16}O in the bottom frame, while the C^{18}O feature is shifted to significantly lower temperature. Evidently for the dimer, adventitious C^{16}O bound via SMA is mostly in sites stable enough to resist $\text{C}^{16}\text{O} \rightarrow \text{C}^{18}\text{O}$ exchange during the subsequent 0.5 L room temperature C^{18}O exposure. In addition, the lower peak desorption temperature for C^{18}O suggests that the SMA-populated sites are nearly saturated by the adventitious exposure, forcing the later-arriving C^{18}O into less stable sites. From the sputtering results, we tentatively identify the more stable SMA sites as being peripheral (little Ir ISS attenuation), and the less stable sites being somehow on top of the clusters, where Ir ISS attenuation is strong. For the 0.1L C^{16}O + 5.0L C^{18}O dose sequence (top data set), most of the C^{16}O is still not exchanged, and the main effect of the higher dose is additional broadening of the C^{18}O feature toward lower temperatures, with some evidence of bi-modal behavior in the total CO desorption spectrum.

For the larger clusters exemplified by Ir_{10} , the effects of the 0.5L and 5.0L C^{18}O doses are larger than for Ir_2 , and qualitatively different. With increasing C^{18}O dose, there is significant suppression of the C^{16}O peak, relative to the intensity from the adventitious dose alone (bottom spectrum). Clearly, there is substantial $\text{C}^{16}\text{O} \rightarrow \text{C}^{18}\text{O}$ exchange at room temperature for the larger clusters. Furthermore, C^{16}O and C^{18}O have similar bi-modal desorption features, unlike the case of Ir_2 , where C^{16}O and C^{18}O desorb in separate peaks. Evidently, $\text{C}^{16}\text{O} \rightarrow \text{C}^{18}\text{O}$ exchange not only removes C^{16}O , but can also displace it into less stable sites. The C^{16}O removal must occur at room temperature, but the site exchange may also occur during the TPD heating. It is not clear why the larger clusters ($n > 4$) show $\text{C}^{16}\text{O} \rightarrow \text{C}^{18}\text{O}$ exchange, while the dimer does not. As Fig. 7 shows, there is some decrease in CO binding energy with increasing cluster size, but the effect is too small to account for the qualitatively different behavior for Ir_2 . More likely, the

difference relates to the multilayer structure of the as-deposited larger clusters. It is possible, for example, that as-deposited multilayer clusters rearrange to two dimensional structures upon CO exposure, in order to increase the number of the stronger binding peripheral sites. Such rearrangement might also explain why the additional CO uptake in the 5 L exposure is much greater for the larger clusters (Fig. 7 (B)).

Several observations make it clear that the heating cycle used in TPD has a major effect on the morphology of the supported clusters. As noted, we typically run two or three sequential TPD scans on each sample, and the temperature dependence of the CO desorption during the first scan is quite different from those observed in the subsequent scans. This effect can be seen for the case of Ir_2 deposited at 1 eV/atom in the top set of TPD curves in Fig. 10 (A). Note that the amount of CO desorbing is substantially smaller for the second scan, and the desorption peak is shifted to lower temperatures. Similar effects are seen for the larger clusters. Third TPD scans are found to be very similar to the second scans, indicating that the TPD-induced changes in the samples are largely complete in a single scan.

The ISS and XPS results provide some insight into the nature of the TPD-induced changes. The dotted curves in Fig. 3 show the ISS data obtained just after the set of TPD runs. Note that the Ir ISS signal is greatly reduced, and becomes nearly independent of cluster size. Low ISS intensity implies that most of the deposited Ir is no longer on the surface of the sample. One interpretation might be desorption of Ir as some carbonyl compound, too heavy to be monitored by the mass spectrometer used for TPD. Ir desorption can be ruled out, however, based on the XPS results shown in Fig. 2, where the post-TPD spectra are given as dotted curves. For the 1 eV/atom data, the post-TPD XPS intensities are at least 75% of the values for the as-deposited clusters, indicating that most of the Ir is still in the near-surface region. The TPD-induced attenuation of Ir ISS and XPS signals, relative to their pre-TPD values, are summarized in Fig. 10 (B) for the depositions at 1 eV/atom. Particularly for the small clusters, the attenuations are large – 80% for ISS and 25% for XPS. Similar effects are observed for heating without CO exposure,

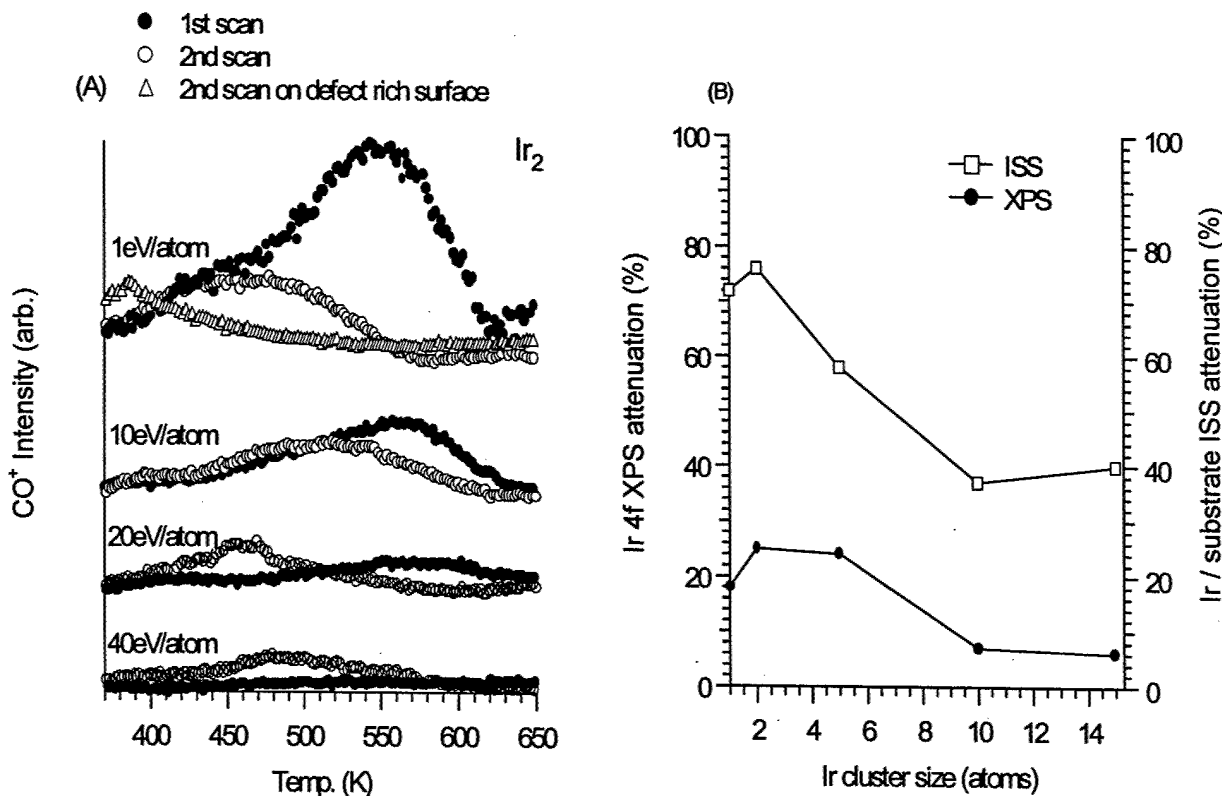


Figure 10. Left: Comparison of TPD for different impact energies, and comparison of 1st and 2nd TPD scans. Right: Percent decreases in ISS and XPS after TPD

indicating that the morphology changes are driven thermally.

Comparison of the ISS and XPS results shows that while the Ir is no longer in the top-most layer of the sample, most of the Ir is still present in the near-surface region. There are two obvious mechanisms that might account for this morphology change. The Ir might be sintering into larger, multilayer particles, where the Ir in the lower layers is invisible to ISS and detected with reduced sensitivity by XPS. The average particle thickness would need to be about three layers to account for the ISS and XPS attenuations. Alternatively, it might be that the clusters are partially encapsulated during TiO_2 annealing. TiO_2 is a reducible support, and many metal/ TiO_2 catalysts show evidence of strong metal support interaction (SMSI) upon heating, particularly under reducing conditions. In most studies the SMSI state is deduced from changes in activity, or from appearance of Ti^{+3} in XPS. In more detailed studies, it has been shown that SMSI can be accompanied by encapsulation of the metal nanoparticles by a TiO_x layer. See, for example, the review by Persaud and Madey[34] or the recent study by Diebold and coworkers,[35] which provides a textbook example of Pt nanoparticle encapsulation upon annealing of Pt/ TiO_2 . In the latter paper, they were able to image the TiO_x encapsulating layer by STM, and reported a post-anneal Pt ISS spectrum that is very similar to our post-TPD Ir ISS. From our results alone, we cannot distinguish between the sintering and encapsulation mechanisms, as both would result in large ISS reductions and smaller reductions in XPS intensity. Sintering was inferred to occur upon annealing in the STM experiments of Solymosi and co-workers for Ir on $\text{TiO}_2(110)-(1\times 2)$, however, their post-anneal STM images were not atomically resolved, thus it is not clear that they would have detected the presence of a thin TiO_x layer. Belton *et al.*[36] studied CO desorption chemistry from titania-supported Rh particles, where encapsulation of the Rh particles by TiO_x was observed after annealing to 760K. Encapsulation reduced the main desorption peak attributed to Rh-bound CO, and generated an additional desorption peak at lower temperature, associated with formation of the TiO_x encapsulating layer. Our results are qualitatively similar, supporting the encapsulation mechanism.

The TPD data also suggest an interesting role of defects in the Ir/ TiO_2 system. The data indicated by filled and open circles in the top frame of Fig. 10 (A) shows data for Ir_2 deposited on freshly annealed TiO_2 , where the estimated surface missing oxygen defect density is relatively low. We also studied TPD from TiO_2 subjected to two ISS scans, estimated to increase the defect density to $\sim 18\%$. As already mentioned, the additional defects (missing oxygen and implanted He) have little effect on the first TPD scan (not shown) other than a slight increase in the intensity of the low temperature peak ($T_{\text{peak}} \approx 340\text{K}$) attributed to CO bound at TiO_2 defect sites. On the other hand, the ISS-generated defects have a large effect on the TPD-induced morphology changes, as shown by the second TPD scan (open triangles, Fig. 10 (A)). Note that the amount of CO desorbing and the desorption temperature are both dramatically reduced, relative to the 2nd TPD scan for the samples not analyzed by ISS, suggesting that the presence of defects enhances the encapsulation process, or possibly changes the stoichiometry of the encapsulating layer.

Finally, Fig. 10 (A) also shows the effects of deposition energy on the TPD behavior for Ir_2 . Note that as deposition energy is increased, the amount of CO desorbing in the first TPD scans decrease, but the temperature dependence is not strongly affected. By 40 eV/atom there is no CO desorption, consistent with the conclusion from ISS that no Ir remains on the surface at this energy. Somewhat surprisingly, significant CO desorption reappears in a second TPD scan, suggesting that the initially implanted Ir_n are migrating closer to the surface, where they can influence CO binding.

References

- [1] M. Li, W. Hebenstreit, and U. Diebold, "Oxygen-induced restructuring of the rutile $\text{TiO}_2(110)(1\times 1)$," *Surf. Sci. Lett.*, vol. 414, pp. 951-951, 1998.
- [2] L. Lapicki, K. Boyd, and S. L. Anderson, "Kinematic sample mounting system for accurate positioning of transferable samples," *J. Vac. Sci. Technol. A*, vol. 18, pp. 2603, 2000.
- [3] U. Heiz, F. Vanolli, L. Trento, and W.-D. Schneider, "Chemical reactivity of size-selected supported clusters: An experimental setup," *Rev. Sci. Instrum.*, vol. 68, pp. 1986-1994, 1997.

- [4] J.-M. Pan, U. Diebold, L. Zhang, and T. E. Madey, "Ultrathin reactive metal films on TiO₂(110): growth, interaction, and electronic structure of chromium films," *Surf. Sci.*, vol. 295, pp. 411-426, 1993.
- [5] B. E. Nieuwenhuys and G. A. Somorjai, "Adsorption of carbon monooxide, oxygen, hydrogen, nitrogen, ethylene and benzene on an iridium (110) surface; correlation with other iridium crystal faces," *Surf. Sci.*, vol. 72, pp. 8-32, 1978.
- [6] J. L. Taylor, D. E. Ibbotson, and W. H. Weinberg, "The chemisorption of CO on clean and oxidized Ir(110)," *J. Chem. Phys.*, vol. 69, pp. 4298-4310, 1978.
- [7] D. I. Hagen, B. E. Nieuwenhuys, G. Rovida, and G. A. Somorjai, "Low energy electron diffraction, auger electron spectroscopy, and thermal desorption studies of chemisorbed CO and O₂ on the (111) and stepped [6(111)X(100)] iridium surfaces," *Surf. Sci.*, vol. 57, pp. 632-650, 1976.
- [8] C. D. Wagner, A. V. Naumkin, A. Kraut-Vass, J. W. Allison, C. J. Powell, and J. R. R. Jr., "NIST X-ray Photoelectron Spectroscopy Database," *NIST Standard Reference Database 20, Version 3.2 (Web Version)*, 2000.
- [9] J. Escard, B. Pontvianne, and J. P. Contour, "Photoelectron spectroscopy study of the metal-support interactions in catalysts having iridium deposited on metallic oxides," *J. Electron Spectrosc. Relat. Phenom.*, vol. 6, pp. 17, 1975.
- [10] M. Aizawa, S. Lee, and S. L. Anderson, "Sintering, oxidation, and chemical properties of size-selected nickel clusters on TiO₂ (110)," *J. Chem. Phys.*, vol. 117, pp. 5001-5011, 2002.
- [11] Y. Takasu, R. Unwin, B. Tesche, and A. M. Bradshaw, "Photoemission from palladium particle arrays on an amorphous silica substrate," *Surf. Sci.*, vol. 77, pp. 219-232, 1978.
- [12] M. G. Mason, "Electronic structure of supported small metal clusters," *Phys. Rev. B*, vol. 27, pp. 748-762, 1983.
- [13] M. K. Bahl, S. C. Tsai, and T. W. Chung, "Auger and photoemission investigations of the platinum-SrTiO₃ (100) surface: relaxation and chemical -shift effects," *Phys. Rev. B*, vol. 21, pp. 1344, 1980.
- [14] L. Oberli, R. Monot, H. J. Mathieu, D. Landolt, and J. Buttet, "Auger and X-ray photoelectron spectroscopy of small Au particles," *Surf. Sci.*, vol. 106, pp. 301-307, 1981.
- [15] C. J. Powell and A. Jablonski, *NIST Electron Inelastic-Mean-Free-Path Database - Version 1.1*. Gaithersburg, MD: National Institute of Standards and Technology, 2000.
- [16] M. Aizawa, S. Lee, and S. L. Anderson, "Sintering, Oxidation, and Chemical Properties of Size-Selected Nickel Clusters on TiO₂ (110)," *J. Chem. Phys. (submitted)*, vol. 1, 2002.
- [17] J. P. Espinos, A. Fernandez, A. R. Gonzalez-Elipe, and G. Munuera, "Electronic interaction of Ni particles with TiO₂ and SiO₂," *Surf. Sci.*, vol. 251/252, pp. 1012-1017, 1991.
- [18] V. Vijayakrishnan and C. N. R. Rao, "An investigation of transition metal clusters deposited on graphite and metal oxide substrates by a combined use of XPS, UPS, and Auger spectroscopy," *Surf. Sci. Lett.*, vol. 255, pp. L516-L522, 1991.
- [19] A. Fritsch, Legare, P., "XPS study of small iridium clusters: comparison with the Ir₄(CO)₁₂ molecule," *Surf. Sci.*, vol. 145, pp. L517-L523, 1984.
- [20] P. G. Bertrand and J. W. Rabalais, "Ion scattering and recoiling for elemental analysis and structure determination," in *Low Energy Ion-Surface Interactions*, J. W. Rabalais, Ed. Chichester: Wiley, 1994, pp. 55-116.
- [21] O. S. Oen, "Universal shadow cone expressions for an atom in an ion beam," *Surf. Sci.*, vol. 131, pp. L407-11, 1983.
- [22] R. Pala, F. Liu, and T. Truong, 2003.
- [23] A. Berko and F. Solymosi, "Effects of different gases on the morphology of Ir nanoparticles supported on the TiO₂ (110)-(1x2) surface," *J. phys. Chem. B*, vol. 104, pp. 10215-21, 2000.
- [24] A. Berko and F. Solymosi, "CO-induced changes of Ir nanoparticles supported on TiO₂ (110)-(1X2) surface," *Surf. Sci.*, vol. 411, pp. L900-L903, 1998.

- [25] J. W C Conner and J. L. Falconer, "Spillover in heterogeneous catalysis," *Chem. Rev.*, vol. 95, pp. 759-788, 1995.
- [26] C. R. Henry, "Catalytic activity of supported nanometer-sized metal clusters," *Appl. Surf. Sci.*, vol. 164, pp. 252-259, 2000.
- [27] F. Rumpf, H. Poppa, and M. Boudart, "Oxidation of carbon monoxide on palladium: Role of the aluminum support," *Langmuir*, vol. 4, pp. 722-728, 1988.
- [28] M. Boudart, M. A. Vannice, and J. E. Benson, "Adlineation, portholes, and spillover," *Zeitschrift fuer Physikalische Chemie (Muenchen, Germany)*, vol. 64, pp. 171-7, 1969.
- [29] M. Boudart, "On the nature of spilt-over hydrogen," *Journal of Molecular Catalysis A: Chemical*, vol. 138, pp. 319-321, 1999.
- [30] T. Dellwig, J. Hartmann, J. Libuda, I. Meusel, G. Rupprechter, H. Unterhalt, and H.-J. Freund, "Complex model catalysts under UHV and high pressure conditions: CO adsorption and oxidation on alumina-supported Pd particles," *J. Mol. Catal. A: Chem.*, vol. 162, pp. 51-66, 2000.
- [31] M. Bowker, P. Stone, R. Bennett, and N. Perkins, "CO adsorption on a Pd/TiO₂ model catalyst," *Surf. Sci.*, vol. 497, pp. 155-165, 2002.
- [32] A. Berko and F. Solymosi, 2003.
- [33] A. Linsebigler, G. Lu, and J. John T Yates, "CO chemisorption on TiO₂: Oxygen vacancy site influence on CO adsorption," *J. Chem. Phys.*, vol. 103, pp. 9438-9443, 1955.
- [34] R. Persaud and T. E. Madey, "Growth, structure, and reactivity of ultrathin metal films on TiO₂ surfaces," *Chemical Physics of Solid Surfaces*, vol. 8, pp. 407-447, 1997.
- [35] O. Dulub, W. Hebenstreit, and U. Diebold, "Imaging cluster surfaces with atomic resolution. The strong metal-support interaction state of Pt supported on TiO₂(110)," *Phys. Rev. Lett.*, vol. 84, pp. 3646-3649, 2000.
- [36] D. N. Belton, Y.-M. Sun, and J. M. White, "Chemisorption of CO, NO, and H₂ on transition metal-titania thin film model catalysts," *J. Catal.*, vol. 102, pp. 338-347, 1986.

Publications acknowledging AFOSR support:

"Kinematic sample mounting system for accurate positioning of transferrable samples", Adam Lapicki, Kevin J. Boyd, and Scott L. Anderson, J. Vac. Sci. Technol. A18 (2000) 2603-5. (winner of the American Vacuum Society's / Vacuum Technology Division Shop Note Award for 2001)

"Sintering, Oxidation, and Chemical Properties of Size-Selected Nickel Clusters on TiO_2 (110)", by Masato Aizawa, Sungsik Lee, and Scott L. Anderson, J. Chem. Phys. 117 (2002) 5001-11

"Deposition dynamics and chemical properties of size-selected Ir clusters on TiO_2 ", Masato Aizawa, Sungsik Lee, and Scott L. Anderson, (to be submitted March 2003).

SHOP NOTES

These are "how to do it" papers. They should be written and illustrated so that the reader may easily follow whatever instruction or advice is being given.

Kinematic sample mounting system for accurate positioning of transferrable samples

Adam Lapicki,^{a)} Kevin J. Boyd,^{b)} and Scott L. Anderson^{c)}

Department of Chemistry, University of Utah, 315 South, 1400 East, Salt Lake City, Utah 84112

(Received 4 May 2000; accepted 3 July 2000)

A design is reported for a system of transferrable sample holders and mating experimental stations, that allows samples to be transferred between preparation and analysis tools with high positional accuracy. The sample holders are designed to be manipulated/transported using standard "ESCA stub" compatible hardware. Provisions are made for heating, cooling, and temperature measurement. © 2000 American Vacuum Society. [S0734-2101(00)08805-9]

I. INTRODUCTION

We recently completed construction of an experiment designed for metal cluster ion deposition in ultrahigh vacuum (UHV), and analysis of the physical and chemical properties of the deposits.¹ The deposited spot size is 800 μm in diameter, thus one requirement for the experiment was a method for positioning samples precisely with respect to the preparation and analysis tools. Normally one would mount the sample on a precision manipulator, and calibrate the manipulator setting for alignment with each experimental tool. One of our tools is scanning tunneling microscope (STM), requiring a sample transfer onto the vibration-isolated STM baseplate. Further complicating the problem was the constraint that experimental tools are distributed over three, interconnected UHV chambers, and that the sample must be transportable and mountable in both vertical and horizontal orientations. Finally, the vacuum system was partly built around a VG ESCALAB II spectrometer, and it was desirable to retain compatibility with the existing VG sample manipulation and transport hardware. To meet these requirements, we developed a system of sample holders and mating docking stations. Samples are mounted on one of a set of sample holders, then loaded into the vacuum system through a vacuum lock, after which they can be transported and inserted into any of the experimental stations.

II. DESIGN

The transportable sample holder is shown in Fig. 1. The maximum size of the holder was constrained by the require-

ment that it, together with the existing VG transporter, has to pass through the 28 mm diameter valves that isolate the UHV chambers. To allow manipulation in both vertical and horizontal orientations, the holder is equipped with two manipulation stubs perpendicular to each other. Their dimensions match those of so-called ESCA stubs popularized by VG and VSW, allowing manipulation with both conventional wobble stick forks and coaxial pincer grip wobble sticks.

The sample holder can be inserted into two types of sockets. To accommodate transport in the ESCALAB's horizontal transporter and for mounting into low precision sample parking stations, the holder is equipped with an ESCA stub-compatible pin that mates to simple cylindrical sockets (available from VG, VSW, and others). The sockets have a retaining spring that engages the annular bulge on the bottom of the pin, thus securing the sample, and compensating for its asymmetric mass distribution. This mounting arrangement is used only in the horizontal (mounting pin down) orientation. The two manipulation stubs and the mounting pin are welded to a bridge piece that is screwed to the main body of the sample holder.

For precise mounting in any orientation, the sample holder is equipped with semicylindrical rails on either side. The radius of curvature of the rails is 3.17 mm, and the rails are machined at an angle of 8° with respect to the symmetry plane of the holder. These rails engage mating V grooves in the mounting stations, a typical example of which is shown in Fig. 2. As shown, the station has two V grooves machined at 8° angle with respect to the symmetry plane, with dimensions such that the sample center is positioned at the center of the station when the holder is fully inserted. The V-groove pieces are screwed to a base mount that holds them at a precise separation. The 8° angle is a compromise. A larger (~45°) angle would give more precise sample positioning (for given machining accuracy) but the V grooves would not engage the semicylindrical rails until the sample was almost

^{a)}Present address: Information Storage Materials Laboratory, Toyota Technological Institute, 2-12-1 Hisakata, Tempaku-ku, Nagoya 468-8511, Japan.

^{b)}Present address: Department of Chemistry, University of New Orleans, New Orleans, LA 70148.

^{c)}Author to whom correspondence should be addressed; electronic mail: anderson@chemistry.utah.edu

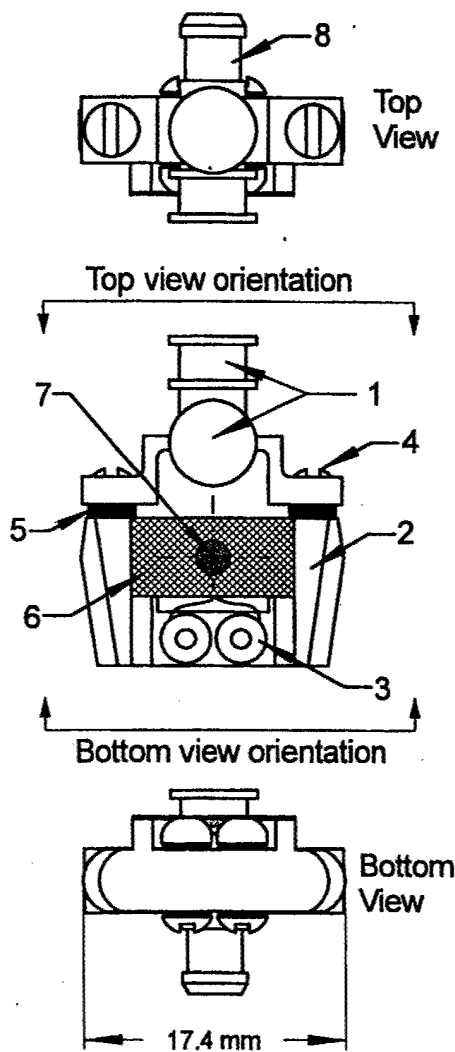


FIG. 1. Sample holder: (1) stubs for manipulation with wobble sticks; (2) V-shaped holder body with semi-cylindrical side rails; (3) thermocouple connectors; (4) mounting screws; (5) spacers; (6) foil mounting the sample to the holder; (7) substrate (sample) for surface studies; (8) pin for mounting in ESCA stub mounts.

completely inserted. Several of our sample stations have poor visibility for sample transfer, and wobble stick manipulators give poor tactile feedback. As a consequence, one design requirement was that the sample holders self-align as they are inserted into sample stations.

Several sample stations are vertically oriented (deposition, vertical transporter, and STM stations), and the samples can be lowered into the station, where they self-align due to gravity. In others, the sample is horizontal [sputter/anneal and temperature-programmed desorption (TPD)] or can be rotated to any angle (angle-resolved XPS). For these stations, a ball-detent mechanism (Fig. 3) is used to lock the sample holder into the station. The spring-loaded balls engage angled shoulders machined into the upper end of the cylindrical rails on both sides of the holders. The geometry is such that the squeezing force of the balls is converted to a net force that pushes the holder deeper into the V-groove socket.

Samples are mounted to the backside of a thin tantalum

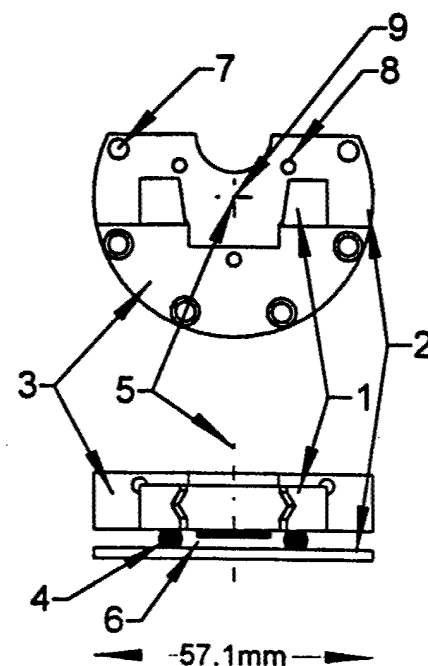


FIG. 2. Example sample station (ion deposition station): (1) angled V-groove pieces; (2) mounting plate with deposition mask; (3) base mount for V-groove pieces; (4) ruby balls for positioning and electrical isolation; (5) beamline axis; (6) sample position; (7) holes for mounting screws; (8) holes for ruby balls; (9) the mask aperture for ion beam deposition.

(or other metal) strip, with the experimental surface exposed through a 5 mm diameter hole. This mounting arrangement assures that the sample plane is independent of sample thickness. Just below the sample are two buttons machined from thermocouple materials that are thermally and electrically insulated from the main body of the holder. Thin thermocouple wires are attached directly to the sample and connected to the buttons by spot welding. Where needed, the sample stations are equipped with spring-loaded contact electrodes (not shown in Fig. 2), also machined from the thermocouple materials, which make contact with the buttons.

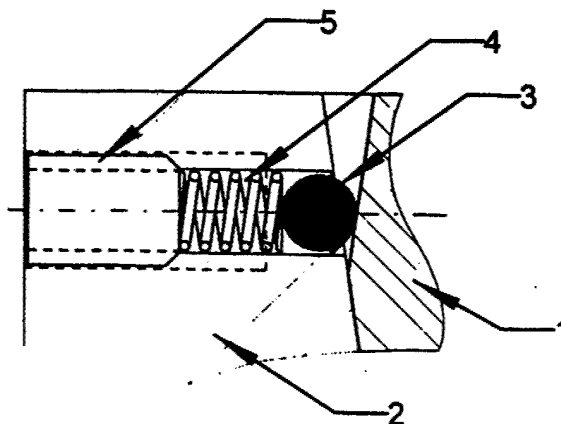


FIG. 3. Ball-detent locking mechanism for the sample stage: (1) sample mount; (2) V-groove piece of sample station; (3) 3/32 in. (~2.38 mm) stainless steel ball; (4) stainless steel spring; (5) set screw.

The samples can be cooled by liquid nitrogen cooling the entire sample station, and this feature is incorporated in the XPS and TPD stations. An additional benefit of the ball-detent mechanism incorporated in these stations is that it forces the holder into good contact with the station, improving cooling. Two schemes are used for heating. For low temperature heating, the entire holder/station is heated, thus warming the sample by conduction. This method is of limited usefulness because of significant undesired gas desorption from the station and holder surfaces. For annealing and for TPD, we use electron-bombardment heating from the back side of the sample. Our anneal stage has a filament assembly that can be translated to position the filament only a few millimeters behind the sample, providing up to 50 mA of electron current onto the sample back. The thermal conductivity of the tantalum sample mounting strip is low enough to allow sample temperatures over 1000 °C with minimal heating of the sample holder and station. If necessary, the sample station and holder could be cooled during annealing, but this has not been implemented. For TPD, the electron gun is positioned several centimeters below the sample surface, and electron lenses are used to focus the beam on the sample back. Sample temperature is controlled by controlling the emission current and acceleration voltage.

The positional precision of the holder/station combination is largely a function of the machining accuracy, specified at ± 0.001 in. There are three useful measures of positional accuracy. For a given sample holder/sample station combi-

nation, the positional repeatability for multiple insertions is measured to be between 15 and 25 μm , depending on the sample holder. For a particular sample holder, moving between sample stations, the positioning accuracy in the x - y directions (z is the sample normal) is better than 50 μm . For the entire set of sample holders combined with all sample stations, the standard deviation in (x - y) position is $\sim 75 \mu\text{m}$. Given our 800 μm deposition spots, this accuracy is adequate, although we estimate that accuracy could be improved to $\sim 25 \mu\text{m}$ across all holder/station combinations by standard high precision machining. The z positional accuracy is significantly worse, because the tantalum sample mounting strip tends to buckle irreversibly during annealing.

Detailed drawings of the sample holder/mount are available upon request to the corresponding author (SLA).

ACKNOWLEDGMENTS

The authors would like to thank Dennis Romney, Mark Petzel, and Jeff Welch in the Chemistry machine shop for helpful suggestions and for constructing the holders and stations. Brent Mantooth assisted in the design of the TPD stage. This work was supported by the Air Force Office of Scientific Research under Grant Nos. F49620-96-1-0119 and F49620-00-1-0138.

¹K. J. Boyd, A. Lapicki, M. Aizawa, and S. L. Anderson, *Rev. Sci. Instrum.* **69**, 4106 (1998).

Sintering, oxidation, and chemical properties of size-selected nickel clusters on $\text{TiO}_2(110)$

Masato Aizawa, Sungsik Lee, and Scott L. Anderson^{a)}

Department of Chemistry, University of Utah, Salt Lake City, Utah 84112

(Received 11 March 2002; accepted 12 June 2002)

We report a study of Ni_n/TiO_2 samples prepared by size-selected deposition of Ni_n^+ ($n = 1, 2, 5, 10, 15$) on rutile $\text{TiO}_2(110)$. The effects of deposition energy and support preparation conditions on the oxidation state of the clusters are examined by x-ray photoelectron spectroscopy (XPS). On the stoichiometric surface, Ni_n is stable, but oxidation can be driven by increased impact energy. For TiO_2 surfaces with chemisorbed oxygen, deposited Ni_n are oxidized even at low impact energies. Low energy ion scattering spectroscopy was used to characterize the dispersion of Ni on the support, and provide some insight into binding morphology. Small clusters bind preferentially to oxygen sites. Large clusters bind in compact geometries and appear to retain some three dimensional character on the surface. The data suggest that the clusters neither fragment, nor agglomerate, in room temperature deposition. Temperature programmed desorption (TPD) of CO was used to characterize deposited clusters. For these small clusters, no strong desorption features are observed in the temperature range above 140 K, where CO desorbs from TiO_2 . The lack of CO binding is discussed in terms of strong Ni– TiO_2 binding. The ion scattering data indicate that there is significant sintering, and possibly partial encapsulation, of the Ni clusters during the TPD experiments. XPS reveals little change in oxidation state. This is the first study where the oxidation state and morphology of size-selected deposited clusters has been studied, before and after TPD.

© 2002 American Institute of Physics. [DOI: 10.1063/1.1498477]

I. INTRODUCTION

Deposition of mass-selected metal clusters on metal oxide supports has been shown by Heiz and co-workers to be an important tool for studying the effects of cluster size and support defects on catalytic activity.^{1–5} Recently they have shown a size dependence for the interaction of CO with Ni_n ($n < 30$) supported on ultrathin MgO (110) films, using temperature programmed desorption (TPD) and infrared spectroscopy.^{2,3} The binding of CO to Ni clusters on MgO is strong, as shown by the appearance of nickel carbonyl species in the thermal desorption mass spectra for the small clusters ($n < 4$). Only CO desorption is observed for the larger clusters (Ni_n , $n = 11, 20$, and 30). They found two types of CO adsorption sites. On one, CO chemisorbs molecularly, resulting in a desorption between 200–300 K. On the second site, CO is dissociated and desorbs associatively between 500–600 K.

We recently built an instrument that allows us to investigate physical and chemical properties of mass-selected metal clusters deposited on metal oxides. The capabilities are somewhat complementary to those of Heiz and co-workers, including TPD, x-ray photoelectron spectroscopy (XPS), and ion-scattering spectroscopy (ISS), but not infrared spectroscopy. The inclusion of ISS is important, because it provides a measure of changes in cluster morphology with deposition energy, cluster size, and following TPD. Here we report a study of oxidation, sintering, and CO-adsorption behavior of

Ni_n deposited on TiO_2 at different deposition energies, and with different TiO_2 preparation conditions. For comparison, we also studied Ni particles grown by deposition of a 1.0 ML dose of nickel atoms. TiO_2 was chosen as the initial support for study because we wanted a system where the metal-support binding would be strong enough to minimize diffusion and sintering of the deposited clusters at room temperature. The results are quite different from the behavior observed by Heiz and co-workers on MgO, reflecting the much stronger Ni-support binding for TiO_2 .

There are a number of motivations for studying the Ni– TiO_2 system. Nickel particles supported on TiO_2 are used in heterogeneous catalysis. In addition, the rutile $\text{TiO}_2(110)$ surface has been studied extensively, and there are a number of studies addressing the morphology and electronic properties of Ni evaporated onto $\text{TiO}_2(110)$, useful in interpreting our results. The structure of the surface is shown in Fig. 1, along with several possible binding motifs for Ni_2 and Ni_5 . The surface unit cell is indicated by the white rectangle, and the density of unit cells is $\sim 7 \times 10^{14}/\text{cm}^2$. Also indicated with circled letters A–D, are the Ni binding sites identified by Pala, Liu, and Truong⁶ in recent density functional calculations. The binding energies are 2.6, 2.0, 1.8, and 0.6 eV, for A–D, respectively. In these periodic calculations, there is one Ni atom per surface unit cell, and it is unclear how the binding energies might change with coverage. Nonetheless, their results indicate that Ni– TiO_2 binding is both relatively strong, and quite corrugated (i.e., site-dependent).

A number of groups have also reported experimental

^{a)}Electronic mail: anderson@chem.utah.edu

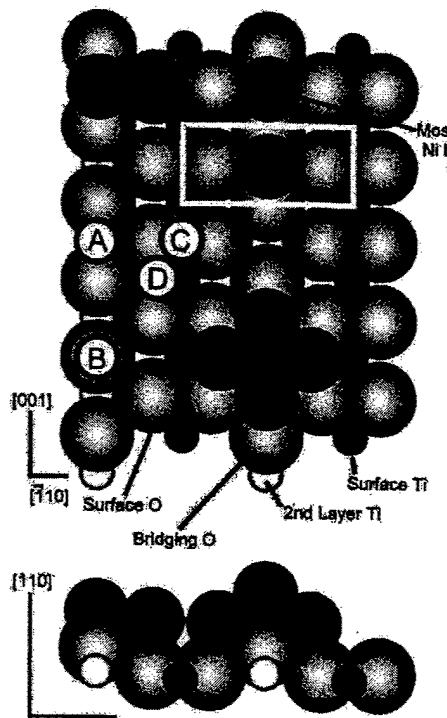


FIG. 1. The structure of the rutile $\text{TiO}_2(110)$ surface, showing surface and second layer Ti, surface and bridging O. The surface unit cell is indicated as a white rectangle. A–D indicate the Ni binding sites calculated by Pala *et al.* (Ref. 6) in order of decreasing stability. The dark spheres indicate the potential Ni dimer and Ni_5 binding arrangements.

studies of Ni evaporated onto $\text{TiO}_2(110)$. Onishi *et al.*,⁷ on the basis of the Ni dose-dependence of Auger intensities, concluded that Ni grows as a surface layer for densities up to $\sim 8 \times 10^{14}/\text{cm}^2$ (i.e., \sim one Ni/unit cell), then begins to form three-dimensional structures. Other authors conclude that growth is three-dimensional (Volmer–Weber) even at low coverages.^{8,9} In STM, cluster morphology is clearly seen at low coverages ($\sim 2 \times 10^{14} \text{ Ni/cm}^2$) following deposition at 375 K.⁸ The origin of the discrepancy is unclear, but may be related to dose rate or surface conditions. One problem in comparing with these earlier studies is that they all use different methods for TiO_2 preparation, and it is not clear that the support is identical.

The metal-support electronic interactions of nickel particles formed during Ni evaporation onto $\text{TiO}_2(110)$ have been studied by electron spectroscopy.^{7,9–11} On stoichiometric $\text{TiO}_2(110)-(1 \times 1)$, only the zero oxidation state Ni is observed, however, the Ni $2p$ binding energy is observed to increase with decreasing nickel coverage. This shift has been explained in terms of final state relaxation effects, and Kao *et al.*¹⁰ also proposed that there is partial electron transfer ($\sim 0.13 e^-/\text{Ni}$) from TiO_2 to Ni. This last point is contradicted by the work function measurements of Onishi *et al.*,⁷ which were interpreted to indicate a $\sim 0.1 e^-/\text{Ni}$ electron transfer *from* Ni *to* TiO_2 . CO desorption temperatures have also been reported by Raupp and Dumesic¹² for nanometer size nickel particles formed by Ni evaporation onto $\text{TiO}_2(110)$. It was found that the desorption peak shifts to decreasing temperatures with decreasing Ni evaporative dose, and with increasing density of missing-oxygen defects

on the TiO_2 . Finally, on the basis of decreasing Ni XPS signal following extended annealing, Kao *et al.*¹⁰ inferred that Ni diffuses into the TiO_2 bulk at elevated temperatures. This conclusion is contradicted by the more recent XPS and ISS work of Espinós *et al.*¹¹ who observed no Ni signal loss for stoichiometric TiO_2 , but did observe diffusion into the bulk for defective TiO_x prepared by Ar^+ sputtering.

II. EXPERIMENT

The instrument consists of a cluster source, a mass-selecting beamline, and a set of UHV chambers where deposition, sample preparation, and analysis are carried out. The beamline and sample handling arrangement have been described in previously.^{13,14} Nickel cluster ions are generated by a 100 Hz laser vaporization source, similar to the source recently reported by Heiz and co-workers.¹⁵ A 100 Hz Nd:YAG laser (Spectra Physics) is tightly focused on a rectangular nickel target that is continuously rastered under computer control. The vaporized metal plasma is entrained in a pulsed helium flow and swept down a 1.5 mm diameter channel, where cluster ions grow. At the end of the channel, the gas pulse exits through a nozzle, and cluster ions are injected into a 27 cm long quadrupole ion guide. At the end of this first guide, the cluster ion beam is deflected by 18° and injected into a second quadrupole which guides the ions through several more differential pumping walls, and delivers them to a commercial quadrupole mass filter (Exret). After mass selection, the clusters are guided by a final quadrupole into the UHV section of the instrument, where they are deposited on the room temperature substrate through a 2 mm diam mask/lens.

The cluster dose is measured by continuously monitoring current on the target, and unless indicated otherwise, the coverage was always 2.0×10^{14} Ni atoms per cm^2 , equivalent to a tenth of a close-packed Ni monolayer. The impact energy was varied by floating the beamline potentials with respect to the grounded TiO_2 target. Typical intensities of mass-selected cluster ions, delivered to the deposition substrate, range from 1 to 25 nA/cm^2 . Deposition times are typically 30–60 min. The deposition energy distribution is estimated by retarding potential analysis on the deposition target, i.e., measurement of the drop in deposition current as the target potential is raised. Because the target current is effected by beam divergence and space charge, as well as the energy spread, the energy width extracted from retarding analysis is approximate, and should be an upper limit. The full width at half maximum of the energy width is $<1 \text{ eV}$, for all cluster sizes. The base pressure in the UHV system is $\sim 1 \times 10^{-10} \text{ Torr}$. The pressure in the deposition chamber rises to $\sim 2 \times 10^{-9} \text{ Torr}$ during deposition, however, the additional gas is ultrahigh purity helium from the laser vaporization source. Contamination of the surface is routinely monitored before and after experimental runs. For this system, there is no evidence for reaction with background gases on the experimental time scale.

The UHV system is equipped with a hemispherical energy analyzer, a dual anode x-ray source (here, using $\text{Al K}\alpha$ radiation) and an ion gun, allowing sample characterization

by x-ray photoelectron spectroscopy (XPS) and low energy ion scattering spectroscopy (ISS). The sample can be transferred into a separate UHV chamber for temperature-programmed desorption (TPD) studies. For TPD, the sample was heated at 3 K/s by electron bombardment from the back-side. Desorbing molecules enter the differentially pumped quadrupole mass spectrometer through a 2 mm diameter aperture in the end of a conical skimmer. The aperture matches our deposition spot size, and is positioned ~ 1 mm from the TiO_2 substrate, minimizing desorption background from other surfaces. Samples are cleaned by Ar^+ sputtering, then annealed in one of two stations. One is used for annealing in UHV, and the other, located in a separate chamber, allows annealing at high O_2 pressures.

XPS spectra were used to estimate TiO_2 stoichiometries for the near-surface region. The spectra were corrected using Shirley background subtraction,¹⁶ before the XPS peak areas were integrated. Atomic sensitivity factors for our instrumental configuration were taken from the PHI Handbook.¹⁷ We note that the binding energies of $\text{Ti} 2p$ and $\text{O} 1s$ differ by only 70 eV, so that the corresponding electron kinetic energies differ by only $\sim 7\%$. As a consequence, the usual uncertainties arising from energy-dependence electron detection efficiency should be minimal. The stoichiometries derived from XPS reflect average properties of a near-surface region defined by the inelastic mean free path (λ) for electrons in TiO_2 . For $\text{O} 1s$ and $\text{Ti} 2p$ photoelectrons λ is ~ 21 Å, while for $\text{Ni} 2p$ photoelectrons λ is ~ 14 Å.¹⁸

$\text{TiO}_2(110)$ single crystals (Commercial Crystal Laboratories) are mounted on a homebuilt sample holder¹⁴ that allows samples to be moved between different preparation or analysis stations with precise positioning. The crystal is clamped against a thick molybdenum backing plate that can be cooled by conduction to a liquid N_2 reservoir. For TPD or annealing in vacuum, the metal backing plate is heated by electron bombardment from the back side. For lower temperature annealing in O_2 atmospheres, the entire sample holder is heated by conduction from a resistively heated copper stage. The crystal temperature is measured by a thermocouple bonded inside a slot cut into the edge of the TiO_2 crystal, using UHV-compatible cement. In order to make the crystal conductive enough to allow ion deposition and minimize charging in XPS, the crystal was initially annealed in UHV at 1000 K for 1 h. This process creates defects throughout the bulk, and results in *n*-type semiconducting properties reflected in a permanent color change from the initially transparent crystal. The main surface contaminant is Na, which is present at ppm concentrations in the TiO_2 bulk, and also a component of the ceramic cement (AREMCO 571) used to bond the thermocouple. Freshly mounted crystals are subjected to repeated sputter/anneal cycles until negligible contaminant signal is observed by ISS and XPS, ISS being extremely sensitive to surface Na. Following each cluster deposition experiment, the crystal was sputtered with 1 kV Ar^+ ions well past the point where no Ni XPS or ISS signal was observed, and the regular sputtering also prevented re-appearance of alkali contamination. The sample was then annealed under different conditions to generate titania with desired surface properties.

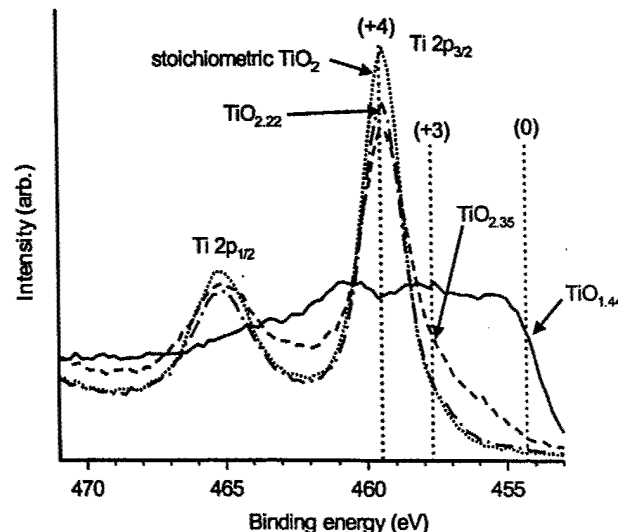


FIG. 2. The $\text{Ti} 2p$ XPS of clean TiO_2 under different preparation conditions. " $\text{TiO}_{1.44}$ " is the surface following Ar^+ ion sputtering only. " TiO_2 " is sputtered then annealed in UHV at 900 K. " $\text{TiO}_{2.35}$ " is sputtered then annealed in O_2 at 570 K. " $\text{TiO}_{2.22}$ " is sputtered then annealed in O_2 at 700 K. The vertical dashed lines indicate the expected binding energies for Ti in different oxidation states.

III. RESULTS AND DISCUSSION

Ni_2^+ , Ni_5^+ , and Ni_{10}^+ were deposited at impact energies of 1 eV/atom and 10 eV/atom, always with the dose equivalent to 0.1 ML of atoms (2.0×10^{14} atoms/cm²). Several experiments were also run with Ni^+ and Ni_{15}^+ at 1 eV/atom. The XPS of the as-deposited sample was used to characterize the distribution of oxidation states of Ni and Ti, and ISS was used to characterize the morphology of the sample. After characterization, TPD of C^{18}O was studied. To exclude the possibility that ISS might damage/modify the sample, some TPD runs were done without prior ISS. Finally, after TPD analysis, the sample was recharacterized to examine changes in sample stoichiometry, oxidation state, and morphology, induced by the TPD process.

A. X-ray photoelectron spectroscopy

Figure 2 shows the $\text{Ti} 2p$ XPS following different annealing procedures. The expected positions¹⁷ of the $2p_{3/2}$ peaks from different oxidation states of Ti are indicated with vertical dashed lines and the labels 0, +3, and +4. To correct for sample charging, which depends somewhat on preparation conditions, all spectra have been referenced to the $\text{O} 1s$ peak, assumed to be at 530.8 eV as in stoichiometric TiO_2 .¹⁷ As a check on this correction, note that the resulting Ti +4 binding energy is in excellent agreement with the expected value of 459.5 eV. The spectrum labeled $\text{TiO}_{1.44}$ is for the freshly sputtered surface, without annealing. The XPS spectrum shows a broad range of Ti oxidation states ranging from 0 to +4, consistent with preferential sputtering of surface oxygen. The $\text{O} 1s$ XPS peak for this sample is broadened by almost 1 eV compared to the $\text{O} 1s$ XPS for annealed TiO_2 . The broadening suggests that a range of oxygen environments is present in the near-surface region, and also makes the charging correction less precise. The stoichiometry cal-

culated from XPS of the reduced surface is $\text{TiO}_{1.44}$, which is an average over electron escape depth.

When the reduced TiO_2 is annealed in UHV at 900 K for a 1 h, the surface appears to be fully oxidized (spectrum labeled "stoichiometric TiO_2 "). Both the ratio of Ti and O peak intensities, and the absence of signal for Ti (+3) are consistent with TiO_2 stoichiometry. The oxidation may occur by diffusion of bulk oxygen to the surface as proposed by Lusvardi *et al.*¹⁹ and/or by diffusion of titanium cations from the surface to the bulk as suggested by Henderson.²⁰ Henderson²⁰ and Linsebigler *et al.*²¹ found that annealing at 900 K creates 5%–10% of oxygen vacancies on the surface, however, their annealing times are much shorter than ours. For short annealing times we also observe significant intensity for Ti (+3), consistent with numerous oxygen vacancies. Nonetheless, our XPS resolution is not high enough to exclude a small Ti (+3) peak buried in the tail of the Ti (+4) peak, and the TPD results indicate that there are, indeed, significant numbers of surface defects.

When the sputtered TiO_2 is annealed for 1 h at 570 K in 10^{-5} Torr of oxygen, the $\text{Ti} 2p$ XPS (labeled $\text{TiO}_{2.35}$) shows a shoulder extending over the Ti (+3) binding energy, indicating that under these conditions, the reduced Ti is not completely oxidized. The stoichiometry calculated from XPS was $\text{TiO}_{2.35}$, however, indicating that the surface has extra oxygen compared to the UHV-annealed sample. Diebold and co-workers suggested that annealing reduced TiO_2 below 600 K with oxygen exposure of 300 L, oxidizes oxygen vacancy sites but leaves oxygen adatoms bound to the surface.²² A subsequent imaging study from that group showed that atomically flat vacuum-annealed TiO_2 underwent restructuring upon O_2 exposure at elevated temperatures, creating roughened surfaces.²³ Our results, below, show that the O_2 -annealed surface is highly oxidizing, consistent with the presence of chemisorbed oxygen. A few experiments were also performed on a surface with XPS-measured stoichiometry of $\text{TiO}_{2.22}$, prepared by annealing sputtered TiO_2 in O_2 at 700 K. As discussed below, this surface also shows the higher oxidative reactivity attributed to chemisorbed oxygen. Both the lower O:Ti ratio, and reduced reactivity compared to the $\text{TiO}_{2.35}$ surface, are consistent with a lower concentration of chemisorbed oxygen.

Figure 3(a) shows the $\text{Ni} 2p$ XPS following deposition of Ni_2 , Ni_5 , and Ni_{10} on stoichiometric TiO_2 at different *per atom* impact energies. At 1 eV/atom impact energy, Ni is observed only in its zero oxidation state, indicating that there is no redox chemistry between the deposited nickel and the stoichiometric TiO_2 surface. No oxidation is observed for Ni or Ni_{15} deposition at 1 eV/atom either (not shown). Note that for higher impact energies, we begin to see a peak at higher binding energy (856.0 eV), corresponding to formation of Ni in the +3 oxidation state.¹⁷ For Ni_2 , the nickel oxidation is quite clear for an energy of 10 eV/atom. For Ni_5 , a +3 oxidation state peak only becomes obvious at 20 eV/atom, although there is some sign of a shoulder at 10 eV/atom. For Ni_{10} , there is no sign of oxidation at our highest deposition energy. The data indicate that nickel clusters are chemically stable on the stoichiometric TiO_2 surface, but that redox chemistry can be driven with sufficient impact energy.

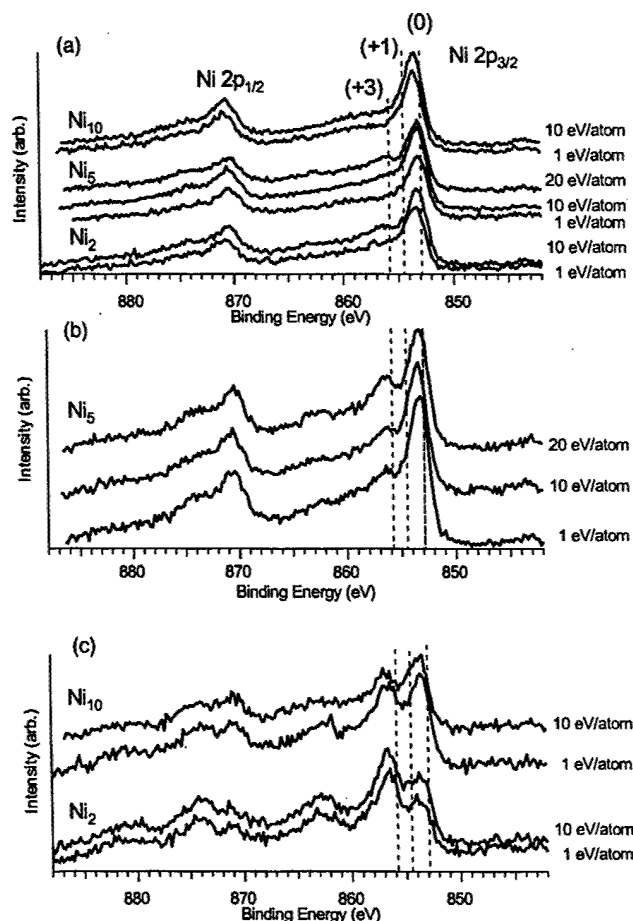


FIG. 3. The $\text{Ni} 2p$ XPS of the nickel clusters on (a) vacuum annealed TiO_2 ; (b) $\text{TiO}_{2.22}$; and (c) $\text{TiO}_{2.35}$. The numbers to the right of the spectra are the cluster impact energies (eV/atom).

Note that the Ni zero oxidation state XPS peak is shifted towards higher binding energy by ~ 0.4 eV, relative to the dashed line indicating the peak position in metallic Ni. This shift is consistent with studies of Ni binding energy shifts for evaporated Ni/ TiO_2 films, discussed above.^{7,9,10} We also find that the $\text{Ti} 2p$ XPS broadens slightly to lower binding energy, upon Ni dosing.

Figure 3(b) shows the nickel $2p$ XPS after depositing Ni_5 on $\text{TiO}_{2.22}$. Even at the lowest impact energy, a significant Ni +3 oxidation state peak is observed, indicating that this surface is more oxidizing than the stoichiometric TiO_2 . The comparison clearly shows that Ni oxidation at low impact energy results from nickel interactions with oxygen chemisorbed at defects, rather than with the titania, itself. The observation that only a small fraction of the Ni atoms in Ni_5 are oxidized, suggests that the Ni atoms deposited as clusters are not highly mobile on the surface at room temperature. Otherwise they would be able to scavenge additional chemisorbed oxygen. The ISS results discussed below are consistent with this conclusion. Note that the extent of oxidation increases substantially with impact energy. Because oxidation is also observed on the stoichiometric surface at high impact energies, we attribute the increased oxidation to reaction with titania, rather than an increase in Ni mobility.

Figure 3(c) shows the results of Ni cluster deposition on the $\text{TiO}_{2.35}$ surface, where we believe that there is substantially more chemisorbed oxygen. Consistent with this belief, we observe that a substantially greater fraction of deposited Ni is oxidized. There is a significant cluster size effect in the degree of oxidation. For Ni_2 , even at the lowest deposition energy, roughly 80% of nickel atoms are oxidized, suggesting that there is sufficient chemisorbed oxygen near most impact sites to oxidize the cluster, or possibly that the dimers are sufficiently mobile to scavenge nearby chemisorbed oxygen. For Ni_{10} , approximately 60% of nickel atoms remain in the zero oxidation state, presumably because there is simply not enough active oxygen to fully oxidize the larger cluster. Because the total Ni atom dose is identical in all experiments, the different behavior of Ni_2 and Ni_{10} is another sign that the Ni atoms are not highly mobile at room temperature, at least when deposited as clusters. If diffusion were facile regardless of the form in which the Ni is deposited, we would expect the final state of the system to be cluster size independent. Note that the time scale of the experiments is on the order of one hour (including both deposition and XPS analysis time) while the areal density of chemisorbed oxygen must be quite high to give the $\text{TiO}_{2.35}$ apparent stoichiometry. Evidently the diffusion rate is near zero for Ni deposited as clusters with size on the order of ten atoms.

When Ni clusters are deposited on freshly sputtered TiO_2 , without annealing, only zero oxidation state nickel is observed at all impact energies, presumably because the surface is quite oxygen deficient and Ti has a higher oxygen affinity than Ni. In addition, there is no shift in the zero oxidation state peak.

B. Low energy ion scattering spectroscopy

Further insight into the structure of the sample surfaces, and the effects on the samples of CO adsorption and of heating, can be obtained from low energy ion scattering spectroscopy (ISS). Here, a ${}^4\text{He}^+$ beam with 1 keV incident energy (E_0) impinges on the surface at 45° incident angle, and the kinetic energy (E) of scattered ions is detected along the surface normal, after scattering by 135° . The dominant scattering process observed in ISS can be regarded as binary elastic collisions between incident He^+ and single atoms on the surface. In that case, the position of peaks, E/E_0 , is simply related to the masses of surface atoms from which the He^+ scatters.²⁴

While ISS peak positions provide unambiguous identification of surface atoms, via their mass, the peak intensities depend on three factors: the cross section for scattering from a particular type of atom, the He^+ ion survival probability (ISP), and the extent to which different surface atoms are shadowed or blocked by other surface atoms. For 1 keV He^+ , the scattering is from the core electrons of the target atoms, and the effective atomic sizes are much smaller than the interatomic spacings. The probability for scattering into our detector is proportional to the square of the impact parameter (b^*) that leads to 135° scattering. These b^* values were estimated by running classical trajectories for an empirically corrected Molière potential.²⁴ The cross sections (σ) are in the ratio, 0.23:1:1.4 for $\sigma_{\text{O}}:\sigma_{\text{Ti}}:\sigma_{\text{Ni}}$.

A major factor in ISS is that most He^+ is neutralized during the scattering process. The ion survival probability (ISP) depends on the electron densities traversed during each scattering trajectory, and varies with the chemical element, oxidation state, and local environment of the target atom. As a consequence, peak intensities in ISS are not simply related to surface concentrations. One simplification resulting from neutralization is that only atoms in the topmost layer contribute significantly to the scattered ion intensity. If Ni is deposited on top of the surface, the Ti or O atoms to which it is bonded are effectively second layer atoms, and the scattering signal from these atoms is expected to be significantly attenuated.

The final effects are blocking and shadowing. Blocking is when He^+ scattered from one atom cannot reach the detector because a second atom is in the way. Because we detect along the surface normal, blocking effects only atoms directly underneath the surface atom, and these second layer atoms already have negligible detection probability. Shadowing refers to the fact that atoms on the surface cast a roughly conical scattering shadow, i.e., scattering from a surface atom prevents He^+ from reaching other atoms that are directly behind it. For 1 keV He^+ scattering from Ni, for example, the shadow cone radius is estimated to be²⁵ $\sim 0.9 \text{ \AA}$ at a distance of 2 \AA . The shadowing effect depends on the angle of incidence, the Ni binding geometry, and the azimuthal angle of the surface with respect to the ion beam. We cannot vary azimuthal angle in our experiment, but measure identical ISS spectra for different samples mounted with random azimuthal angles, verifying that we have not accidentally chosen an azimuthal angle where shadow cone edge effects²⁴ are significant. It is straightforward to estimate the average shadowing per Ni atom on the surface, by simply counting surface atoms within the shadow cone, averaging over azimuthal angle. For our rather steep angle of incidence, it turns out that the shadowing effect is small. For dispersed atoms in the A–D binding sites and for the dimer and pentamer structures in Fig. 1, the shadowing ranges from ~ 0.4 to $\sim 0.7 \text{ Ti}$ or O atoms shadowed per Ni. Most of these atoms are bound to the Ni, and therefore are expected to have reduced ISP, anyway.

Because of ISP and shadowing effects, the relative intensities of Ni, Ti, and O peaks depend strongly on how the Ni is disposed on the surface. For example, Ni in sites A or B (Fig. 1) would attenuate only O intensity, while Ni in site C or D would effect both O and Ti intensities. In general, the greatest attenuation of Ti and O intensities should occur for Ni dispersed as atoms on top of the surface, because each Ni attenuates He^+ scattering signal from a number of surrounding substrate atoms. With increasing cluster size, we expect that a given dose of Ni will result in less attenuation of O or Ti signal, because a smaller fraction of the substrate surface is covered.

The Ni ISS signal is also important, providing insight into the cluster morphology. As long as all Ni remains in the top layer, the Ni signal should be roughly independent of cluster size. If the Ni forms multilayer particles, however, only the top layer Ni contributes to the Ni ISS, and more TiO_2 surface is exposed. The result would be a substantial

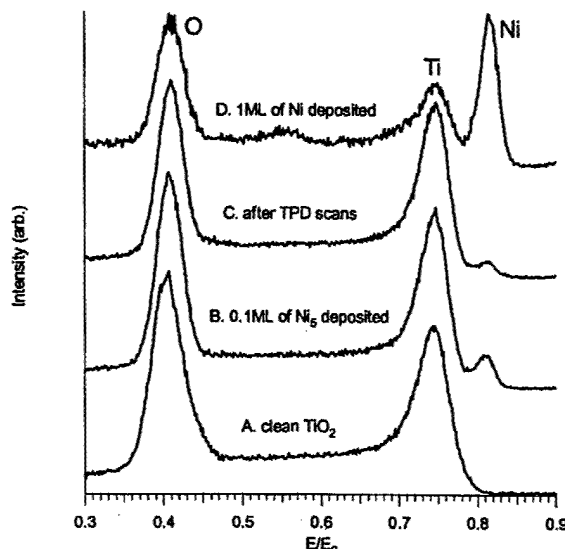


FIG. 4. Typical low energy ion scattering spectra. (A) clean TiO_2 ; (B) TiO_2 with $2.0 \times 10^{14} \text{ Ni atoms/cm}^2$ (0.1 ML) deposited as Ni_5 at 1 eV/atom; (C) same as (B), after TPD experiments; (D) TiO_2 with $2.0 \times 10^{15} \text{ per cm}^2$ of Ni^+ deposited at 1 eV (1 ML).

decrease in Ni/Ti and Ni/O ratios. Another possibility is strong metal-support interaction (SMSI), i.e., encapsulation of Ni particles by TiO_2 . Recent work of Diebold and co-workers²⁶ provides a textbook example of SMSI, wherein Pt clusters annealed on TiO_2 are completely encapsulated in a reduced TiO_x layer, resulting in complete loss of Pt ISS signal. Encapsulation has been observed for Ni/TiO_2 , but only following high temperature annealing in a H_2 atmosphere.^{12,27} A related possibility is that the Ni might diffuse into the TiO_2 lattice, forming a mixed oxide phase, in which case, the Ni signal would be strongly attenuated. Finally, at our highest deposition energies, it is not impossible that some Ni implantation into the TiO_2 surface might occur. Such implantation would result in strong attenuation of Ni ISS signal.

Figure 4 shows a number of ISS spectra, and Table I gives ratios of peak intensities. Trends with cluster size are summarized in Fig. 5. Ratios are reported, rather than raw intensities, because the data were taken over a several month period, and it is impossible to keep the He^+ beam parameters exactly constant from run to run. Also included in the table for comparison, are data for deposition of 0.1 ML and 1.0 ML of Ni^+ at 1 eV.

Before considering the ISS data for the clusters, is it useful to consider two limiting cases. Figure 4(A) shows an ISS spectrum of clean TiO_2 , prior to Ni deposition. The O/Ti intensity ratio is 1.27, consistent with the results of Diebold and co-workers.²⁶ The ratio expected in absence of ISP effects is only 0.69, estimated as the product of $\sigma_{\text{O}}/\sigma_{\text{Ti}}$ ($=0.23$) and the relative number of first layer O and Ti atoms (3:1). The fact that the measured O/Ti ratio is substantially larger indicates that the ISP is lower for scattering from Ti than for scattering from O, probably reflecting the more exposed geometry of O on this surface (Fig. 1).

The other interesting point of comparison is the experiment where 1.0 ML of Ni^+ was deposited at 1 eV [Fig.

TABLE I. ISS intensity ratios, and integrated intensities.

Sample	Cluster	Energy	O/Ti ratio	Ni/substrate ratio ^a
Clean TiO_2			1.27	
0.1 ML, before TPD	Ni	1 eV	0.98	0.07
	Ni_2	1 eV	0.98	0.08
		10 eV	0.90	0.06
	Ni_5	1 eV	1.12	0.07
		10 eV	1.10	0.08
	Ni_{10}	1 eV	1.24	0.08
		10 eV	1.29	0.12
	Ni_{15}	1 eV	1.36	0.01 ₄
1 ML, before TPD	Ni	1 eV	1.75	1.07
0.1 ML, after TPD	Ni	1 eV	1.0	0.03
	Ni_2	1 eV	0.90	0.02
		10 eV	0.94	0.02
	Ni_5	1 eV	0.98	0.02
		10 eV	not taken	
	Ni_{10}	1 eV	1.13	0.04
		10 eV	0.81	0.04
	Ni_{15}	1 eV	1.34	0.01 ₂
1 ML, after TPD	Ni	1 eV	1.73	0.76

^aAverage of Ni/O and Ni/Ti ratios. Where given, the subscripted final digits are given only to show the trend.

4(D)]. Under this condition, the Ni, O, and Ti peaks are all comparable in size, and the O/Ti ratio is 1.75. As noted in the Introduction, there is some debate in the literature about the growth mechanism for Ni evaporated onto $\text{TiO}_2(110)$, with some data suggesting that growth is initially layer-by-layer, and other data indicating three-dimensional growth from the

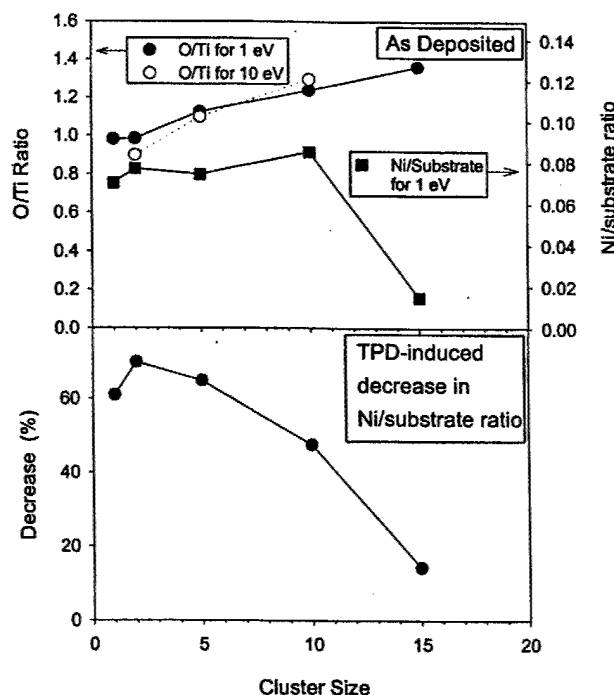


FIG. 5. Top frame: O/Ti ISS ratios (left-hand scale) and Ni/substrate ISS ratios (right-hand scale) for as-deposited Ni and Ni clusters on TiO_2 at a constant dose of 0.1 ML of Ni atoms. Bottom frame: Percent decrease in Ni/substrate ISS ratio induced by TPD, as a function of cluster size.

start. The ISS results indicate that for our conditions, the growth mechanism is 3D to some extent. This conclusion rests on the observation of Ti and O ISS intensities $\sim 64\%$ and 50% of those for clean TiO_2 . If growth were entirely two-dimensional, our $2.0 \times 10^{15} \text{ Ni/cm}^2$ dose would completely block the O and Ti ISS. On the other hand, it appears that the degree of Ni agglomeration is not high, as shown by both the strong Ni ISS signal and the observation of substantial attenuation of substrate ISS signal. If large multilayer particles were forming, for example, then we would expect less attenuation of the Ti and O signals, and the Ni signal would be weak, because only the top layer Ni atoms would be observable. Limited agglomeration is not surprising given the strong and highly corrugated Ni– TiO_2 binding calculated by Pala *et al.*⁶

When 0.1 ML equivalents of Ni, Ni_2 , Ni_5 [Fig. 4(B)], Ni_{10} , and Ni_{15} are deposited at 1 eV/atom, the O/Ti ratios are 0.98, 0.98, 1.12, 1.24, and 1.36, respectively (Fig. 5, top frame). The large drop in O/Ti ratio for Ni and Ni_2 , relative to clean TiO_2 , indicates that Ni attenuates scattering signal from O more than Ti, suggesting that binding is preferentially to oxygen sites. This result is consistent with the calculations of Pala *et al.*⁶ indicating that oxygen binding is energetically preferred for Ni atoms. The fact that the ratio is identical for Ni and Ni_2 is not surprising. Regardless of how they land, Ni atoms should be able to settle into the more stable oxygen binding sites (A or B, Fig. 1). Ni_2 can presumably bind with each atom in an adjacent A site, or at least with both atoms in adjacent oxygen sites (Fig. 1). In either case, the ISP and shadowing/blocking effects attenuate scattering from O, but not Ti. The observation that the O/Ti ratio increases with deposited cluster size, is also not unexpected. Larger clusters cover less of the surface, leading to more contribution from bare TiO_2 regions, and because large clusters have large footprints, they necessarily attenuate scattering from both Ti and O. It may seem surprising that the ratio can exceed that for clean TiO_2 , however, we note that the ratio is 1.75 for the 1.0 ML Ni sample. Without knowing the details of how clusters bind to the surface, and how cluster binding might modify the ISP for scattering from neighboring atoms, it is not possible to interpret the O/Ti ratios quantitatively. Nonetheless, the trends suggest that the average size of Ni clusters on the surface is correlated with the size of the deposited clusters. The O/Ti ratios clearly rule out substantial fragmentation or agglomeration of the clusters, because in that case, the ratio should be roughly size-independent. Furthermore, we can rule out certain binding arrangements. For example, if deposited clusters rearranged from the compact geometry of gas-phase Ni clusters,^{28,29} to a linear cluster bound along a row of oxygen atoms (e.g., bound to neighboring "A" sites), then the O/Ti ratio would remain near that for isolated atoms, independent of cluster size.

The Ni/substrate ISS ratios (i.e., Ni/Ti and Ni/O) provide additional morphological insight, summarized in Table I and the top frame of Fig. 5. As comparison of curves B and C of Fig. 4 indicates, the dominant factor effecting the Ni/substrate ratios is changes in the Ni ISS intensity, although the individual Ni/Ti and Ni/O ratios obviously also reflect the

changes in the O/Ti ratio discussed above. To isolate the trends in the Ni ISS signal from the changes in O/Ti ratios, Table I and Fig. 5 give Ni/substrate ratios, taken as the average of the Ni/O and Ni/Ti ratios. The Ni/substrate ratios depend on the fraction of deposited Ni atoms exposed on the surface, along with the ISP for scattering from those atoms. As already noted, sintering into multilayer particles or penetration of Ni into the surface would result in substantial decrease in the Ni signal. For Ni, Ni₂, Ni₅, and Ni₁₀, the nearly constant Ni/substrate ratios suggests that most or all Ni remains in the top layer. For Ni₁₅, however, the Ni intensity is substantially lower, consistent with this large cluster retaining a three-dimensional structure on the surface, where scattering from most of the Ni atoms is attenuated by the presence of a few top layer Ni atoms.

When the deposition energy is increased to 10 eV/atom, the O/Ti ratios remain approximately constant, suggesting that the Ni dispersion on the surface is not grossly altered at high impact energies. If clusters were shattering in high energy deposition, for example, the O/Ti ratios would drop to near the small cluster limit (<1). There are signs in the Ni/substrate ratios, however, that the cluster structures are affected by increased deposition energy. For Ni_2 , the Ni/O and Ni/Ti ratios decrease by $\sim 25\%$, suggesting that some Ni is being driven into the TiO_2 substrate. We would expect these implanted Ni atoms to be oxidized, and indeed, our XPS results [Fig. 3(a)] show significant oxidation for Ni_2 at 10 eV/atom. The alternative explanation, that Ni sticking probability is reduced at high impact energies, is ruled out by the observation that the total Ni XPS intensity does not decrease for deposition at high energies.

For Ni_5 and Ni_{10} no oxidation is observed in the XPS at 10 eV/atom, consistent with the observation of no decrease in Ni/O or Ni/Ti ratios. For Ni_{10} , in fact, there is a small *increase* in Ni ISS signal, reflected in both the raw intensities and the ratios. A not unreasonable explanation for this effect is that at low impact energies, the deposited Ni_{10} retains, to a small degree, the 3D structure of the free cluster. At 10 eV/atom, more flattening of the cluster is expected, exposing more Ni to the ion beam.

In summary, the ISS results for the as-deposited clusters are consistent with the clusters remaining approximately intact on the surface, particularly at low deposition energies. The larger clusters probably even retain some 3D structure. We certainly are not suggesting that the cluster structures are unperturbed by the impact process or by binding to the surface. Indeed, the strong (and highly corrugated) binding calculated by Pala *et al.*⁶ for Ni atoms on TiO₂ suggests that cluster structure is undoubtedly effected even for low impact energies, but at the same time, the tendency to diffusion is reduced.

ISS was measured for each sample following the sequence of TPD experiments described below, and the results are given in the bottom half of the table and summarized in the bottom frame of Fig. 5. Particularly for the smaller clusters, the ISS results show that there are large changes in the morphology of the deposited nickel, induced by the CO adsorption, heating, and desorption that occurs in TPD. The Ni signal drops significantly after TPD, as shown for Ni_5 by

comparison of traces B and C in Fig. 4. The decreases in Ni/substrate ratio for Ni, Ni₂, Ni₅, Ni₁₀, and Ni₁₅, are 61%, 70%, 65%, 47%, and 12%, respectively (Fig. 5). For the 1 ML Ni deposit, a decrease of 29% is observed. The effect is similar for deposition at 1 eV/atom and 10 eV/atom, again suggesting that cluster properties are not grossly perturbed by deposition energy in this range. In XPS, we observe little TPD-induced change in the Ni 2p intensity, and no Ni-containing species are observed to desorb during TPD. These observations indicate that Ni remains in the near-surface layers after TPD. The XPS data indicate a small increase in the fraction of Ni in the +3 oxidation state, but >90% remains in the zero oxidation state.

The decreases in the Ni ISS signal must, therefore, be interpreted in terms of changes in Ni morphology during TPD. There are two limiting case mechanisms. Ni might be sintering into multilayer particles, in which a significant fraction of the Ni atoms are no longer in the ISS-accessible top-layer. Alternatively, it might be that SMSI results in partial encapsulation of the Ni clusters in TiO₂. (We can rule out complete encapsulation because the substantial Ni ISS signal is still observed.) In principle, it should be possible to distinguish sintering from partial encapsulation by the differing extents of XPS signal reduction that would result. To test this idea, we did simple continuum electron attenuation calculations³⁰ for two model morphologies, using inelastic mean free path values for Ni and TiO₂ from the NIST database.¹⁸ The XPS signal reduction calculated for a two layer Ni deposit (which would give ISS attenuation of 50%), is ~8% relative to Ni in a single layer. This reduction is essentially identical to the ~7% reduction calculated for a model single layer Ni deposit with 50% coverage of a single layer of TiO₂.

Both sintering and partial encapsulation mechanisms are consistent, within the experimental uncertainty, with the ~6% percent decrease observed in the XPS following TPD. Several considerations favor the sintering mechanism, however. Sintering would explain why the reduction in Ni ISS signal is inversely dependent on cluster size. Large clusters tend to be more stable with respect to surface diffusion than small clusters, and thus are expected to sinter less. The small reduction observed for Ni₁₅ is also consistent with a sintering mechanism; because the ISS data suggest that as-deposited Ni₁₅ is already three-dimensional. Sintering has been observed for Ni/TiO₂ at elevated temperatures by STM.⁸ Finally, it seems likely that encapsulation of our small nascent clusters would lead to a significant degree of Ni oxidation, not observed in the post-TPD XPS. It must be noted, however, that we cannot rule out the partial encapsulation mechanism, which could account for the observations if it is assumed that the tendency toward encapsulation is inversely dependent on cluster size, and if encapsulation is not accompanied by oxidation, even of atoms and dimers.

We did one experiment bearing on the sintering/encapsulation question. For a freshly-deposited Ni_n/TiO₂ sample, the Ni ISS signal is observed to decrease monotonically with time under the He⁺ beam, because the Ni is slowly sputtered away. After a TPD experimental cycle, the Ni signal is still observed to decrease monotonically with

time. If the TPD-induced decrease in the Ni ISS signal were attributable to partial encapsulation by TiO_x, we might expect that the Ni ISS signal would initially increase with time, because sputtering of the TiO_x overlayer would tend to expose additional Ni.

The one observation that is hard to reconcile with a pure sintering model, is that the O/Ti ratios do not increase significantly following a TPD cycle, as might be expected from the trend in O/Ti ratio with increasing size of deposited cluster. We looked for loss of oxygen from the surface as both O₂ and CO₂, but none is observed in the temperature range of the TPD experiments. One possibility is that the mechanism includes both sintering and SMSI, i.e., Ni may be sintering into larger particles, but there may also be some SMSI at the interface between the Ni particle edges and the support. By bringing some partially reduced TiO_x to the surface, SMSI would reduce the O/Ti ratio.

C. Temperature-programmed desorption

TPD experiments were performed for Ni clusters deposited on stoichiometric TiO₂(110). The sample was cooled by conduction to a liquid N₂ reservoir to an initial temperature of ~140 K. The sample was then dosed with a saturation dose of C¹⁸O (>20 L). Prior to each TPD heating run, the filament used for electron-bombardment heating was flash-heated for 0.5 s with the electron bias voltage set to 300 V. This desorbs CO from the area around the heater, and also removes CO from surfaces where electron-stimulated desorption might cause elevated background during the TPD run. All TPD were done at a constant 3 K/s heating rate, followed by rapid cooling. The quadrupole mass spectrometer was rapidly switched between masses of interest during the heating phase of the experiment. In each run we monitor C¹⁸O⁺, Ni⁺, C¹⁶O¹⁸O⁺, and C¹⁸O₂⁺. Ni⁺ is monitored because this is the major nickel-containing ion observed in electron bombardment ionization of nickel carbonyl.³¹

Figure 6 shows C¹⁸O TPD spectra for several surfaces of interest for comparison with the Ni_nTiO₂ samples. For these samples, no desorption of Ni-containing species or CO₂ is observed. The top frame shows the result for CO TPD from clean stoichiometric TiO₂(110), with no Ni cluster deposition. Based on TiO₂ CO TPD results in the literature,²¹ the CO desorption peak for perfect TiO₂(110) under our TPD conditions should be at ~130 K. The ~140 K starting temperature achievable with our transferable sample holders is, therefore, too high to see the main CO desorption peak. In the literature TPD results, for TiO₂ with annealing history similar to ours, a high temperature tail of CO desorption from TiO₂ defect sites is observed, to almost 350 K. We, therefore, attribute the desorption feature observed in our TPD spectrum to CO desorption from defect sites on the surface.

The middle frame shows TPD from single crystal Ni (100), following a ~20 L CO dose at 220 K. A peak is observed at ~420 K, with a shoulder at ~320 K. For a dose about six times lower, the low temperature shoulder disappears. This structure and dose dependence is consistent with the recent detailed TPD study of Muscat and Madix³² which

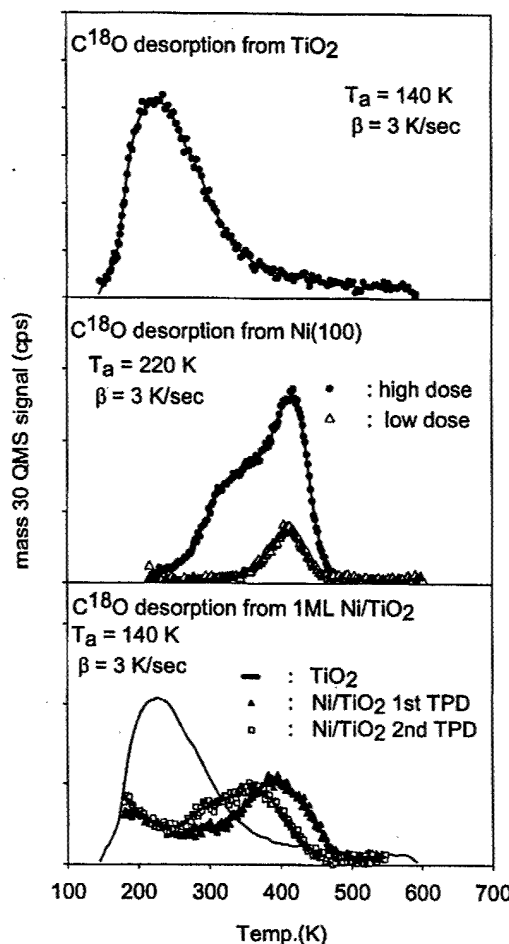


FIG. 6. C^{18}O TPD spectra for comparison with cluster results. Top: Desorption following saturation dose on clean TiO_2 . Middle: Desorption from $\text{Ni}(100)$ at saturation dose, and a dose ~ 6 times lower. Bottom: Desorption from sample prepared by deposition of $2.0 \times 10^{15} \text{ Ni}^+/\text{cm}^2$ (1 ML Ni) on TiO_2 , showing changes between first and second TPD scans, and TPD for clean TiO_2 , for comparison.

showed clearly that a succession of more weakly bound states is filled as CO dose is increased.

The final frame shows an experiment designed for comparison with the study of Raupp and Dumesic.¹² In their study, Ni films were evaporated onto an oxidized polycrystalline Ti surface, then subjected to TPD after various substrate and Ni annealing procedures. In the experiment closest to ours, they deposited 0.2 nm of Ni (~ 1 ML) then did CO TPD with no other pretreatment. In our experiment, we deposited a monolayer ($2.0 \times 10^{15} \text{ Ni}/\text{cm}^2$) as atomic ions at an impact energy of 1 eV. The ISS results indicate that our Ni is aggregating to a limited extent upon deposition at room temperature, leaving about half the TiO_2 surface free of Ni. We measured two sequential TPD runs, in each run cooling the sample, applying a saturation CO dose, then ramping the temperature at 3 K/s to 600 K. The first TPD run, with as-deposited Ni, resulted in a broad peak at 385 K, almost identical to that observed by Raupp and Dumesic for 0.2 nm Ni on fully oxidized titanium. In our second TPD run, the peak broadened and shifted to lower temperature, with a hint of a second peak near 300 K. The ISS results, where the Ni/substrate ratio decreases by 29% following a single TPD

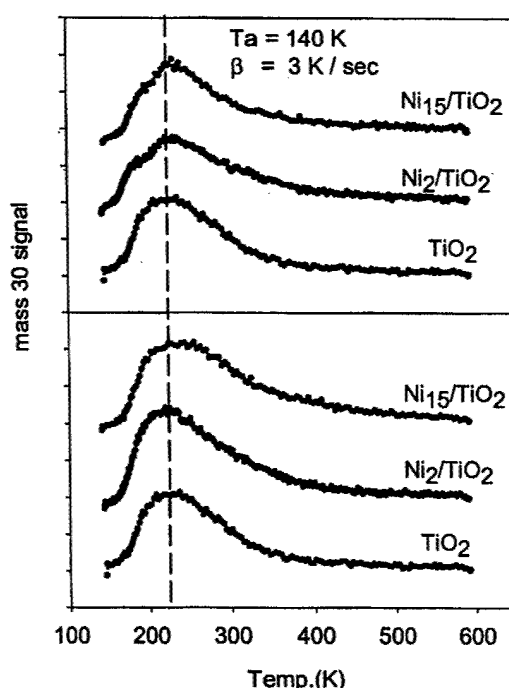


FIG. 7. C^{18}O TPD clean TiO_2 , and from Ni_2 and Ni_{15} supported on vacuum annealed TiO_2 . Top: First TPD run. Bottom: Second TPD run, showing loss of structure.

cycle, suggests that sintering and/or partial encapsulation take place during TPD. Although the conditions were somewhat different, a similar trend was observed by Raupp and Dumesic.

Figure 7 shows C^{18}O TPD spectra run under identical conditions for clean TiO_2 , and TiO_2 with $2.0 \times 10^{14} \text{ Ni atoms}/\text{cm}^2$, deposited as Ni_2^+ , and Ni_{15}^+ at 1 eV/atom deposition energy. The other size clusters and deposition energies give similar results. No mass spectral signal was observed for Ni^+ , $\text{C}^{18}\text{O}_2^+$, or $\text{C}^{16}\text{O}^{18}\text{O}^+$, consistent with XPS indications that the stoichiometry of the near-surface region is not altered by CO TPD. In particular, there is no carbon build-up following TPD. The most obvious point is that there is little change in the TPD due to Ni_n deposition. In the spectra for Ni_2 and Ni_{15} , there is some hint of a shoulder near 190 K, and the high temperature tail extends to somewhat higher temperatures than for the clean TiO_2 . The shoulder structure, though weak, is reproducible. The lower frame of the figure compares the results of a second, sequential TPD run from each sample. Note that the weak shoulder structure observed in the first run is absent.

Several conclusions can be drawn from this result. First, CO binding to small Ni clusters on the surface in low doses is substantially weaker than for the clusters that form in high dose Ni deposition. Whether this is a cluster size effect or an effect of Ni dose-dependent modification of electronic properties is unclear, because it is not known what cluster size distribution forms in the high dose Ni deposition. The ISS results, above, indicate that the TPD cycle of adsorption/desorption and heating leads to substantial sintering and/or encapsulation of the very small clusters ($n = 2, 5$), with less change observed for Ni_{10} , and little for Ni_{15} . Presumably this TPD-induced effect leads to the loss of the weak shoul-

der structure in the second TPD run. Apparently sintering under these conditions does not lead to growth of large Ni clusters that would have significantly increased CO desorption temperatures, perhaps approaching that of bulk Ni (~ 400 K).

The STM work of Tanner *et al.*⁸ provides a useful point of comparison. In their experiment, nickel atoms were evaporated onto a TiO_2 (110) support, and the resulting clusters were imaged. For a dose of 2×10^{14} atoms/cm² at a substrate temperature of 375 K, dome-shaped 1.6 nm diam clusters were obtained. From the reported contact angle, we can estimate that these clusters contain only about 30 atoms. Our cluster dose is about the same, and while we heat to 600 K in our TPD runs, the total time at temperatures above 375 K is <2 min. If the TPD-induced sintering of our small clusters stopped in the 30 atom size range, that would explain several observations. First, the Raupp and Dumesic work suggests that for larger Ni particles on TiO_2 , CO desorption peaks should be observed at higher temperatures, as in our 1 ML Ni^+ experiment. No such peaks are observed in repeated TPD experiments, suggesting that large particles do not grow for the 0.1 ML dose of Ni. Stopping in the 30 atom size range would also explain why the TPD-induced changes in Ni ISS signal are large for Ni_2 and Ni_5 , but smaller for Ni_{10} and especially Ni_{15} . For the small clusters, sintering into multilayer particles leads to a large decrease in the fraction of Ni atoms exposed in the top layer. For Ni_{15} , where the as-deposited structure appears three-dimensional, sintering into a 30 atom cluster would result in only a small change in the fraction of exposed Ni.

We also considered the possibility that CO adsorption might be breaking up the clusters into isolated metal surface carbonyls, which then desorb CO at low temperatures. The nickel would have to reaggregate into clusters during the course of TPD, because the ISS data are inconsistent with increased Ni dispersion following TPD. Because we are not currently able to do ISS/XPS with the sample at low temperatures, we cannot completely eliminate this possibility, but it seems unlikely. In order that we not see CO desorption at high temperatures, the CO–Ni binding must be weak, and in that case, CO adsorption would be unlikely to result in cluster disruption. We did look at XPS and ISS of Ni_n/TiO_2 exposed to a saturation dose of CO at room temperature. No carbon was detected by XPS, and the Ni/O and Ni/Ti ISS ratios were not altered from the values prior to the CO dose. One could argue that we might not see a small coverage of CO by its C 1s XPS signal, but CO binding to Ni atoms would certainly attenuate the Ni ISS signal. It seems clear from this result that at room temperature, CO is not sticking to the Ni in the Ni_n/TiO_2 sample. Furthermore, the lack of change in ISS suggests that CO adsorption/desorption at room temperature does not significantly modify the clusters.

While it is clear that the CO binding is weak for our small clusters, the question is why. The work of Riley and co-workers^{29,33} clearly shows that CO binds to gas-phase Ni_n in our size range, and the results of Heiz and co-workers^{2,34} for Ni_n/MgO indicate that Ni–CO binding is reasonably strong in that system. This comparison suggests that the weak CO binding for low dose Ni/TiO_2 is a consequence of

strong interaction with the support. We observe no desorption of nickel carbonyls for Ni_n/TiO_2 , whereas this is a major TPD channel for the Ni_n/MgO ($n < 4$). In addition, CO is observed to bind both molecularly and dissociatively on Ni_n/MgO ($n > 10$), with TPD peaks at ~ 240 and ~ 600 K, respectively, while no dissociative adsorption is observed for Ni/TiO_2 . We note that DFT calculations indicate nickel atom binding energies are ~ 1 eV for MgO (Refs. 35, 36) and ~ 2.6 eV for TiO_2 .⁶ The stronger binding on TiO_2 presumably results in a concomitant weakening of the CO–Ni binding energies, consistent our observation that CO binding to Ni is comparable to, or weaker than the binding to defects on the TiO_2 surface. Stronger Ni-support binding probably also accounts for our not seeing desorption of nickel-containing species for Ni_n/TiO_2 —the Ni– TiO_2 binding is much stronger than the CO–Ni binding, so that CO cannot volatilize even small Ni clusters. In the Heiz experiments, they have no direct means for examining cluster morphology changes induced by CO adsorption/desorption. Given that we see substantial TPD-induced sintering for Ni/TiO_2 , we would expect extensive TPD-induced sintering in the more weakly bound Ni_n/MgO system, and possibly some diffusion/sintering at room temperature.

ACKNOWLEDGMENTS

Development of the instrumentation and the experiments reported were supported by the Air Force Office of Scientific Research (F49620-00-1-0138), and the Department of Energy, Office of Science, Basic Energy Science Program, under Grant No. DEFG0399ER15003. Support does not constitute endorsement by DOE of the views expressed herein. Development of the instrument was also supported by a seed grant from the University of Utah, and an equipment donation from Kodak, Inc. Rajganesh Pala from Professor Thanh Truong's group (University of Utah) provided prepublication results of his calculations on Ni/TiO_2 binding and useful discussions regarding bonding to TiO_2 . The authors are grateful for many discussions with Professor Jihwa Lee from Seoul National University, and Professor Kevin Boyd from the University of New Orleans.

- 1 F. Vanolli, U. Heiz, and W.-D. Schneider, *Chem. Phys. Lett.* **277**, 527 (1997).
- 2 U. Heiz, *Appl. Phys. A: Mater. Sci. Process.* **A67**, 621 (1998).
- 3 U. Heiz, F. Vanolli, A. Sanchez, and W. D. Schneider, *J. Am. Chem. Soc.* **120**, 9668 (1998).
- 4 U. Heiz and W.-D. Schneider, in *Metal Clusters at Surfaces*, edited by K.-H. Meiwes-Broer (Springer, Berlin, 2000), p. 237.
- 5 U. Heiz and W.-D. Schneider, *Crit. Rev. Solid State Mater. Sci.* **26**, 251 (2001).
- 6 R. Pala, F. Liu, and T. Truong (unpublished).
- 7 H. Onishi, T. Aruga, C. Egawa, and Y. Iwasawa, *Surf. Sci.* **233**, 261 (1990).
- 8 R. E. Tanner, I. Goldfarb, M. R. Castell, and G. A. D. Briggs, *Surf. Sci.* **486**, 167 (2001).
- 9 V. Vijayakrishnan and C. N. R. Rao, *Surf. Sci.* **255**, L516 (1991).
- 10 C. C. Kao, S. C. Tsai, M. K. Bahl, Y. W. Chung, and W. J. Lo, *Surf. Sci.* **95**, 1 (1980).
- 11 J. P. Espinós, A. Fernández, and A. R. González-Elipe, *Surf. Sci.* **295**, 402 (1993).
- 12 G. B. Raupp and J. A. Dumesic, *J. Catal.* **97**, 85 (1986).
- 13 K. J. Boyd, A. Lapicki, M. Aizawa, and S. L. Anderson, *Nucl. Instrum. Methods Phys. Res. B* **157**, 144 (1999).

- ¹⁴A. Lapicki, K. J. Boyd, and S. L. Anderson, *J. Vac. Sci. Technol. A* **18**, 2603 (2000).
- ¹⁵U. Heiz, F. Vanolli, L. Trento, and W. D. Schneider, *Rev. Sci. Instrum.* **68**, 1986 (1997).
- ¹⁶D. A. Shirley, *Phys. Rev. B* **5**, 4709 (1972).
- ¹⁷*Handbook of X-Ray Photoelectron Spectroscopy*, edited by J. F. Moulder, W. F. Stickle, P. E. Sobol, K. D. Bomben, J. J. Chastain, and R. C. King (Physical Electronics, Eden Prairie, MN, 1995).
- ¹⁸C. J. Powell and A. Jablonski, *NIST Electron Inelastic-Mean-Free-Path Database—Version 1.1* (National Institute of Standards and Technology, Gaithersburg, MD, 2000).
- ¹⁹V. S. Lusvardi, M. A. Barteau, J. G. Chen, J. Eng, Jr., A. Teplyakov, and B. Fruhberger, *Surf. Sci.* **397**, 237 (1998).
- ²⁰M. A. Henderson, *Surf. Sci.* **419**, 174 (1999).
- ²¹A. Linsebigler, G. Lu, and J. T. Yates, Jr., *J. Chem. Phys.* **103**, 9438 (1995).
- ²²W. S. Epling, C. H. F. Peden, M. A. Henderson, and U. Diebold, *Surf. Sci.* **412/413**, 333 (1998).
- ²³M. Li, W. Hebenstreit, L. Gross, U. Diebold, M. A. Henderson, D. R. Jennison, P. A. Schultz, and M. P. Sears, *Surf. Sci.* **437**, 173 (1999).
- ²⁴P. G. Bertrand and J. W. Rabalais, in *Low Energy Ion-Surface Interactions*, edited by J. W. Rabalais (Wiley, Chichester, 1994), pp. 55–116.
- ²⁵O. S. Oen, *Surf. Sci.* **131**, L407 (1983).
- ²⁶O. Dulub, W. Hebenstreit, and U. Diebold, *Phys. Rev. Lett.* **84**, 3646 (2000).
- ²⁷S. Takatani and Y.-W. Chung, *J. Catal.* **90**, 75 (1984).
- ²⁸E. K. Parks, B. J. Winter, T. D. Klots, and S. J. Riley, *J. Chem. Phys.* **94**, 1882 (1991).
- ²⁹E. K. Parks, K. P. Kerns, and S. J. Riley, *J. Chem. Phys.* **112**, 3384 (2000).
- ³⁰A. Lapicki, K. J. Boyd, M. Aizawa, M. Popescu, and S. L. Anderson, *J. Vac. Sci. Technol. A* (submitted).
- ³¹S. E. Stein, director, in *NIST Chemistry WebBook, NIST Standard Reference Database Number 69*, edited by W. G. Mallard and P. J. Linstrom, NIST Mass Spec Data Center, National Institute of Standards and Technology, Gaithersburg, MD 20899 (<http://webbook.nist.gov>), 2000.
- ³²A. J. Muscat and R. J. Madix, *J. Phys. Chem.* **100**, 9807 (1996).
- ³³K. P. Kerns, E. K. Parks, and S. J. Riley, *J. Chem. Phys.* **112**, 3394 (2000).
- ³⁴U. Heiz, R. Sherwood, D. M. Cox, A. Kaldor, and J. T. Yates, Jr., *NATO ASI Ser., Ser. C* **465**, 37 (1995).
- ³⁵A. Markovits, M. K. Skalli, C. Minot, G. Pacchioni, N. Lopez, and F. Illas, *J. Chem. Phys.* **115**, 8172 (2001).
- ³⁶I. Yudanov, G. Pacchioni, K. Neyman, and N. Roesch, *J. Phys. Chem. B* **101**, 2786 (1997).

Deposition dynamics and chemical properties of size-selected Ir clusters on TiO₂

Masato Aizawa, Sungsik Lee, and Scott L. Anderson*

Department of Chemistry, University of Utah, Salt Lake City, UT 84112

Abstract

We report a study of Ir_n/TiO₂ samples prepared by size and energy-selected deposition of Ir_n⁺ (n=1, 2, 5, 10, 15) on rutile TiO₂ (110) at room temperatures. The Ir clusters are found to be formally in the zero oxidation state, and there are no significant shifts in Ir 4f binding energy with cluster size. Over a wide range of impact energies, both Ir XPS intensity and peak position are constant, indicating constant sticking coefficient, and no impact-driven redox chemistry. Low energy ion scattering spectroscopy (ISS) suggests that the deposited Ir clusters remain largely intact, neither fragmenting nor agglomerating, and retaining 3-D structures for the larger sizes. For impact energies above 10 eV/atom, comparison of ISS and XPS data show that the Ir clusters are penetrating into the TiO₂ surface, with the extent of penetration increasing with both *per* atom energy and cluster size. Temperature programmed desorption (TPD) of CO is used to further characterize the deposited Ir_n. This system shows pronounced substrate-mediated adsorption (SMA) in low CO exposures, with strong dependence on cluster size. ISS and sputtering experiments indicate that CO adsorbed via SMA is bound differently than CO adsorbed in high dose experiments. In experiments with sequential C¹⁶O and C¹⁸O doses, facile C¹⁶O → C¹⁸O exchange is observed for Ir₅ and larger clusters, but not for Ir₂. The peak CO desorption temperature is found to decrease with cluster size. The cycle of CO adsorption and heating comprising a TPD experiment have a dramatic effect on the sample morphology, leading to encapsulation of Ir by a thin TiO_x layer.

Keywords: Iridium clusters, deposition, titanium dioxide, XPS, LEIS, TPD, substrate mediated adsorption

anderson@chem.utah.edu

I. Introduction

Many catalysts consist of nanometer-sized transition metal clusters supported on metal oxides, and there are many examples in the literature where the chemical properties change with average size of supported clusters. Similar effects have been observed for planar model catalysts, where nanoclusters are grown by metal evaporation onto a single crystal or thin film oxide support. Such experiments allow use of better characterized supports and enable use of scanning probe microscopy to characterize the cluster size and morphology distributions in detail. Still, for the smallest cluster sizes, the size dispersion for clusters grown on a support is non-negligible, and it may not be possible to independent vary metal loading, metal cluster size, and support defect density, because nucleation at defects can be important in cluster formation. An approach that, in principle, allows these three factors to be decoupled, is deposition of pre-formed, size-selected metal clusters on an oxide single-crystal support. Heiz *et al.*[1]developed the first instrument that allowed detailed study of the chemical properties of size-selected deposited clusters, and have reported studies of various metal clusters deposited on MgO thin films.[2-7]

Recently we reported development of an instrument for cluster deposition[8] and its application to the Ni_n/TiO_2 (110) system.[9] Here we report a study of Ir/TiO₂ planar model catalysts prepared by deposition of size and energy-selected Ir_n^+ on single crystal TiO₂. The samples are probed by x-ray photoelectron spectroscopy (XPS), ion scattering spectroscopy (ISS), auger electron spectroscopy (AES), and temperature programmed desorption (TPD). Inclusion of ISS is important, providing insight into the morphology of the as-deposited samples, and into changes induced by adsorbate exposure or heating.

Because Ir is a catalytically interesting metal, a number of studies have been reported on chemical properties of Ir metal and supported Ir catalysts, including Ir/TiO₂. The Ir/TiO₂ system was shown to be promising for partial oxidation of methane in production of synthetic gas[10]. From the perspective of cluster size effects, the work by Gates and co-workers is of particular interest. They prepared Ir/ γ -Al₂O₃ catalysts by decarbonylation of polynuclear iridium carbonyl precursors, providing a method to study catalytic effects of varying Ir particle size.[11] In addition to these catalysis experiments, CO TPD has

been reported for various surfaces of Ir metal[12-14] and Ir particles on different supports[15-17], though not, to our knowledge, for Ir/TiO₂. Finally, several studies have focused on spectroscopic properties and diffusion/sintering behavior of Ir nanoclusters on TiO₂.[18-20]

In addition to the experimental results, a number of theoretical studies are relevant to the Ir/TiO₂ system. Pala *et al.*[21] have examined binding of Ir atoms on different binding sites on defect-free TiO₂ (110), calculated within both the local density and generalized gradient approximations. Both methods give Ir-surface binding energies in excess of 3 eV, with variations between different binding sites exceeding 1 eV. Such a strongly corrugated interaction potential suggests that barriers to Ir diffusion on defect-free TiO₂ should be relatively large. We have not found any studies dealing with Ir binding to TiO₂ defects, however, Horsley [22] examined the interactions of Pt with defective TiO₂ using Xα-SW-SCF calculations. They found that Pt atoms can bind into missing-oxygen defects on the surface, leading to strong Ti-Pt bonding – a prediction that has been verified experimentally.[23, 24]

II. Experimental Section

The experimental setup has been described previously.[8, 9] A laser vaporization source is used to produce Ir_n⁺, which are collected by a rf-quadrupole beamline, mass-selected, and delivered to the TiO₂ substrate in ultra-high vacuum (UHV). In addition to the deposition station, the UHV system contains stations for sample preparation, electron and ion spectroscopy, and temperature-programmed desorption (TPD). The base pressure for most experiments was $\sim 2 \times 10^{-10}$ Torr, however, some test experiments were done after prolonged bake-out, with base pressure $\sim 1 \times 10^{-10}$ Torr.

Rutile TiO₂ (110) single crystals (5 x 5 x 1 mm) from Commercial Crystal Laboratories are clamped against 0.5 mm thick molybdenum backing plates, that serve as electrical contacts and heat diffusers. The mounted crystals are attached to sample holders that differ from those previously described[25] only in being fabricated from OFHC copper. Sample heating is by electron bombardment of the Mo plate from the back side, and cooling is by conduction to a liquid N₂-cooled reservoir. Temperatures are measured with a K-type thermocouple glued into a slot cut in the edge of the TiO₂

crystal. Our preparation procedure for the TiO_2 is similar to that reported by Li and coworkers[26]. To induce enough electrical conductivity for ion deposition and electron/ion spectroscopy, the TiO_2 samples are initially heated to 1000K for 1h in UHV. Prior to each deposition experiment, the surface is cleaned by cycles of 1 keV Ar^+ sputtering and 850K vacuum annealing (20min) until surface impurities such as C and Na are below our detection limit using Auger electron spectroscopy (AES) and low energy ion scattering spectroscopy (ISS). It is known from the STM work of Li and coworkers, that this cleaning/annealing procedure produces a slightly O-deficient, near-stoichiometric $\text{TiO}_2(110)-(1\times 1)$ surface.

Iridium clusters are produced by a 100 Hz laser vaporization/nozzle source similar to that reported by Heiz and coworkers.[1] The cluster ions, entrained in the He carrier gas, are collected by a quadrupole ion guide, where most of the He is pumped away. At the end of the first quadrupole guide, the ion beam is deflected 18°, and injected into a second quadrupole, which guides it through several more differential pumping stages. The cluster size of interest is selected using a conventional quadrupole mass filter, then the ions are injected into a final quadrupole guide, passed through an additional differential pumping stage, and delivered to the TiO_2 target through a 2mm diameter exposure mask. Current is measured directly on the deposition substrate, and the energy spread, determined by retarding potential analysis at the substrate, is better than 1 eV FWHM. The deposition spot size is occasionally profiled by AES, and matches the mask opening within the resolution of our electron gun (~0.3 mm). Pressure during deposition rises to 2×10^{-9} Torr, however, the additional gas load is UHP helium from the source. To check for possible deposition of contaminants from the beamline, samples were examined with AES and TPD following a prolonged exposure under deposition conditions, but with the sample biased to prevent ion impact. No metal deposition is observed, and the level of other surface contaminants is identical to that resulting from a similar time exposure to base pressure. Except for a few experiments noted below, the total Ir dose was fixed at 1.6×10^{14} Ir atoms per cm^2 , corresponding to a tenth of a close-packed Ir monolayer. Deposition times are typically 30 minutes, and do not vary strongly

with cluster size, because the decline in ion current with size is approximately countered by the increase in number of atoms *per* cluster. The exception is Ir⁺, where intensity can be made very large, allowing rapid deposition. Because the cluster beam energy spread is small, the deposition time is also independent of energy, over the entire energy range explored here.

XPS is performed using a Mg K α source with photon energy of 1253.6 eV. To correct for charging due to the low conductivity of the TiO₂ sample, the XPS spectra have been corrected so that the Ti⁴⁺ peak appears at the 459.5 eV binding energy expected for bulk TiO₂.[27] This correction gives O 1s peaks at 530.8 eV, in excellent agreement with literature data for TiO₂.[28-30]

ISS is done using a 1 keV ⁴He⁺ beam, incident at 45° with a current density of ~10 μ A/cm² (6 x 10¹³ cm⁻²•sec⁻¹). Scattered He⁺ ions are collected along the surface normal, thus the scattering angle is fixed at 135 degrees. To minimize surface damage, ISS data are taken quickly – about 30 seconds total exposure to the ion beam for a survey scan, and select experiments were also done with He⁺ exposures about 100 times lower. As shown below, ISS does cause some damage to the surface, in the form of increased density of missing oxygen defects and implanted helium. To probe the effects of sample damage, the main set of 1 eV/atom deposition experiments was run both with, and without ISS characterization. No differences are observed in the Ir XPS. As discussed below, we do find that the CO TPD measurements are modestly affected by pre-TPD ISS characterization, so the main TPD results presented are from the set taken without ISS.

For TPD measurements, C¹⁸O is introduced to the chamber through a leak valve, and doses are estimated from the pressure (3 x 10⁻⁸ Torr) measured using an ion gauge, with correction for sensitivity to CO. Linsebigler *et al.*[31] reported that CO desorption from clean rutile TiO₂ (110)-(1x1) occurs at 150K, but that CO adsorbed at missing oxygen defects desorbs in a long tail extending to ~350K. To minimize background from CO bound to TiO₂, the sample was held at 300K during CO dosing. Before each TPD scan, the heating filament is briefly flashed to remove CO adsorbed on the filament supports. Under these conditions, only a small CO desorption peak at ~340K is observed in absence of deposited Ir,

and no CO desorption is observed in the temperature range of interest for the Ir clusters. TPD experiments involve heating the sample at a rate of 3 K/sec to 800K, then rapidly cooling back to 300 K. Typically, three successive TPD runs are performed to study the effects of TPD-induced changes in sample properties. Finally, after the TPD experiments, XPS and ISS spectra are again recorded to examine the effects of TPD on the oxidation state and morphology of the sample.

The mass spectrometer sensitivity to CO desorbing from the sample was calibrated by measuring TPD from Ni(100) exposed to 0.5 L of CO.[32, 33] The difficulty in translating this sensitivity calibration into a measure of absolute CO coverage on the Ir_n/TiO_2 samples, is that the clusters are deposited in a ~2 mm spot, whereas the Ni single crystal is significantly larger. The TPD mass spectrometer sees the samples through a 45° (half angle) skimmer with a ~3 mm diameter orifice, but the orifice has a smaller internal angle, and it is not clear how the detection sensitivity varies with distance from the center of the cluster spot. Adding the fact that our cluster spot profile is only known with resolution of ~0.3 mm, we feel that our absolute coverage calibration is only good to within a factor of two.

Because CO desorption temperatures from single crystal Ir(110)[13, 14] and Ir(111)[12] are 530K and 550K, respectively, some adsorption of adventitious CO on our supported Ir clusters is expected during deposition and XPS analysis. To quantify the adventitious CO exposure, we also looked at CO TPD from Ni (100) following 1 hour exposure to the deposition chamber background, and following 1 hour in the deposition station with gas flows identical to those during deposition. The amount of CO desorbing following background exposure was 20% of that desorbing following a 0.5 L dose, and was independent of whether the exposure was in the deposition position or not. The estimated adventitious CO exposure for the clusters is ~0.095 L – consistent with the value estimated from the CO partial pressure (~4 x 10^{-11} Torr) and exposure time. For CO at room temperature, 1 L corresponds to 3.8×10^{14} collisions/cm², thus 0.1L exposure corresponds to 2.4% of the density of a close-packed Ir monolayer ($1.56 \times 10^{15}/\text{cm}^2$).

III Results and Discussion

A. X-ray photoelectron spectroscopy

Examples of Ti 2p XPS data are shown in Fig. 1 for freshly annealed TiO_2 (A) and TiO_2 subjected to two ISS survey scans to create additional defects. The expected positions of various Ti oxidation states are indicated by vertical lines.[34] Spectra shown as solid curves are for clean TiO_2 , and the dotted spectra are for TiO_2 with 0.1ML equivalent of Ir_2 deposited at 1eV/atom deposition energy. First consider spectrum (A), for freshly annealed TiO_2 . The intensity in the region where Ti^{3+} shoulder appearance is too low to allow extraction of a precise value of the Ti^{3+} density, with estimates ranging from 3 to 8%, depending on the lineshape assumed for the dominant Ti^{4+} peak. This value provides an estimate for the density of missing oxygen defects in the near-surface region probed by XPS. Adsorbate titration experiments by Diebold *et al.*[35] and Henderson *et al.*[36] showed $7 \pm 3\%$ surface missing oxygen defects for similar annealing conditions. After deposition of 0.1 ML equivalent of Ir_2 , there is a slight general intensity reduction, as expected because Ir on the surface will tend to attenuate photoelectrons from the underlying substrate, and in addition, the relative Ti^{3+} intensity is slightly reduced.

The latter effect is more obvious in the spectra in Fig. 1(B), where two pre-deposition ISS scans were used to create additional Ti^{3+} intensity. From fitting the spectrum, we estimate that the Ti^{3+} concentration in the top few nanometers of the sample has increased to $\sim 18\%$, presumably mostly in the form of missing oxygen defects.[37] ISS, which is sensitive only to the topmost layer, shows a decrease in the O/Ti ISS ratio of $\sim 12\%$. A single ISS scan is expected to cause about half of this much damage. In this case, it is quite clear that the Ti^{3+} intensity decreases upon Ir deposition, and the Ti^{4+} intensity decrease is less than would be expected from attenuation by the overlying Ir (c.f. Fig. 1 (A)). These data indicate that a fraction of the surface Ti^{3+} centers, i.e., Ti at missing oxygen defects, are oxidized to Ti^{4+} by interaction with the deposited Ir. We also considered the possibility that the Ti^{3+} might be oxidized by reaction with background gas during the deposition time, however, the Ti XPS shows no change after

exposure to background for one hour, in absence of Ir deposition. The fact that only a fraction of the Ti^{3+} centers are oxidized simple reflects the facts that the surface Ti^{3+} concentration is higher than the deposited Ir density, and that some of the Ti^{3+} centers are subsurface. For the freshly annealed TiO_2 sample (Fig. 1A), the Ti^{3+} shoulder is too weak to estimate what fraction is oxidized in the deposition process.

Fig. 1 (C) and (D) show the equivalent Ir 4f XPS results for Ir_2 deposited on the TiO_2 samples characterized in (A) and (B), respectively. The Ir XPS is complicated by background from a weak Ti 3s peak, overlapping the expected Ir 4f spectral region. The dotted spectra show the total XPS signal in the Ir 4f spectral region after Ir_2 deposition, and the solid curves *without* point symbols are the Ti 3s spectra measured just prior to Ir_2 deposition. The asymmetrically broadened Ti 3s spectrum in (D) reflects the higher density of Ti^{3+} from ISS damage. The solid curves *with* point symbols are the Ir 4f XPS spectra determined as the difference between the pre and post deposition spectra. The subtraction process clearly decreases the signal/noise ratio for the Ir XPS, however, we are confident that the spectrum is not significantly distorted, because the shapes and intensity ratio of the two fine structure components are in good agreement with Ir 4f XPS spectra in the literature. Because the fine structure provides a consistency check, we feel that the resulting Ir XPS data are accurate enough to allow detection of spectral shifts greater than ~ 0.1 eV, intensity changes greater than $\pm 5\%$, or growth of new spectral features with intensities greater than $\sim 15\%$ of the total intensity. In principle, it should be possible to avoid Ti 3s background by looking at a different Ir XPS band. The 4d band at 298 eV is the only one with sufficient intensity, and indeed, both 4f and 4d XPS were measured routinely. Sadly, the 4d XPS is plagued by even stronger background, in the form of a ghost of the O 1s peak resulting from Al contamination of our Mg anode.

The Ir 4f doublet structure is shifted ~ 0.3 eV to higher binding energy, compared to the binding energy reported for bulk Ir. The shift is in the direction of positive oxidation states of Ir, qualitatively similar to the shift observed by Escard *et al.*[18] for 15 nm mean diameter iridium particles on TiO_2 . They

interpreted the shift as indicating partial oxidation of Ir by the substrate, however, this interpretation is contradicted by our observation that the Ti^{3+} intensity decreases, rather than increasing upon Ir deposition. (Ni_n deposited at high energies on TiO_2 provides an example where deposited metal is oxidized by the support – growth of Ni^{3+} intensity is clearly accompanied by reduction of Ti^{4+} to Ti^{3+}).[9]

Interpretation of XPS binding energies for small metal particles on oxide surfaces is complicated by final state relaxations effects, which can shift binding energies relative to the values measured for bulk materials.[38, 39] Bahl *et al.*[40] and Oberli *et al.*[41] reported a simple method to estimate the final state shift using a combination of Auger and photoelectron energies. The shift in Auger electron kinetic energy (ΔK), relative to the value for bulk metal, is approximately given by $\Delta K = -\Delta E + 2\Delta R$, where ΔE is the core level shift and ΔR is the final state shift. This simple approach is oversimplified, as pointed out by Thomas[42] and Hohlneicher *et al.*,[43] nonetheless, we feel that it is adequate to provide at least a rough indication of the direction of metal-support electron transfer. The Ir 4f XPS for the Ir_n/TiO_2 samples is found to be shifted $\sim 0.3\text{ eV}$ towards higher binding energy, while the Ir LMM Auger peak is shifted 1.5 eV toward lower kinetic energy, relative to the positions measured for Ir foil. The estimated final state shift is, therefore, $\sim 0.6\text{ eV}$, and the observed binding energy shift of $+0.3\text{ eV}$ actually corresponds to a $\sim -0.3\text{ eV}$ shift in the core level energy. In other words, after correction for the final state effect, the XPS data indicate net electron transfer from the TiO_2 to the Ir clusters, consistent with our observation that Ti^{3+} tends to be oxidized by Ir deposition. This conclusion is also consistent with results from Bahl *et al.*,[40] who concluded that XPS of Pt/SrTiO_3 shows net support-to-metal transfer of ~ 0.6 electrons/Pt, after correcting for final state effects. They also showed that, on a slightly reduced surface, deposition of Pt oxidizes surface Ti^{3+} cations, consistent with our observations for Ir/TiO_2 .

Fig. 2 shows the variations in Ir 4f XPS spectra with Ir cluster size and deposition energy. The solid spectra are for as-deposited clusters, and the dotted spectra were taken post-TPD, as discussed below. Table 1 gives integrated XPS peak areas, normalized to the value for 0.1 ML of Ir^+ at 1 eV/atom . Within the $\sim 5\%$ experimental uncertainty, the Ir XPS intensity for as-deposited clusters is independent of

cluster size and nearly independent of deposition energy. The only obvious exception is that the XPS intensity for Ir_2 at 40 eV/atom is only about half the intensity for lower impact energies. XPS intensity is determined by the Ir concentration in the sample, weighted by the variation in detection efficiency with depth. The inelastic mean free path (IMFP) of Ir photoelectrons in TiO_2 is ~ 2.3 nm,[44] thus XPS probes Ir in the top few nanometers of the sample.

Constant XPS intensity indicates that the sticking probability for Ir_n on TiO_2 is size-, and energy-independent, at least for energies below tens of eV/atom. It is hard to imagine a mechanism whereby the sticking probability could be low, but also nearly constant, therefore we infer near-unit sticking probability. Sticking probability can also be estimated from the measured Ir/Ti XPS intensity ratio, as follows. Atomic sensitivity factors measured for our electron energy analyzer[45] and IMFP values for pure Ir and Ti were combined to estimate effective, relative Ir and Ti photoemission cross sections, building in factors relating to detection efficiency for our analyzer. Using these, together with appropriate IMFP values in TiO_2 and Ir, we calculated the expected Ir/Ti XPS ratio for a model 10 nm thick slab of TiO_2 with 0.1 ML of Ir on top (i.e., assuming unit sticking probability). The predicted Ir/Ti XPS ratio is 10.2%, compared to the measured 8.6% ratio. Given the uncertainties resulting from Ti 3s background subtraction and the crudeness of the estimation, we feel that the agreement is about as good as could be expected, reinforces the conclusion that sticking probability is high. Near-unit sticking probability is not unexpected, given the strength of the Ir- TiO_2 interaction (see above). The explanation for the decrease in Ir XPS at the highest impact energies becomes clear in light of the ISS results discussed below.

No significant binding energy shifts or new features are observed, suggesting that the oxidation state of Ir is also independent of cluster size and impact energy. This situation is quite different from the case of Ni_n deposited on TiO_2 [9], where new peaks indicating production of Ni^{3+} are observed for deposition energies of 10 eV/atom and above, indicating impact-driven redox chemistry between Ni and TiO_2 . One might object that because the Ti 3s background peak happens to lie almost exactly between the Ir 4f fine structure components, the apparent position of the fine structure peaks after subtraction will tend

to be insensitive to small shifts in the true Ir 4f XPS spectral position. That may be true to an extent, however, the intensity ratio of the two fine structure components would then be quite sensitive to the shifts. Within the experimental signal/noise, the fine structure intensity ratios are constant across the data set, thus we conclude that the Ir 4f spectral positions really are independent of cluster size and impact energy.

The lack of peak shifts for different cluster size is interesting in light of many previous experiments where binding energies were inferred to shift with cluster size, because of size-dependent final state effects.[38, 39, 46, 47] For example, Fritsch *et al.*[48] studied XPS shifts for Ir evaporated onto carbon with increasing evaporation time. They found that the Ir 4f binding energy is initially shifted 1.0 eV to higher binding energy (relative to bulk metallic Ir), but decreases with time, finally reaching the metallic value. There are several conceivable explanations for why we don't see significant cluster size shifts. From the XPS data alone, one might conclude that our clusters are sintering or fragmenting such that the actual size distribution of Ir on the surface is independent of the deposited cluster size and energy. The ISS results clearly show, however, that this is not the case. More likely, the cluster sizes probed in our experiments are simply too small for there to be significant dependence of the final state relaxation on size.

Photoemission leaves a cluster with a positive charge that is eventually neutralized by electron transfer from the substrate. On semiconducting or insulating substrates, electron transfer from the substrate may be slow compared to the photoemission time scale, so that the final state is determined by only intra-cluster electronic relaxation. If the clusters are truly metallic, then the core hole is screened by the conduction electrons such that the charge appears at the surface of the cluster. As the size is reduced, the final state energy is increased by the coulomb energy, $e^2/2r$, where r is the cluster radius. On the other hand, if the clusters are not metallic, then the extent of screening is limited to localized polarization of the valence electrons, and will not depend strongly on cluster size. Such localized screening was inferred, for example, by Wertheim and co-workers for metal clusters containing fewer than 30 atoms supported on

amorphous carbon.[49-51] In the end, it is difficult to assess what shifts might be expected with cluster size, because the net XPS shift is the result of two partially cancelling effects. Initial state effects (partial electron transfer to the clusters) tend to shift the peak to lower binding energy, while the final state effects tend to shift to higher binding energy. Both effects are expected to die out with increasing Ir cluster size, but not necessarily at the same rate.

B. Low energy ion scattering spectroscopy

Ion scattering spectroscopy (ISS) was used to probe morphology of the cluster/substrate samples. ISS is sensitive to surface structure in several ways. Scattering of 1 keV He^+ can be thought of as isolated binary collisions between He^+ and a single surface atom, in which case, the energy of the scattered He^+ is a simple function of the surface atom mass.[52] As Fig. 3 shows, the ISS spectra for Ir_n/TiO_2 samples consist of three peaks at different He^+ energies (plotted as E/E_0 , where E_0 is the 1 keV initial energy), corresponding to scattering from O, Ti, and Ir. Note that the Ir ISS peak intensity is strongly dependent on the size of the deposited cluster, demonstrating that deposited cluster size has a strong effect on the morphology of the resulting sample. As we will see below, cluster deposition energy also has a strong effect on ISS intensities.

While ISS peak positions are trivially interpreted, intensities are a more complex problem. Intensities can logically be considered to be a convolution of three factors: the cross section for scattering from a particular type of atom, the He^+ ion survival probability (ISP), and shadowing/blocking. For 1 keV He^+ , the scattering cross section depends mostly on the surface atom's core electrons, and therefore is not strongly dependent on oxidation state. For reference, the cross sections (σ) for scattering through 135° were estimated by running classical trajectories for an empirically corrected Molière potential.[52] The cross sections are in the ratio, $0.23 : 1 : 3.5$ for $\sigma_{\text{O}} : \sigma_{\text{Ti}} : \sigma_{\text{Ir}}$.

The most important factor in ISS intensities for our scattering geometry is the ISP, because most He^+ is neutralized during the scattering process. High neutralization probability greatly simplifies the ISS spectra, because only single-scattering events from top layer atoms contribute significantly. The ISP

depends on the electron densities traversed during each scattering event, and thus varies with the chemical element, oxidation state, and local environment of the surface atom. For Ir deposited on top of the surface, the underlying Ti or O atoms are effectively 2nd layer atoms, thus ion scattering from them is greatly attenuated. The oxidation state of the surface atoms can affect ISP, complicating interpretation of ISS if sample oxidation state changes with cluster size or impact energy. For this system, the XPS shows no significant oxidation state changes, therefore the ISS intensity variations must be related to morphology changes. (The effect of oxidation state on ISP can be seen from the presence of a weak peak at $E/E_0 \sim 0.57$ for Ir_5 , attributed to the presence of surface Na. This Na contamination is well below the level detectable by AES, but high ISP for scattering from surface Na^+ enhances the ISS detection efficiency dramatically).

The final effects are blocking and shadowing. Blocking is when He^+ scattered from one atom cannot reach the detector because a second atom is in the way. Because we detect along the surface normal, blocking affects only atoms directly underneath the surface atom, and these 2nd layer atoms already have negligible detection probability. Shadowing refers to the fact that atoms on the surface cast a roughly conical scattering shadow, i.e., scattering from a surface atom prevents He^+ from reaching other atoms that are directly behind it. For reference, the shadow cone radius for 1 keV He^+ scattering from an Ir adatom is estimated[53] to be $\sim 1.2 \text{ \AA}$ at a distance corresponding to the TiO_2 surface layer. In essence, we expect each Ir adatom to shadow about one Ti or O surface layer atom, and because most of these shadowed atoms are bound to the Ir adatom, they would already be expected to have low detection probability because of ISP effects. For grazing incidence scattering, blocking and shadowing effects are large and sharply dependent on surface azimuthal angle,[52] providing a sensitive probe of surface geometry. For our ISS angles, strong azimuthal dependence is not expected, however, we verified this expectation by measuring identical ISS spectra for several different TiO_2 samples mounted at random azimuthal angles.

In essence, ISP and blocking effects completely eliminate ISS signal for scattering from atoms directly beneath Ir adatoms, and ISP and shadowing effects attenuate ISS signal from surface layer atoms immediately surrounding the site of ad-atom binding. As a consequence, we expect the largest Ir ISS peaks and the greatest attenuation of Ti and O ISS peaks (i.e., the largest Ir/Ti and Ir/O ISS peak ratios), should occur for Ir dispersed as atoms on top of the surface. If the deposited Ir is in the form of clusters on top of the surface, there will be less attenuation of Ti and O signal, because areas attenuated by adjacent Ir atoms will tend to overlap to some extent, leaving a larger fraction of the TiO_2 exposed. Note, however, that for our 0.1 ML Ir dose, most of the TiO_2 is exposed regardless of Ir morphology, thus the O and Ti ISS intensities can't change much. Any large changes in Ir/Ti or Ir/O ISS peak ratios must, therefore, originate from changes in Ir signal. If the deposited Ir forms one or two dimensional islands on the surface, the Ir ISS signal should be unchanged, because all Ir atoms are still exposed to the He^+ . The resulting Ir/Ti or Ir/O ratios should be close to the dispersed atom limit. In contrast, if deposition leads to formation of Ir clusters with multilayer structure, then the Ir ISS signal should be substantially reduced, because the top layer Ir atoms will attenuate signal from the lower layers. Similarly, if Ir is implanted or diffuses beneath the TiO_2 surface, or is decorated by adsorbed species, the Ir ISS signal would be strongly attenuated, or entirely absent.

1. Low deposition energies

Absolute ISS intensities taken during the course of several months of experiments were quite reproducible, nonetheless, to compensate for possible variations in He^+ beam intensity, focus, detector gain, etc., our analysis will largely be based on ratios of ISS peaks. Ir/O, Ir/Ti, and O/Ti ISS peak ratios are calculated by integrating the peak areas. Fig. 4 gives the Ir/substrate ratio (average of Ir/O and Ir/Ti) and O/Ti ratio as a function of cluster size, for deposition at 1 eV/atom energy. The O/Ti ratio has been normalized to the value for clean TiO_2 . The ISS intensities are summarized in Table 1. Because deposition times, spot sizes, Ir oxidation state, and sticking probability are all independent of cluster size and impact energy (except possibly at the highest energies), changes in ISS ratios must be related to

morphology changes. The most obvious trend is that the Ir ISS intensity decreases with increasing cluster size (Fig. 3), resulting in Ir/substrate ratios (Fig. 4) that decrease by about a factor of four over the deposited size range. A more subtle effect, evident in Fig. 4, is that the O/Ti ratio depends on cluster size. For the large clusters, the O/Ti ratio is close to the value observed for clean TiO_2 , but the ratio drops by $\sim 10\%$ for the small clusters. These results show that the morphology of the deposited Ir is strongly dependent on the size of clusters deposited. In particular, we can rule out the possibility that the clusters might be sintering or fragmenting extensively, because in either case, the final state of the system would be approximately independent of deposited cluster size.

The most reasonable explanation for the trend in Ir/substrate ratio is that the size of clusters on the surface is strongly correlated with the size deposited, i.e., the clusters are remaining approximately intact. Deposition of Ir and Ir_2 results in high dispersion, so that the Ir/substrate ratio is large. The rapid decrease in Ir/substrate ratio with increasing cluster size implies that an increasing fraction of the Ir is no longer in the top-most layer for the larger clusters, i.e., the supported clusters are multilayer, retaining some memory of their 3-d gas-phase structures. Only a small degree of multilayer character is probably needed to cause a significant change in the ISS. For example, if the structure of deposited Ir_5 were Ir_4 with a single Ir on top, we would expect the signal from the lower four atoms to be significantly attenuated by ISP and shadowing effects.

The cluster size dependence of the O/Ti ratio is also consistent with the clusters remaining approximately intact in low energy deposition. For large multilayer clusters, the O/Ti ratio must be close to the clean TiO_2 limit, both because most of the substrate is free of Ir, and because the cluster "footprint" is large enough that it will tend to attenuate O and Ti ISS signal equally. The decrease in O/Ti ratio with decreasing size indicates that Ir deposited as small clusters binds so that it preferentially attenuates scattering from surface O. The preference is actually quite strong, i.e., 10% of a monolayer equivalent of Ir causes up to a $\sim 10\%$ decrease in the O/Ti ratio.

Further evidence regarding the structure of the supported iridium clusters comes from the decay slope of Ir ISS intensity with He^+ sputtering time, shown in Fig. 5 as Ir/Ti ratios, normalized to the ratios observed for as-deposited clusters. (The Ir/Ti ratio is plotted, rather than Ir/substrate, because O tends to sputter rapidly compared to Ti). This experiment is done simply by leaving the He^+ beam on continuously, and periodically running ISS scans. Only the early, *quasi*-linear part of the time dependence is shown, and the lines are simple linear fits to the data. The times indicated are the start times of each \sim 30 second ISS scan. The sputter rate (slope) is quite strongly correlated with cluster size. The decay is rapid for Ir and Ir_2 , but slows dramatically for the larger clusters, which are inferred to have multilayer structures from the ISS intensities (Fig. 4). This trend is exact what is expected. For multilayer clusters the sputter-induced decay in Ir ISS should be slow because loss of Ir by sputtering is partly offset by exposure of previously hidden Ir. In addition, it is not unlikely that the Ir sputter yield (Ir sputtered/incident He^+) should depend to some extent on the cluster size, because higher Ir-Ir coordination may stabilize against Ir sputtering.

Because the trends in ISS intensities and sputter rates are exactly what is expected if the post-deposition cluster size matches the size selected, we conclude that the clusters are depositing more-or-less intact at 1 eV/atom energy. By more-or-less intact, we are not suggesting that the structure of the clusters is unaffected by deposition, but only that most clusters are not fragmented or sintered. Indeed, the calculations of Pala *et al.*[21] suggest that Ir-TiO₂ binding should be relatively strong even for perfect TiO₂, presumably leading to changes in both geometry and electronic structure relative to the free clusters. Their calculations also suggest that the interaction potential is strongly corrugated, and that probably accounts for the apparent lack of diffusion (i.e. fragmentation or sintering) at room temperature. To the extent that the clusters bind at missing oxygen defects on the surface, this may provide an additional impediment to diffusion.

There are alternative ways to rationalize the decrease in Ir/substrate ratio with increasing cluster size. It might be, for example, that the larger clusters tend to implant or diffuse into the TiO₂ surface. As

discussed below, we do observe such implantation behavior, however, the threshold for implantation is well above 1 eV/atom. A large decrease in Ir ISS would also be expected if the clusters become adsorbate covered, or encapsulated by TiO_x during the deposition process. There is some evidence for possible encapsulation when the samples are heated above 600K, but not at room temperature. The effect of both adventitious and deliberately dosed adsorbates on ISS signal is discussed below, however, it is clear that adsorbate effects are far too small to account for the cluster size effects.

For comparison, Fig. 4 also gives results for Ni_n deposition on TiO_2 , taken under identical conditions[9]. The smaller ISS intensity observed for Ni is expected because the scattering cross section scales with atomic number. Note that the Ni/substrate ratio is nearly constant up to Ni_{10} , and decreases only for Ni_{15} . We take this as evidence that the small Ni clusters flatten on the surface during deposition, so that the transition to multilayer structure only occurs for large clusters. The greater tendency of Ni_n to flatten is favored by the smaller Ni - substrate mass ratio, which makes the TiO_2 surface effectively stiffer for Ni_n impacts. Perhaps more importantly, Ir shows a greater tendency than Ni toward multilayer growth on TiO_2 , as shown by experiments where low energy metal atomic ions were deposited. Table 1 shows metal/substrate ISS ratios for 0.1 and 1.0 ML depositions of Ni and Ir. Note that the Ir/substrate ratio increases by only a factor of 2.8 between 0.1 and 1.0 ML, implying that Ir tends to form multilayer clusters at high doses, leaving the TiO_2 mostly Ir-free. In contrast, the Ni/substrate ratio grows by a factor of 16, indicating that Ni is covering a large fraction of the TiO_2 . Caution is warranted in interpreting these results because of possible metal dose effects on ISP, nonetheless, Ir clearly has a greater tendency toward multilayer growth than Ni.

A surprising point in common between the Ir and Ni results, is that the metal/substrate ISS ratios are smaller, and the O/Ti ratio larger, for deposition of atomic ions, relative to dimers. As discussed above, this observation is counter to expectations based on ISP and shadowing considerations, and XPS shows no difference in sticking probability for atoms v.s. dimers. While we can only speculate regarding the origin of such subtle effects, a not unreasonable explanation is that some deposited atoms might be

binding substitutionally into missing oxygen defect sites. These missing O atoms expose underlying Ti centers, and thus tend to decrease the O/Ti ratio, relative to that for a perfect surface. Ir atoms binding into these defects would block ISS signal from the underlying Ti centers, rather than attenuating O signal, which seems to be the propensity for Ir bound on top of the surface. Both effects would tend to increase the O/Ti ratio, as is observed. Substitutional binding into defect sites might also account for the decrease in Ir/substrate ratio, because Ir atoms bound *into* the TiO₂ top layer would attenuate substrate signal less than Ir bound on top, and might also have lower ISP because the defect sites are electron rich.

2. Effects of impact energy

ISS was also performed following deposition over a wide range of impact energies. In comparing different size clusters, it is not clear whether impact dynamics should scale with total energy, total momentum or *per* atom energy or momentum. We have opted to carry out experiments at certain values of energy/atom, i.e., clusters are impacted at certain velocities. For Ir₁₀ and Ir₁₅, we also did experiments at lower energy/atom values, so that it is possible to make at least limited comparisons of different clusters at similar total impact energies. The energy/atom range studied is somewhat constrained by cluster size because our ~1eV kinetic energy spread precludes very low energy/atom impacts for small clusters, and the electrometer used to measure cluster current complicates the problem of depositing at high total energies. It should be noted that the spot size (profiled by AES) and beam intensity (i.e., deposition time) are independent of energy over the range studied, so that the observed effects cannot be attributed to spot size or contamination issues.

Fig. 6 compares ISS spectra taken following Ir₂ and Ir₁₀ depositions over a wide energy range, and the complete data set is summarized in Table 1. At low energies, both cluster sizes give significant Ir ISS peaks, although the peak intensity decreases with cluster size, as discussed above. With increasing impact energy, the Ir ISS signal decreases substantially – much more than the decrease in Ir XPS intensity (Table 1). For example, at 20 eV/atom, the Ir₂ XPS is still 95% of the low energy value, while the ISS intensity is down to 41%, and the difference is even greater at 40 eV/atom. The XPS results show

that most, or all, of the Ir is still in the top few layers of the sample, while ISS shows that most of the Ir is no longer in the top layer, i.e., Ir is penetrating into the substrate. For the dimer, the XPS intensity decrease at high energies could be taken as evidence of a decrease in sticking probability, however, penetration also decreases XPS intensity, and the ISS data show that penetration is the dominant effect. For the larger clusters, the XPS intensity remains high as the ISS drops, ruling out significant drops in sticking probability.

For larger clusters, the penetration becomes significant at lower *per atom* energies, as can be seen by noting that the ISS decrease for Ir_{10} at 10 eV/atom is greater than for Ir_2 at 20 eV/atom. Such a trend is not surprising – the large, three dimensional clusters transfer large total impact energy and momentum to a relatively small "footprint" on the surface. The more facile penetration observed for the larger clusters raises the question of whether there is already some penetration for Ir_{10} or Ir_{15} at the 1 eV/atom energy compared in Figs. 3 and 4. As shown in Table 1, however, the Ir/substrate ISS ratios at 1 eV/atom are identical, within the experimental uncertainty, with ratios taken at much lower energies, indicating that significant penetration occurs only at higher energies.

The behavior observed for Ni_n/TiO_2 is quite different. The Ni/substrate ISS ratios increased slightly at high impact energy for the larger clusters. We interpret this effect as indicating that some fraction of the larger Ni clusters retain multilayer structure when deposited at low energies (though much less so than for Ir_n), and that with increasing energy there is increased tendency to flatten on the surface, rather than penetrating. As expected for such a scenario, the Ni XPS intensities are independent of impact energy, indicating that all Ni remains on the surface. Note, however, that high impact energy does lead to oxidation of a small fraction of the deposited Ni (to Ni^{3+}), not observed for Ir. The tendency of Ni_n to flatten on the surface while Ir_n penetrates, may reflect differences in the interaction potential of the two metals with TiO_2 , but also is expected from the impact kinematics. The mass of Ir is more than seven times the average atomic mass of TiO_2 , while Ni is only a bit more than twice the average surface atom mass. At a given energy/atom, momentum/atom increases like the square root of atomic mass, thus Ir_n

has nearly twice the momentum/atom of Ni_n . Additional momentum should facilitate displacement of surface atoms, enhancing penetration.

Yamaguchi *et al.*[54, 55] studied energy dependent deposition of size-selected Ag_n ($n=1, 3, 5, 7, 9$) on highly oriented pyrolytic graphite (HOPG) by measuring Ag 3d XPS intensity. Their results showed that for energies below ~ 30 eV, the sticking probability decreases with increasing energy, presumably reflecting the weak binding of Ag on HOPG. At higher energies, sticking increases again, eventually plateauing at a value about twice that observed for the lowest impact energies. This change in energy dependence was taken as evidence for Ag penetration (or possibly creation of defects) which binds the metal to the surface, resulting in high sticking efficiency. The threshold energy (eV/atom) for the onset of penetration tends to decrease with increasing cluster size, as in the Ir_n/TiO_2 system.

In summary, the XPS, ISS, and sputter-rate results all are consistent with a scenario where clusters deposit with unit sticking probability, on top of the surface, and more-or-less intact, for low deposition energies. With increasing impact energy, the clusters begin to penetrate the TiO_2 surface, becoming completely buried for energies above some size-dependent limit. There is no evidence of cluster-surface redox chemistry even at high impact energies.

C. Temperature programmed desorption

C^{16}O and C^{18}O adsorption/desorption behavior was studied to further characterize the deposited Ir clusters. To examine the chemical consequences of ISS damage, the TPD experiments were done with and without pre-TPD ISS characterization. The two data sets are similar, but unless specifically noted, the results presented are from the set with no pre-TPD ISS. In addition to C^{18}O and C^{16}O , we monitored desorption of C^{18}O_2 and $\text{C}^{16}\text{O}^{18}\text{O}$, and looked for residual surface carbon by AES. CO desorption was the only significant channel.

Before describing our CO adsorption/desorption results, it is useful to review the STM results of Solymosi *et al.*[20, 56] In their experiments, Ir nanoparticles were grown by Ir evaporation onto a TiO_2 (110)-(1x2) support, followed by various annealing treatments. The (1x2) surface differs from our

stoichiometric (1x1) surface in that every other row of oxygen atoms is missing. For the lowest Ir coverages used in their experiments, the Ir particle size (1 - 1.5 nm, 8 - 10 atoms) was in the middle of the range we deposit. After imaging the nanoparticles, the samples were exposed to high pressures of CO (10^{-3} mbar) for several minutes at 300K, after which they were re-imaged. It was found that particles with diameters \sim 1.5 nm (10 atoms), were disrupted to isolated Ir(CO)₂ species. IR spectroscopy was used to identify the dicarbonyl species, and also to follow the CO adsorption/breakup process. The breakup process was slow enough to be time-resolved for 3-4 nm Ir clusters, but too fast to follow by IR spectroscopy for the small clusters. The major difference between their experiment and ours, other than the use of a different TiO₂ surface, was the CO dose. Our doses vary from 0.1 L to 5 L, whereas their lowest dose was \sim 10⁵ L. In addition to the particle breakup observed upon CO exposure at 300K, they also examined samples annealed with, and without CO exposure. In both cases, they observed formation of large (several hundred atom) particles. Based on their results, we can anticipate strong CO adsorption and thermal effects on the clusters.

1. The nature of CO binding, and effects of adventitious CO

CO is the only gas present in the chamber background that adsorbs significantly on Ir_n/TiO₂ at room temperature. To quantify the adsorption of adventitious CO on the Ir_n/TiO₂ samples, experiments were run where Ir_n was deposited (in \sim 30 minutes), then the samples were allowed to stand in the deposition chamber until the total time since the beginning of deposition was exactly 1 hour. As described above, the adventitious CO exposure under these conditions is 0.1 L. These samples were then probed by TPD with no additional CO dosing. Fig. 7(A) shows the Ir cluster size dependence of the TPD signal resulting from 0.1 L exposure to adventitious CO. No CO desorption is observed in this temperature range from clean TiO₂, even following large CO exposures, thus the desorption is clearly associated with Ir. The desorption temperature is in the same range observed for Ir single crystals, [12-14] and shifts slightly to lower temperatures and sharpens as the cluster size increases. Because the sample morphology changes in the course of TPD (see below), the broad desorption feature does not

necessarily reflect a distribution of CO binding sites, and may be affected by the kinetics of thermally driven rearrangement processes.

The solid circles in Fig. 7(B) represent the integrated desorption peak areas ($T \geq 400$ K), normalized to the value for Ir_2 . The open circles show desorption intensity for as-deposited clusters exposed to a deliberate 5 L CO dose, prior to TPD. For the adventitious exposure alone, CO coverage decreases strongly with increasing cluster size, whereas the coverage following a 5 L dose is nearly size-independent. A surprising result is that the amount of CO desorbing for the 0.1 L adventitious dose is only a factor of ~ 1.5 to 3 times smaller than for the 5L dose. For reference, a 5L dose corresponds to 1.9×10^{15} CO molecules impinging *per* cm^2 , i.e., all exposed Ir atoms are likely to experience a direct CO collision. The 0.1L exposure corresponds to 3.8×10^{13} CO molecules/ cm^2 , so that each exposed atom has only about a 2.4% chance for a direct CO collision. Even given the uncertainties of our mass spectrometer sensitivity calibration, it is clear that considerably more CO desorbs from the as-deposited clusters than could be explained if adsorption occurred only in direct CO-on-Ir collisions.

Instead, we conclude that CO must be adsorbing on the TiO_2 , then migrating to stable binding sites in association with Ir clusters. This process has variously been termed “reverse spillover” or substrate mediated adsorption (SMA), and has been discussed by many authors. See for example, the review of Conner and Falconer[57], papers by Henry and co-workers[58], Rumpf *et al.*[59], Boudart and co-workers[60, 61], or Dellwig *et al.*[62]. Because SMA depends mostly on the support, the recent study by Bowker *et al.*[63] of CO SMA on $\text{Pd}/\text{TiO}_2(110)-(1\times 1)$ is particularly relevant to our results. They found that the heat of adsorption of CO on TiO_2 is about 38 kJ/mol, and for a catalyst with 12% coverage of Pd, CO SMA was significant for temperatures up to 330K. In our experiments, the support is at room temperature and the Ir dose is 0.1 ML, thus significant SMA is to be expected. The SMA mechanism can also account for the inverse correlation of adventitious CO coverage with cluster size (Fig. 7(B)). The probability of a CO molecule diffusing to a stable Ir-associated binding site is inversely proportional to the average distance between clusters, which increases with cluster size, particularly if the larger clusters

have multilayer structures. In order to interpret the effects, it is useful to work out the maximum possible CO coverage. The 0.1L ($3.8 \times 10^{13}/\text{cm}^2$) adventitious CO dose corresponds to 24% of the 1.6×10^{14} Ir atoms deposited per cm^2 as clusters. Therefore, if the SMA mechanism is 100% efficient, the maximum adventitious CO adsorption level is about one CO for every four Ir atoms. Within the uncertainties of our mass spectrometer sensitivity calibration, it appears that the SMA efficiency approaches unity for deposited dimers, decreasing to ~40% for Ir_{15} .

The adventitious CO coverage seen for the as-deposited clusters raises the question of how adventitious CO might affect the clusters and/or our ISS/XPS measurements. The worst-case scenario would be that the deposited clusters are disrupted by interaction with adventitious CO, similar to the effects seen by Solymosi and co-workers. In fact, they observed no cluster disruption for modest CO exposures, still far in excess of our adventitious CO exposure.[64] Even without physically disrupting the clusters, however, there could be effects on XPS or ISS. For XPS, the presence of CO clearly has little effect. We can compare XPS for as-deposited clusters with adventitious CO, clusters grown by very rapid atomic ion deposition where there is little adventitious CO, and clusters with 5 L CO exposures. Within experimental error, there are no shifts in XPS peak positions, and no changes in XPS intensities. ISS, on the other hand, is highly sensitive to adsorbates if they bind so as to attenuate scattering from underlying atoms. This sensitivity raises questions regarding interpretation of the ISS, but also provides an opportunity to probe the nature of the CO binding.

The nature of CO binding was probed by examining the effects of 1 keV He^+ sputtering on the Ir ISS signal, relying on the observation that CO sputters much more rapidly than Ir. For example, a single ISS scan after cluster deposition results in a ~63% decrease in the amount of adventitious CO desorbing in subsequent TPD, but only causes a ~2% decrease in the Ir XPS signal. Consider a sample where CO is bound to Ir in such a way that it attenuates Ir ISS, i.e., on top of the clusters. In that case, the Ir ISS intensity should initially increase rapidly as He^+ sputters away the CO, decreasing only after long sputter times when the slower Ir removal becomes dominant. If, on the other hand, CO is bound in such a way

that it does not attenuate Ir ISS, then CO removal would result in little change in Ir ISS intensity, which should simply decrease slowly with sputter time. To allow us to monitor the initial stages of the rapid CO sputtering, the He^+ beam intensity was reduced by a factor of ~ 15 relative to our normal ISS conditions. In addition, only the Ir region of the ISS spectrum was scanned, reducing the He^+ exposure in a single scan to about 1% of that in a normal ISS survey scan. Under these conditions ($\sim 2 \times 10^{13} \text{ He}^+/\text{scan}$), sample damage and CO loss should be negligible during the initial scan.

The results are shown in Fig. 8. Because the intensity is so low, the data have been fit to gaussians, intended only as guides to the eye. Consider the top row of data, showing the results for a 5 L dose on Ir_2 and Ir_{10} . The data have been normalized, and the absolute ISS signal for Ir_2 is a bit more than twice that for Ir_{10} (see Fig. 3). The initial (most intense) ISS spectrum is for as-deposited Ir_n with only adventitious CO. The second (weakest) ISS spectrum was taken immediately after a 5L dose of C^{18}O . This dose is large enough that most of the exposed Ir atoms will have had a direct encounter with CO impinging from the gas phase, in addition to whatever CO is adsorbed via the SMA mechanism. After the 5L dose, the Ir ISS signal decreases by a factor of three (four) for the dimer (10-mer), indicating that the additional adsorbed CO is bound so that it attenuates Ir ISS. After the 5 L dose, the He^+ beam was left on and ISS spectra were run periodically to examine sputter-induced changes in the Ir ISS signal. As expected from the considerations discussed above, the Ir ISS signal increases significantly as the overlying CO sputters away, exposing Ir. After ~ 15 minutes the Ir signal begins to drop, indicating that the rate of Ir sputtering overtakes the rate at which CO sputtering exposes fresh Ir. The more complete recovery for Ir_{10} is consistent with the lower Ir sputter rates seen for the larger clusters (Fig. 5).

The bottom row shows the same experiment, but without the 5 L saturation dose. In this case, the sputter-induced increase in Ir ISS signal is much smaller. The maximum Ir ISS signal appears after ~ 10 minutes (compared to 15 min for the 5L dose), and is only 15% greater than the signal for as-deposited clusters. Based on the observation that $\sim 63\%$ of adventitious CO is lost in one normal ISS survey scan, 10 minutes under low flux conditions should remove $\sim 70\%$ of the CO, assuming single exponential time

dependence. By extrapolation to zero CO coverage, we can crudely estimate that adventitious CO adsorption results in only ~20% attenuation of Ir ISS signal, relative to the signal expected in absence of CO. Because the changes in Ir ISS signal with cluster size and impact energy are much larger than 20%, it is clear that adventitious CO is only a minor factor in the ISS analysis. In fact, the adventitious CO effect on the ISS survey data (Figs. 3-6, Table 1) is probably only ~10%, because about half the CO will have been lost by the time the survey scans reached the Ir energy range.

The data in Fig. 8 also suggests a tendency for adventitious CO to populate different binding sites compared to the sites populated in high CO exposures. For the moment, assume that there is no difference in binding sites, and recall (Fig. 7B) that the CO coverage following the 5 L dose only increases by a factor of 1.5 or 2 (for Ir_2 and Ir_{10}) compared to the adventitious coverage. Extrapolating from the ~20% ISS attenuation deduced for the adventitious CO coverage, attenuations following the 5 L dose should be in the 30% or 40% (Ir_2 , Ir_{10}) range, relative to hypothetical samples with no CO. Relative to the signal for as-deposited clusters, therefore, the 5L dose should result in additional attenuations of ~13% and ~25% for Ir_2 and Ir_{10} . As Fig. 8 shows, the 5L dose actually attenuates the Ir ISS signal by ~70% and 75% (Ir_2 , Ir_{10}), i.e., the additional CO coverage from the 5 L dose has larger than expected effect. The conclusion is that CO adsorbed at low doses is mostly in sites where it does not attenuate Ir ISS, while at higher doses CO populates sites where Ir ISS attenuation is large.

Adventitious CO is mostly adsorbed by SMA, i.e., CO diffuses across the surface to reach Ir_n . From the observation that adventitious CO causes little Ir ISS attenuation, we infer that this "SMA-delivered" CO tends to bind at sites associated with the periphery of the clusters, rather than on top. This propensity may result from the SMA adsorption mechanism, or may simply reflect higher stability for the peripheral sites. In high CO doses, a significant fraction of the CO binds on top of the clusters, where ISS attenuation is large. In high doses, the SMA mechanism is still active, but there is also a high probability for CO to impinge directly on Ir from the gas phase. It may be that this directly impinging CO is responsible for populating the on top sites, while SMA populates peripheral sites. Alternatively, it might

be that the peripheral sites are simply saturated at higher CO doses, so that later-adsorbing CO is forced into sites on top of the clusters. In any case, the point that low and high doses populate different sites is also supported by the TPD results, discussed next.

2. CO exchange, and the effects of TPD on the clusters.

Fig. 9 shows a series of TPD experiments for Ir_2 and Ir_{10} . It should be noted that each data set (A - F) represents a separate deposition on freshly annealed TiO_2 . Traces A and D show the signal for C^{16}O desorbing from as-deposited clusters, i.e., desorption of the adventitious ("0.1L") dose. The small feature at low temperatures, also seen for clean TiO_2 , is attributed to CO bound at defects on the TiO_2 surface, as discussed by Linsebigler *et al.*[31] The middle and top sets of spectra show desorption of C^{16}O and C^{18}O (and total = $\text{C}^{16}\text{O} + \text{C}^{18}\text{O}$) for as-deposited clusters that were dosed with 0.5L and 5.0 L of C^{18}O , prior to the TPD experiment. By comparing the data sets, it can be seen CO at the TiO_2 defect sites undergoes complete $\text{C}^{16}\text{O} \rightarrow \text{C}^{18}\text{O}$ exchange. The run-to-run variations in the intensity of the low temperature feature reflect the fact that each data set is a separate experiment, with some variation in the concentration of defects capable of binding CO at room temperature. This low temperature feature has been omitted in the peak integrations used to generate Fig. 7 (B).

The behavior for the Ir-associated high temperature feature is more complicated. Consider first Ir_2 . For the 0.1L $\text{C}^{16}\text{O} + 0.5\text{L} \text{C}^{18}\text{O}$ dose sequence (middle data set), roughly equal amounts of C^{16}O and C^{18}O desorb, but with distinct temperature dependences. The C^{16}O feature has intensity, shape, and peak temperature similar to that for C^{16}O in the bottom frame, while the C^{18}O feature is shifted to significantly lower temperature. Evidently for the dimer, adventitious C^{16}O bound via SMA is mostly in sites stable enough to resist $\text{C}^{16}\text{O} \rightarrow \text{C}^{18}\text{O}$ exchange during the subsequent 0.5 L room temperature C^{18}O exposure. In addition, the lower peak desorption temperature for C^{18}O suggests that the SMA-populated sites are nearly saturated by the adventitious exposure, forcing the later-arriving C^{18}O into less stable sites. From the sputtering results, we tentatively identify the more stable SMA sites as being peripheral (little Ir ISS attenuation), and the less stable sites being in some fashion on top of the clusters, where Ir ISS attenuation

is strong. For the 0.1L C¹⁶O + 5.0L C¹⁸O dose sequence (top data set), most of the C¹⁶O is still not exchanged, and the main effect of the higher dose is additional broadening of the C¹⁸O feature toward lower temperatures, with some evidence of bi-modal behavior in the total CO desorption spectrum.

For the larger clusters exemplified by Ir₁₀, the effects of the 0.5L and 5.0L C¹⁸O doses are larger than for Ir₂, and qualitatively different. There is clearly substantial C¹⁶O → C¹⁸O exchange at room temperature, as shown by the suppression of C¹⁶O desorption with increasing C¹⁸O exposure. Furthermore, C¹⁶O and C¹⁸O have similar bi-modal desorption features, unlike the case of Ir₂, where C¹⁶O and C¹⁸O desorb in separate peaks. Evidently, C¹⁶O → C¹⁸O exchange not only removes C¹⁶O, but can also displace it into less stable sites. The C¹⁶O removal must occur at room temperature, but the site exchange may also occur during the TPD heating. It is not clear why the larger clusters (n≥5) show C¹⁶O → C¹⁸O exchange, while the dimer does not. As Fig. 7 shows, there is some decrease in CO binding energy with increasing cluster size, but the effect is too small to account for the qualitatively different behavior for Ir₂. More likely, the difference relates to the multilayer structure of the larger clusters. It is possible, for example, that multilayer clusters rearrange to two dimensional structures upon CO exposure, in order to increase the number of the stronger-binding peripheral sites. Such rearrangement might also explain why the additional CO uptake in the 5 L exposure is much greater for the larger clusters (Fig. 7 (B)), resulting in near size-independent coverage.

Several observations make it clear that the heating cycle used in TPD has a major effect on the morphology of the supported clusters. As noted, we typically run two or three sequential TPD scans on each sample, and the temperature dependence of the CO desorption during the first scan is quite different from those observed in the subsequent scans. This effect can be seen for the case of Ir₂ deposited at 1 eV/atom in the top set of TPD curves in Fig. 10 (A). Note that the amount of CO desorbing is substantially smaller for the second scan, and the desorption peak is shifted to lower temperatures. Similar effects are seen for the larger clusters. Third TPD scans are similar to the second scans, indicating that the TPD-induced changes in the samples are largely complete in a single TPD cycle.

The ISS and XPS results provide some insight into the nature of the TPD-induced changes. The dotted curves in Fig. 3 show ISS data obtained just after the set of TPD runs. Note that the Ir ISS signal is greatly reduced, indicating that most of the deposited Ir is no longer on the surface. One interpretation might be desorption of Ir as some carbonyl compound, too heavy to be monitored by the mass spectrometer used for TPD. Ir desorption can be ruled out, however, based on the XPS results shown in Fig. 2, where the post-TPD spectra are given as dotted curves. For the 1 eV/atom data, the post-TPD XPS intensities are at least 75% of the values for the as-deposited clusters, indicating that most of the Ir is still in the near-surface region. The TPD-induced attenuation of Ir ISS and XPS signals, relative to their pre-TPD values, are summarized in Fig. 10 (B) for depositions at 1 eV/atom. Particularly for the small clusters, the attenuations are large – 80% for ISS and 25% for XPS. Similar effects are observed for heating without CO exposure, indicating that the morphology changes are driven thermally.

Comparison of the ISS and XPS results shows that while the Ir is no longer in the top-most layer of the sample, most of the Ir is still present in the near-surface region. There are two obvious mechanisms that might account for this morphology change. The Ir might be sintering into larger, multilayer particles, where the Ir in the lower layers is invisible to ISS and detected with reduced sensitivity by XPS. The average particle thickness would need to be about three layers to account for the ISS and XPS attenuations. Alternatively, it might be that the clusters are partially encapsulated during TPD. TiO_2 is a reducible support, and many metal/ TiO_2 catalysts show evidence of strong metal support interaction (SMSI), sometimes including encapsulation of the metal nanoparticles by a TiO_x layer. See, for example, the review by Persaud and Madey.[65] Diebold and coworkers,[66] observed Pt encapsulation upon annealing of Pt/ TiO_2 , reporting post-anneal ISS data very similar to our post-TPD ISS, and demonstrated encapsulation by atomically imaging the TiO_x layer by STM.

From the ISS and XPS intensities alone, we cannot distinguish between the sintering and encapsulation mechanisms, as both would result in large ISS reductions with smaller reductions in XPS intensity. Several factors favor the encapsulation mechanism, however. Perhaps the most obvious is the

CO desorption behavior. Note that our first TPD run CO desorption temperatures are not strongly cluster size-dependent, and in the same range as is observed for bulk Ir. If sintering were the morphology change induced by TPD, then we would not expect the 2nd run TPD to differ dramatically from the first. The fact that they are so different, suggests that the surface is chemically altered in the first run, as would be the case if encapsulation is occurring. Our results are qualitatively similar to those of Belton *et al.*,[67] who studied CO desorption chemistry from Rh/TiO₂, where Rh encapsulation by TiO_x was observed after annealing to 760K. Encapsulation reduced the intensity of the CO desorption peak attributed to Rh-bound CO, and generated an additional desorption peak at lower temperature, associated with formation of the TiO_x encapsulating layer. The second factor favoring the encapsulation mechanism is the appearance of a small Ti³⁺ signal in the Ti XPS following TPD, indicating increase in the concentration of reduced Ti. Ti³⁺ is expected in an encapsulation mechanism, because the encapsulating layer is typically partially reduced TiO_x.[68-70] The only results strongly suggesting a sintering mechanism are those of Solymosi and co-workers for Ir on TiO₂(110)-(1x2), where particle coarsening is observed by STM following annealing. In fact, it is not unlikely that both sintering and encapsulating may be occurring, but encapsulation appears to best account for the changes in surface chemical properties.

The TPD data also suggest an interesting role of defects in the Ir/TiO₂ system. The data indicated by filled and open circles in the top frame of Fig. 10 (A) are for Ir₂ deposited on TiO₂ with low defect density. We also studied TPD from TiO₂ subjected to two ISS scans, estimated to increase the defect density to ~18%. As already mentioned, the additional defects (missing oxygen and implanted He) have little effect on the first TPD scan (not shown) other than a slight increase in the intensity of the low temperature peak ($T_{peak} \approx 340K$) attributed to CO bound at TiO₂ defect sites. On the other hand, the ISS-generated defects have a large effect on the TPD-induced morphology changes, as shown by the second TPD scan (open triangles, Fig. 10 (A)). Note that the amount of CO desorbing and the desorption temperature are both dramatically reduced, suggesting that the presence of defects enhances the encapsulation process, or possibly changes the stoichiometry of the encapsulating layer.

Finally, Fig. 10 (A) also shows the effects of deposition energy on the TPD behavior for Ir_2 . Note that as deposition energy is increased, the amount of CO desorbing in the first TPD scans decreases, but the temperature dependence is not strongly affected. By 40 eV/atom there is no CO desorption, consistent with the conclusion from ISS that no Ir remains on the surface at this energy. Somewhat surprisingly, significant CO desorption reappears in a second TPD scan, suggesting that the initially implanted iridium atoms are migrating closer to the surface, where they can influence CO binding.

IV. Conclusions

Size-selected Ir clusters deposit approximately intact on top of TiO_2 (110)-(1x1) for deposition energies of 1 eV/atom and lower. The Ir is formally in the zero oxidation state, and both the oxidation state and sticking probability are independent of cluster size and impact energy, within experimental error. At impact energies in the tens of eV/atom range, the Ir clusters penetrate into the TiO_2 support, with penetration being more facile for the larger clusters. CO desorption was used to probe the chemical nature of the supported clusters. The desorption temperatures are slowly varying with cluster size, and in the same range where CO is observed to desorb from bulk Ir. Both sputtering and CO isotope exchange experiments indicate that there are two CO binding sites. CO adsorbed by substrate mediated adsorption in low CO exposures binds so that it does not attenuate Ir ISS, presumably in sites at the periphery of the clusters. CO impinging directly on Ir in higher CO exposures binds such that Ir ISS is strongly attenuated, indicating that the CO is on top of the clusters. Despite the observation that CO desorption temperatures are not strongly cluster size dependent, the tendency for $\text{C}^{16}\text{O} \rightarrow \text{C}^{18}\text{O}$ exchange is markedly higher for the larger clusters, compared to the dimer. The heating attendant on TPD results in major morphology changes in the samples, most likely in the form of encapsulation of the clusters in a TiO_x layer.

Acknowledgment

Development of the instrumentation and the experiments reported were supported by the Department of Energy, Office of Science, Basic Energy Science Program, under Grant No. DEFG0399ER15003, and the Air Force Office of Scientific Research (F49620-00-1-0138). Support does

not constitute endorsement by DOE of the views expressed herein. Development of the instrument was also supported by a seed grant from the University of Utah, and an equipment donation from Kodak, Inc. Rajganesh Pala and Professor Thanh Truong (University of Utah) provided prepublication results of their calculations on metal/TiO₂ binding and useful discussion. The authors are grateful for many discussions with Professor Jihwa Lee from Seoul National University, and Professor Kevin Boyd from the University of New Orleans.

References

- [1] U. Heiz, F. Vanolli, L. Trento and W.-D. Schneider, *Rev. Sci. Instrum.* 68 (1997) 1986.
- [2] U. Heiz, *Appl. Phys. A: Mater. Sci. Process.* A67 (1998) 621.
- [3] U. Heiz, F. Vanolli, A. Sanchez and W.-D. Schneider, *J. Am. Chem. Soc.* 120 (1998) 9668.
- [4] U. Heiz, A. Sanchez, S. Abbet and W.-D. Schneider, *Eur. Phys. J. D* 9 (1999) 35.
- [5] A. Sanchez, S. Abbet, U. Heiz, W.-D. Schneider, H. Häkkinen, R. N. Barnett and U. Landman, *J. Phys. Chem. A* 103 (1999) 9573.
- [6] S. Abbet, A. Sanchez, U. Heiz and W.-D. Schneider, *J. Catal.* 198 (2001) 122.
- [7] U. Heiz and W.-D. Schneider, *Crit. Rev. Solid State Mater. Sci.* 26 (2001) 251.
- [8] K. J. Boyd, A. Lapicki, M. Aizawa and S. L. Anderson, *Rev. Sci. Instrum.* 69 (1998) 4106.
- [9] M. Aizawa, S. Lee and S. L. Anderson, *J. Chem. Phys.* 117 (2002) 5001.
- [10] K. Nakagawa, N. Ikegami, T. Suzuki, T. Kobayashi and M. Haruta, *Appl. Catal. A* 169 (1998) 281.
- [11] B. C. Gates, *J. Mol. Catal. A: Chem.* 163 (2000) 55.
- [12] D. I. Hagen, B. E. Nieuwenhuys, G. Rovida and G. A. Somorjai, *Surf. Sci.* 57 (1976) 632.
- [13] B. E. Nieuwenhuys and G. A. Somorjai, *Surf. Sci.* 72 (1978) 8.

- [14] J. L. Taylor, D. E. Ibbotson and W. H. Weinberg, *J. Chem. Phys.* 69 (1978) 4298.
- [15] K. Tanaka, K. L. Watters and R. F. Howe, *J. Catal.* 75 (1982) 23.
- [16] F. J. C. M. Toolenaar, A. G. T. M. Bastein and V. Ponec, *J. Catal.* 82 (1983) 35.
- [17] J. L. Falconer, P. R. Wentzcek and H. Wise, *J. Catal.* 45 (1976) 248.
- [18] J. Escard, B. Pontvianne and J. P. Contour, *J. Electron Spectrosc. Relat. Phenom.*, 6 (1975) 17.
- [19] D. A. Buchanan, M. E. Hernandez, F. Solymosi and J. M. White, *J. Catal.* 125 (1990) 456.
- [20] A. Berko and F. Solymosi, *J. Phys. Chem. B* 104 (2000) 10215.
- [21] R. Pala, F. Liu and T. Truong, priv. comm. (2003)
- [22] J. A. Horsley, *J. Am. Chem. Soc.* 109 (1979) 2870.
- [23] S. Fischer, K.-D. Schierbaum and W. Gopel, *Vacuum* 48 (1997) 601.
- [24] K. D. Schierbaum, F. Fischer, M. C. Torquemada, J. L. D. Segovia, E. Roman and J. A. Martin-Gago, *Surf. Sci.* 345 (1996) 261.
- [25] A. Lapicki, K. J. Boyd and S. L. Anderson, *J. Vac. Sci. Technol. A* 18 (2000) 2603.
- [26] M. Li, W. Hebenstreit and U. Diebold, *Surf. Sci. Lett.* 414 (1998) 951.
- [27] Q. Guo, S. Lee and D. W. Goodman, *Surf. Sci.* 437 (1999) 38.
- [28] D. Robba, D. M. Ori, P. Sangalli, G. Chiarello, L. E. Depero and F. Parmigiani, *Surf. Sci.* 380 (1997) 311.
- [29] W. Gopel, J. A. Anderson, D. Frankel, M. Jaehnig, K. Phillips, J. A. Schafer and G. Rocker, *Surf. Sci.* 139 (1984) 333.
- [30] L.-Q. Wang, K. F. Ferris, A. N. Shultz, D. R. Baer and M. H. Englehard, *Surf. Sci.* 380 (1995) 352.
- [31] A. Linsebigler, G. Lu and J. T. Yates, Jr., *Chem. Phys.* 103 (1995) 9438.

- [32] J. Lauterbach, M. Wittmann and J. Kueppers, *Surf. Sci.* 279 (1992) 287.
- [33] A. J. Muscat and R. J. Madix, *J. Phys. Chem.* 100 (1996) 9807.
- [34] C. D. Wagner, A. V. Naumkin, A. Kraut-Vass, J. W. Allison, C. J. Powell and J. R. Rumble Jr., NIST Standard Reference Database 20, Web Version 3.2 (2000).
- [35] U. Diebold, J. Lehman, T. Mahmoud, M. Kuhn, G. Leonardelli, W. Hebenstreit, M. Schmid and P. Varga, *Surf. Sci.* 411 (1998) 137.
- [36] M. A. Henderson, W. S. Epling, C. L. Perkins, C. H. F. Peden and U. Diebold, *J. Phys. Chem. B* 103 (1999) 5328.
- [37] J.-M. Pan, U. Diebold, L. Zhang and T. E. Madey, *Surf. Sci.* 295 (1993) 411.
- [38] Y. Takasu, R. Unwin, B. Tesche and A. M. Bradshaw, *Surf. Sci.* 77 (1978) 219.
- [39] M. G. Mason, *Phys. Rev. B* 27 (1983) 748.
- [40] M. K. Bahl, S. C. Tsai and Y. W. Chung, *Phys. Rev. B* 21 (1980) 1344.
- [41] L. Oberli, R. Monot, H. J. Mathieu, D. Landolt and J. Buttet, *Surf. Sci.* 106 (1981) 301.
- [42] T. D. Thomas, *J. Electron Spectrosc. Relat. Phenom.* 20 (1980) 117.
- [43] G. Hohlneicher and H. Pulm, *J. Electron Spectrosc. Relat. Phenom.* 37 (1985) 209.
- [44] S. Tanuma, C. J. Powell and D. R. Penn, *Surf. Interf. Anal.* 17 (1991) 911.
- [45] J. F. Moulder, W. F. Stickle, P. E. Sobol, K. D. Bomben and J. J. Chastain & R. C. King, eds., in: *Handbook of X-ray Photoelectron Spectroscopy*, (Physical Electronics, Minnesota, 1995).
- [46] J. P. Espinos, A. Fernandez, A. R. Gonzalez-Elipe and G. Munuera, *Surf. Sci.* 251/252 (1991) 1012.
- [47] V. Vijayakrishnan and C. N. R. Rao, *Surf. Sci.* 255 (1991) L516.
- [48] A. Fritsch, Legare, P., *Surf. Sci.* 145 (1984) L517.

- [49] S. B. Dicenzo and G. K. Wertheim, in: Clusters of atoms and molecules 2, Eds. H. Harberland (Springer, Berlin, 1994)p 361.
- [50] G. K. Wertheim and S. B. DiCenzo, Phys. Rev. B 37 (1988) 844.
- [51] G. K. Wertheim, Z. Phys. D 12 (1989) 319.
- [52] P. G. Bertland, in: Low Energy Ion-Surface Interactions, Eds. J. W. Rabalais (Wiley, New York, 1994)p55.
- [53] O. S. Oen, Surf. Sci. 131 (1983) L407.
- [54] W. Yamaguchi, K. Yoshimura, Y. Tai, Y. Maruyama, K. Igarashi, S. Tanemura and J. Murakami, Chem. Phys. Lett. 311 (1999) 341.
- [55] W. Yamaguchi, K. Yoshimura, Y. Tai, Y. Maruyama, K. Igarashi, S. Tanemura and J. Murakami, J. Chem. Phys. 112 (2000) 9961.
- [56] A. Berko and F. Solymosi, Surf. Sci. 411 (1998) L900.
- [57] J. W C Conner and J. L. Falconer, Chem. Rev. 95 (1995) 759.
- [58] C. R. Henry, Appl. Surf. Sci. 164 (2000) 252.
- [59] F. Rumpf, H. Poppa and M. Boudart, Langmuir 4 (1988) 722.
- [60] M. Boudart, M. A. Vannice and J. E. Benson, Z. Phys. Chem. 64 (1969) 171.
- [61] M. Boudart, J. Mol. Catal. A: Chem. 138 (1999) 319.
- [62] T. Dellwig, J. Hartmann, J. Libuda, I. Meusel, G. Rupprechter, H. Unterhalt and H.-J. Freund, J. Mol. Catal. A: Chem. 162 (2000) 51.
- [63] M. Bowker, P. Stone, R. Bennett and N. Perkins, Surf. Sci. 497 (2002) 155.
- [64] A. Berkó and F. Solymosi, priv. comm. (2003).
- [65] R. Persaud and T. E. Madey, in: Chemical Physics of Solid Surfaces, Vol. 8, Eds. D. A. King and D. P. Woodruff (Elsevier, Amsterdam, 1997) p407.

- [66] O. Dulub, W. Hebenstreit and U. Diebold, Phys. Rev. Lett. 84 (2000) 3646.
- [67] D. N. Belton, Y.-M. Sun and J. M. White, J. Catal. 102 (1986) 338.
- [68] F. Pesty, H.-P. Steinruck and T. E. Madley, Surf. Sci. 339 (1995) 83.
- [69] J. M. Pan and T. E. Madley, Catal. Lett. 20 (1993) 269.
- [70] H.-P. Steinruck, F. Pesty, L. Zhang and T. E. Madley, Phys. Rev. B 51 (1995) 2427.

Figure Captions

Fig. 1. Ti 2p XPS for (A) freshly annealed TiO_2 and (B) TiO_2 subjected to 2 ISS scans. Solid curves are samples without Ir deposition. Dotted curves are spectra acquired after deposition of Ir_2 on the corresponding TiO_2 surfaces at an impact energy of 1 eV/atom. C and D: Ir 4f XPS spectra for 0.1 ML equivalent of Ir_2 deposited at 1 eV/atom on freshly annealed TiO_2 , and TiO_2 subjected to 2 ISS scans. Dotted curves are total XPS spectra taken after Ir_2 deposition. Spectra indicated by solid curves are Ti 3s XPS background spectra taken prior to Ir_2 deposition. The Ir 4f XPS (solid curves with dots) are obtained by subtracting the Ti 3s peaks from the corresponding total XPS signal. Expected peak positions for various Ti and Ir oxidation states in bulk materials are indicated by vertical dotted lines.

Fig. 2. Ir 4f XPS for Ir_n ($n=1, 2, 5, 10, 15$) deposited on TiO_2 at various impact energies. Spectra indicated by solid curves are for as-deposited clusters. Dotted spectra were taken after TPD measurements.

Fig. 3. ISS spectra for Ir_n ($n=1, 2, 5, 10, 15$) deposited on TiO_2 at an impact energy of 1 eV/atom. The solid and dotted spectra are acquired for as-deposited and post-TPD Ir clusters, respectively.

Fig. 4. Ir/substrate, Ni/substrate, and O/Ti ISS intensity ratios as a function of Ir cluster size. The metal/substrate ratios are the average of the metal/O and metal/Ti ratios. The O/Ti ratios are normalized to the value obtained for clean, freshly annealed TiO_2 . The Ni/substrate data is taken from Aizawa *et al.* [9]

Fig. 5. Dependence of Ir/Ti ISS intensity ratios on He^+ sputtering time for Ir_n ($n=1-15$) deposited on TiO_2 at an impact energy of 1 eV/atom.

Fig. 6 Effect of impact energy on the ISS spectra for Ir_2 (bottom) and Ir_{10} (top) deposited on TiO_2 .

Fig. 7 (A). C^{16}O temperature-programmed desorption (TPD) spectra from Ir_n ($n=2, 5, 10, 15$) deposited on TiO_2 at an impact energy of 1eV/tom. The TPD spectra were acquired at a heating rate of 3K/s after room temperature adventitious C^{16}O exposures estimated to be 0.1 L. (B) Normalized CO desorption intensity ($T > 400\text{K}$) following $\sim 0.1\text{L}$ (solid circles) and 5L CO exposures (open circles) as a function of Ir cluster size.

Fig. 8. Effect of CO dose and He^+ sputtering time on Ir ISS intensity for Ir_2 and Ir_{10} deposited on TiO_2 at an impact energy of 1eV/atom. The He^+ ion flux is decreased by a factor of 15 compared with that used to take the ISS survey spectra. The data are fitted to gaussians, intended only as guides for the eye.

Fig. 9 CO desorption spectra for Ir_2 (A-C) and Ir_{10} (D-F) deposited on TiO_2 at an impact energy of 1eV/atom after (A and D) $\sim 0.1\text{L}$ adventitious exposure to C^{16}O , (B and E) $\sim 0.1\text{L}$ exposure to C^{16}O and 0.5L dose of C^{18}O , (C and F) $\sim 0.1\text{L}$ exposure to C^{16}O and 5L dose of C^{18}O .

Fig. 10 (A) Effect of Ir_2 impact energy and TPD experiments on CO desorption spectra acquired after a 5L dose of C^{18}O . The CO^+ intensity is sum of both adventitious C^{16}O and dosed C^{18}O intensities. (B) TPD-induced attenuation of Ir ISS (open rectangles) and Ir 4f XPS (solid circles) relative to their pre-TPD values as a function of the Ir cluster size. The data are obtained for Ir clusters deposited at an impact energy of 1eV/atom.

Table 1. ISS and XPS intensity dependence on Ir and Ni cluster size and impact energy.

Dosage	Cluster	Energy (eV /atom)	Metal / substrate ISS ratio ^a		Relative Ir 4f XPS Intensity ^b	
			As deposited	After TPD	As deposited	After TPD
0.1 ML	Ir	1	0.18	0.05	1.00	0.83
	Ir ₂	1	0.21	0.05	1.00	0.75
		10	0.18	0.06	0.97	0.71
		20	0.17	0.07	0.95	0.32
		40	0.04	0.02	0.48	0.18
	Ir ₅	1	0.12	0.05	1.05	0.75
		10	0.07	0.00	1.04	0.97
	Ir ₁₀	0.3	0.09	0.07	1.03	1.02
		1	0.08	0.05	1.02	0.98
		10	0.03	0.04	0.96	0.92
	Ir ₁₅	0.07	0.05	0.03	0.95	0.90
		1	0.05	0.03	0.98	0.92
		5	0.04	0.00	0.99	0.92
1.0 ML	Ir	1	0.51	0.23	8.85	6.62
0.1 ML	Ni	1	0.066	0.027		
	Ni ₂	1	0.077	0.023		
		10	0.056	0.027		
	Ni ₅	1	0.074	0.0526		
		10	0.082	Not taken		
	Ni ₁₀	1	0.085	0.045		
		10	0.125	0.045		
	Ni ₁₅	1	0.015	0.013		
1.0 ML	Ni	1	1.073	0.76		

^aAverage of Metal/O and Metal/Ti ratios

^bNormalized to intensity of Ir 4f XPS for Ir atom at 1eV.

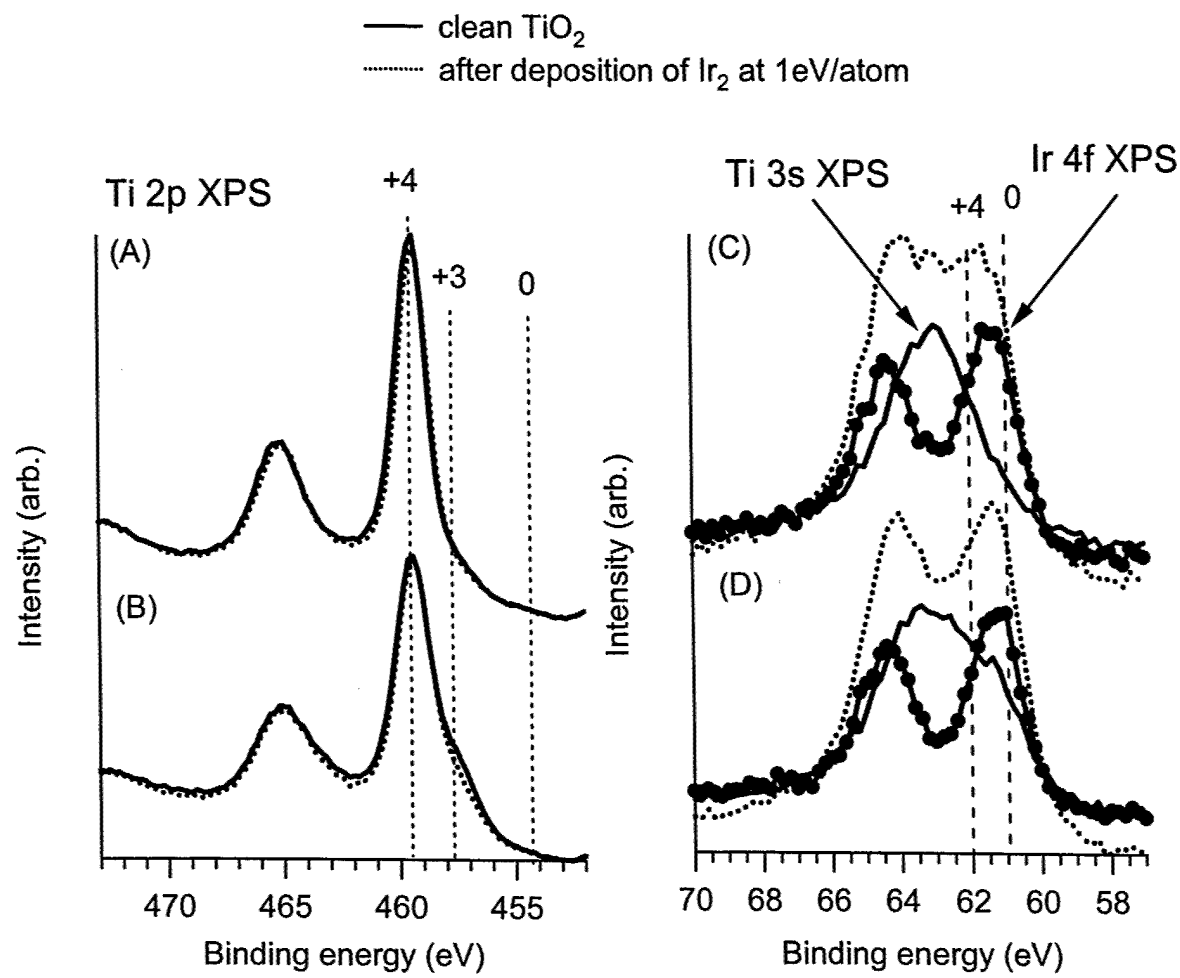


Fig. 1 Aizawa et.al.

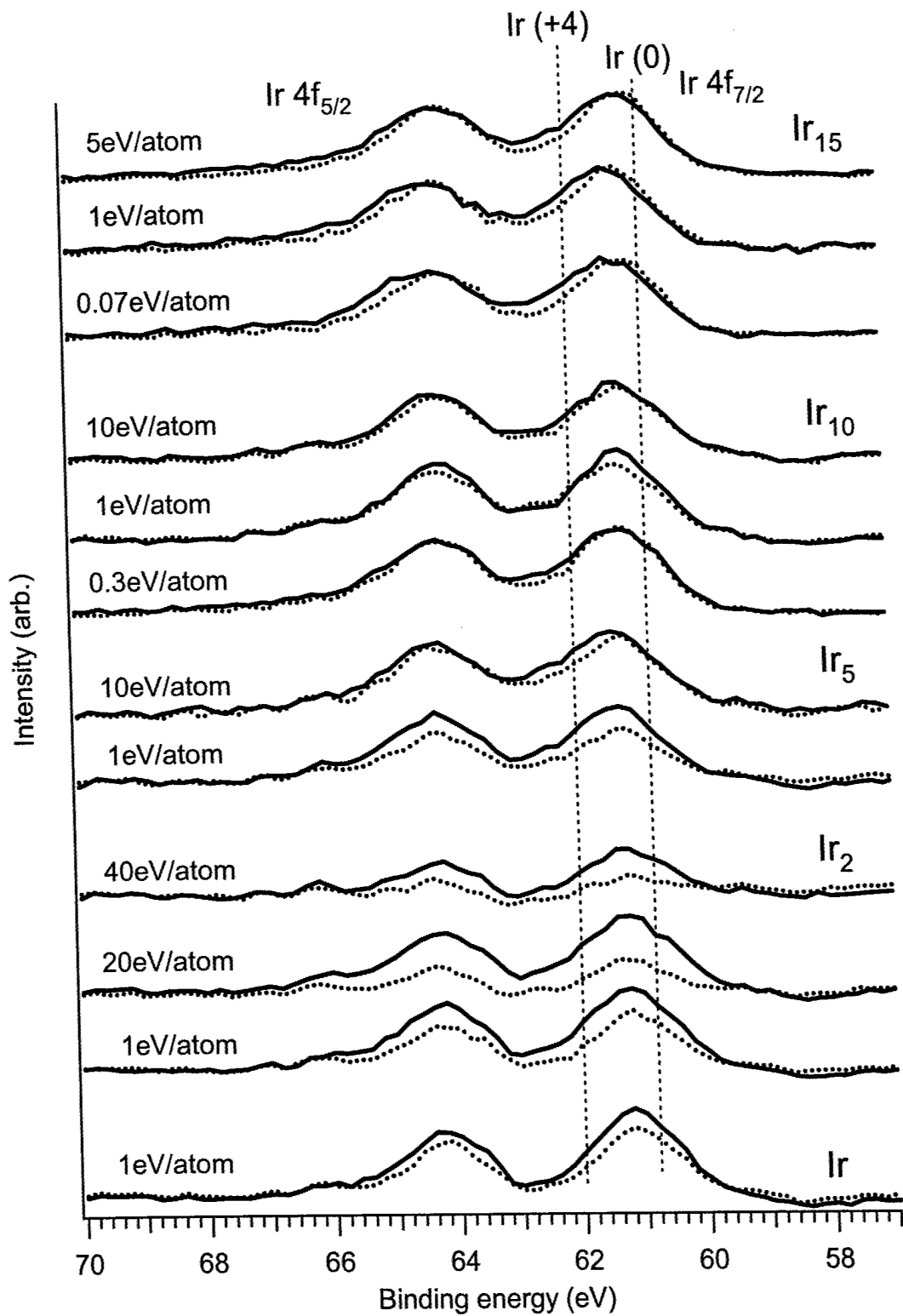


Fig. 2 Aizawa et.al.

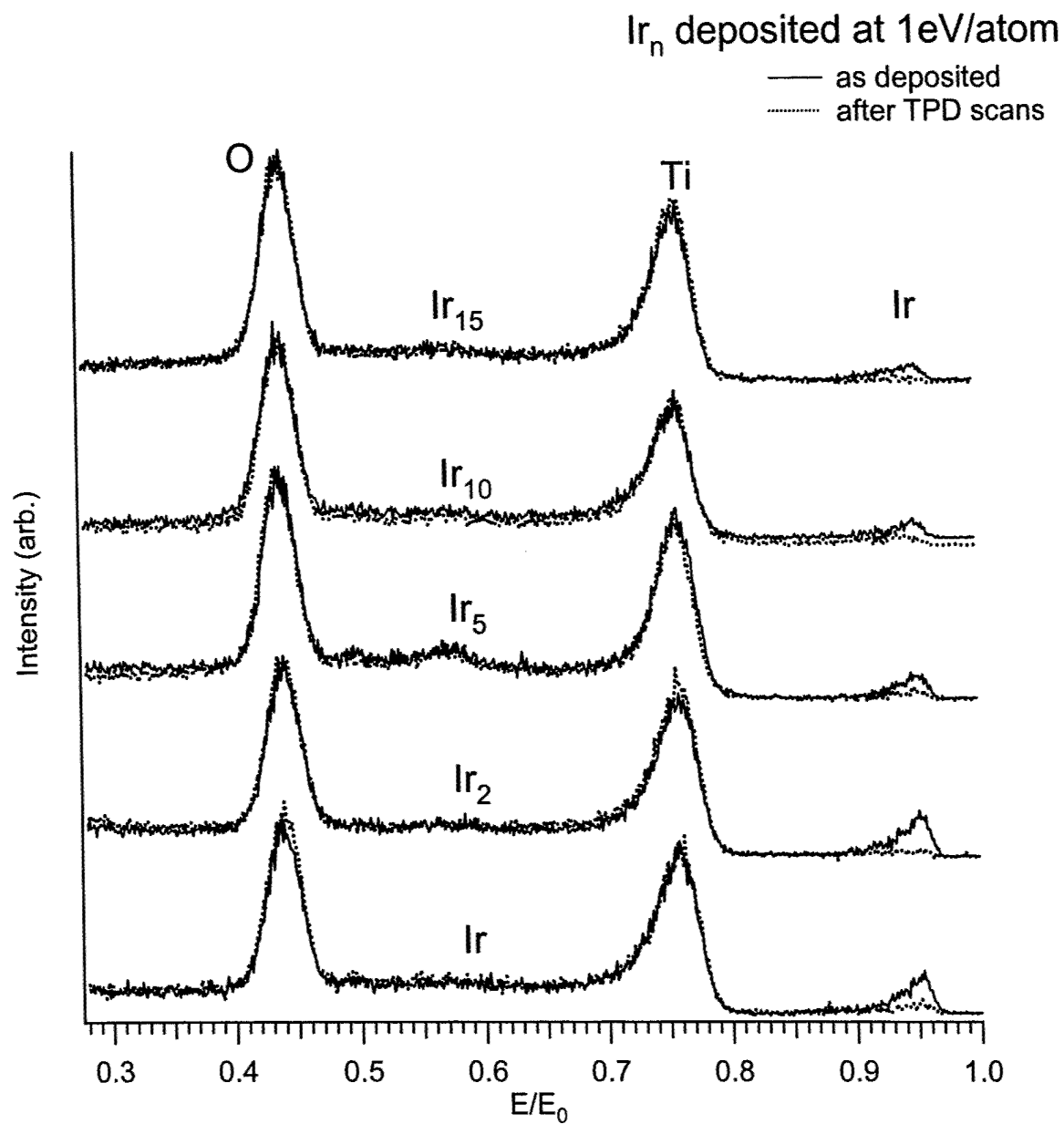


Fig. 3 Aizawa et.al.

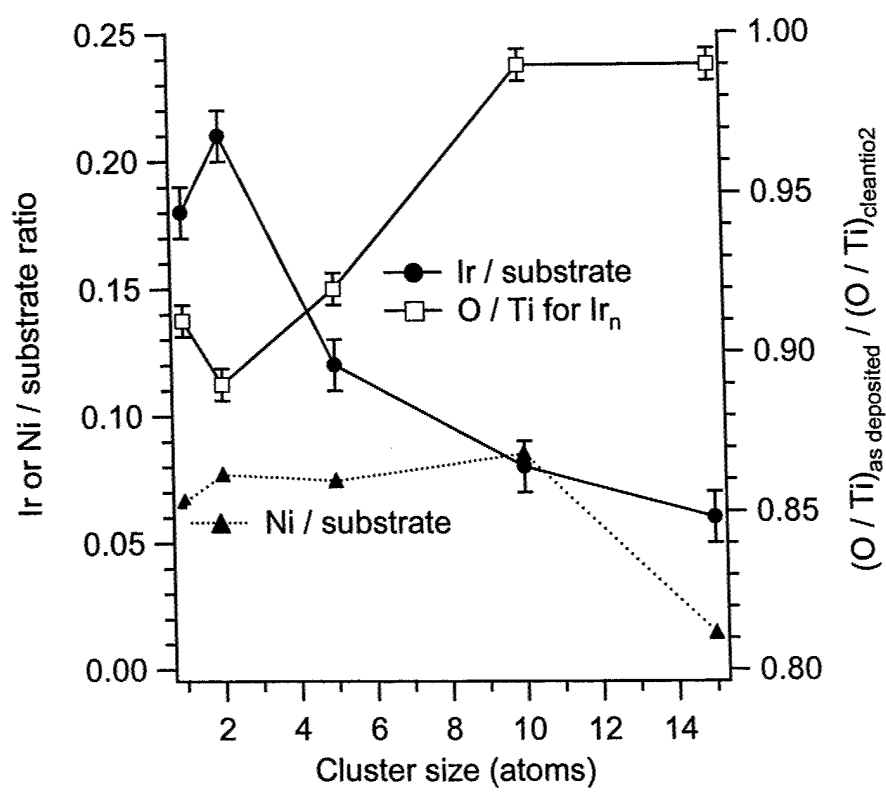


Fig. 4 Aizawa et.al.

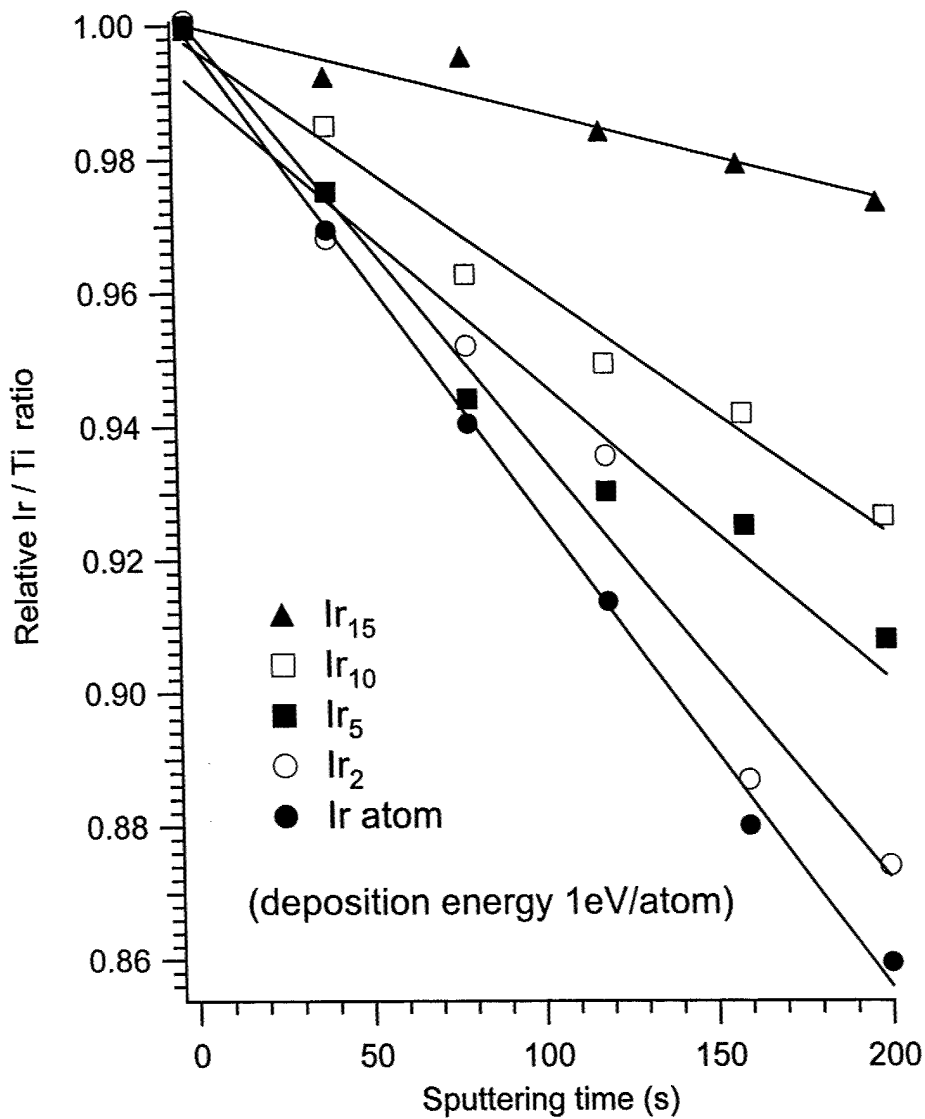


Fig. 5 Aizawa et.al.

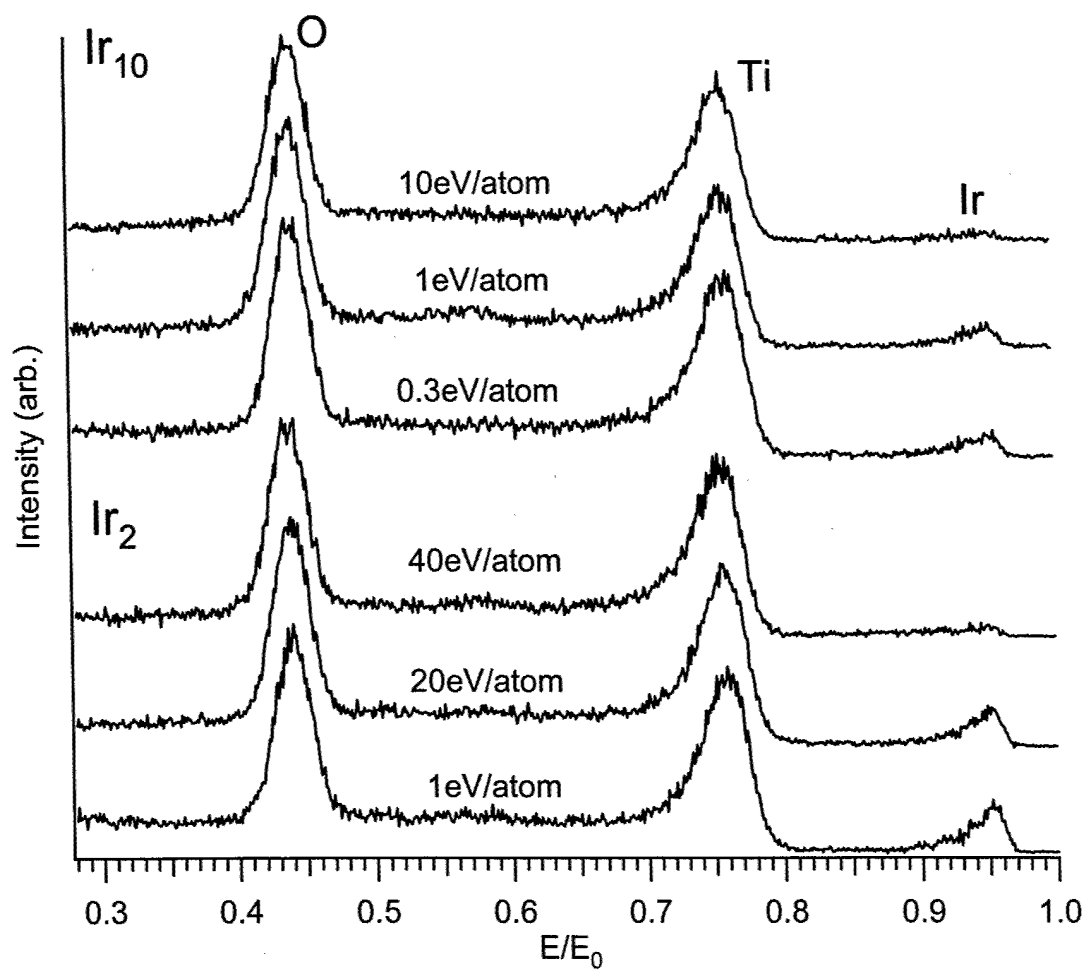


Fig. 6 Aizawa et.al.

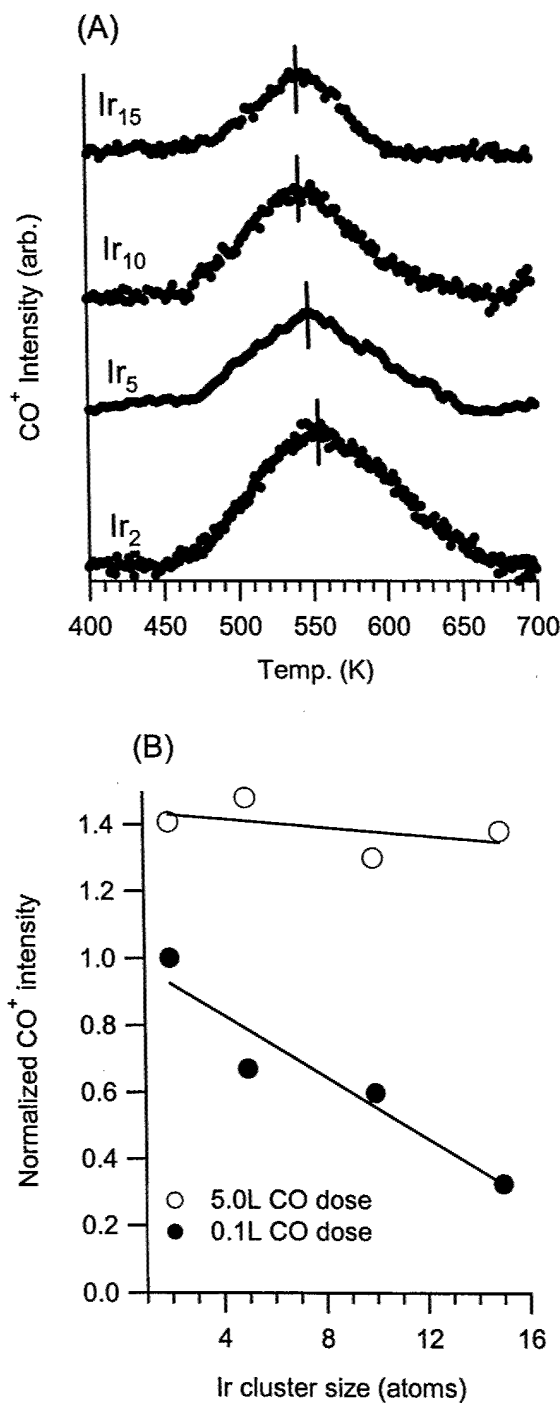


Fig. 7 Aizawa et.al.

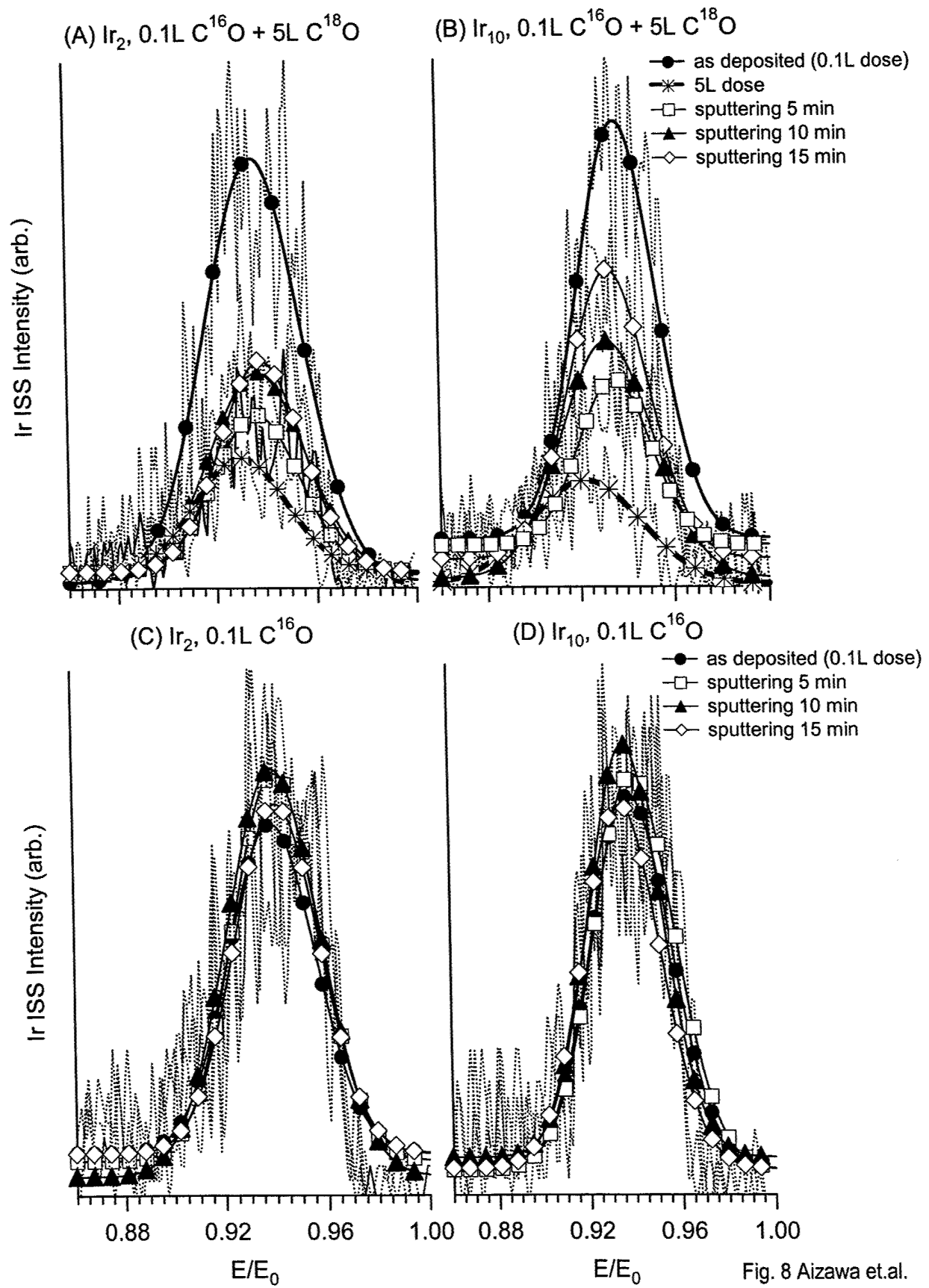


Fig. 8 Aizawa et.al.

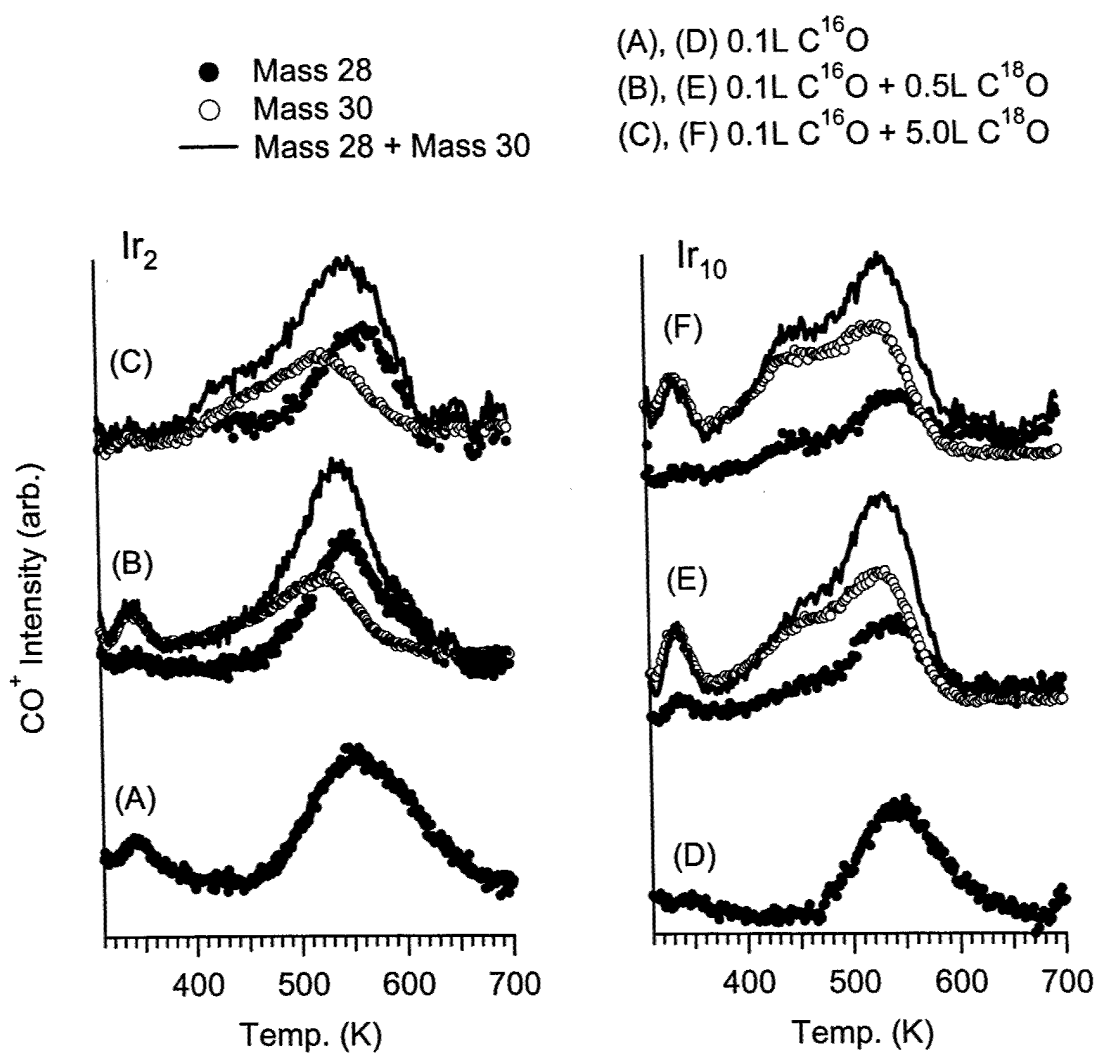


Fig. 9 Aizawa et al.

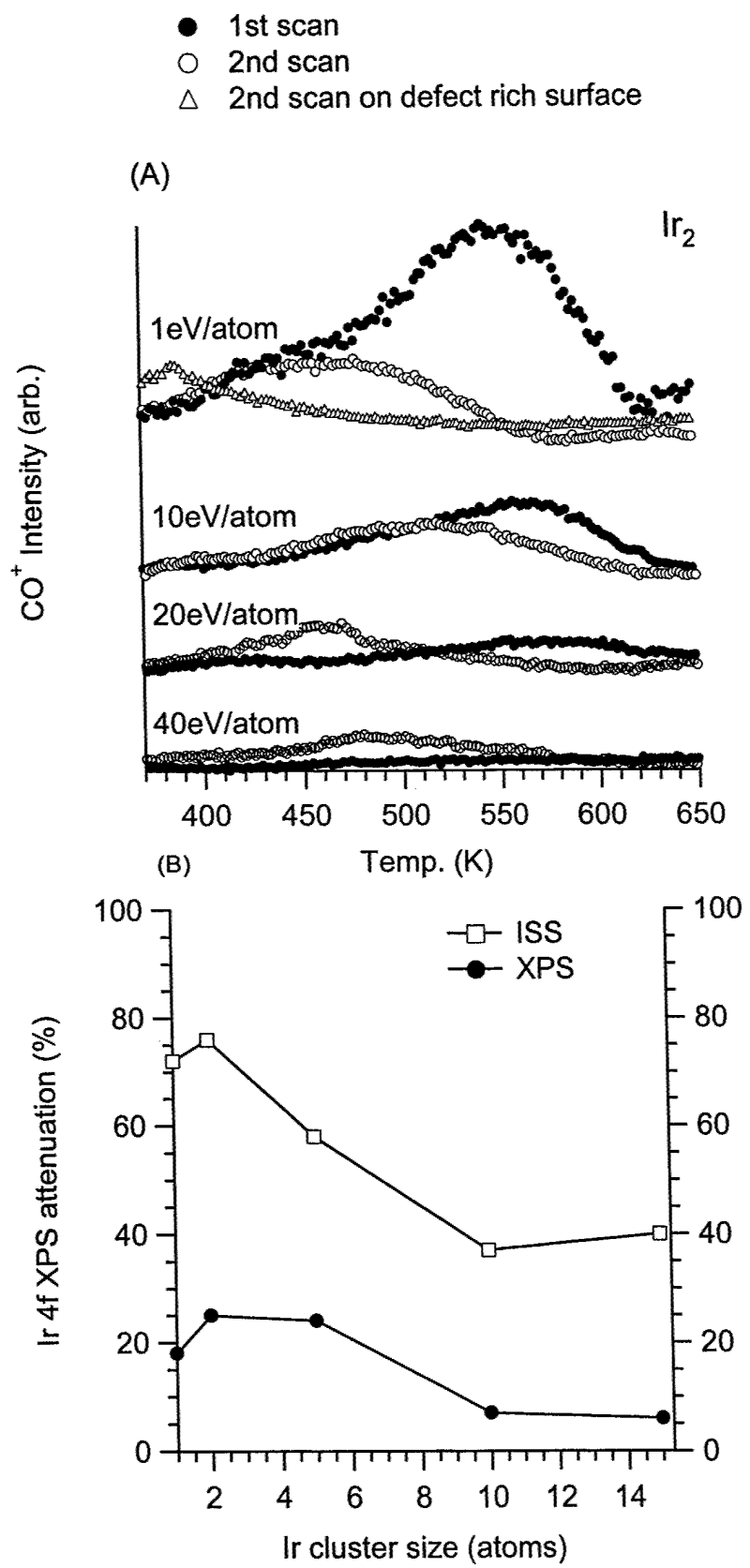


Fig. 10 Aizawa et.al.